THEORETICAL AND EXPERIMENTAL STUDIES ON THE PROPAGATION OF LONGITUDINAL ELASTIC STRAIN PULSES IN WIDE RECTANGULAR BARS

Thesis by

Orval Elmer Jones

In Partial Fulfillment of the Requirements

For the Degree of

Doctor of Philosophy

California Institute of Technology

Pasadena, California

1961

ACKNOWLEDGEMENTS

The author wishes to express his deep appreciation to Dr. A. T. Ellis who directed this research. His enthusiasm, encouragement, and guidance made this work possible.

Thanks are also due to Dr. J. Miklowitz for many helpful discussions during the course of the work.

Personal support from the following sources is gratefully acknowledged: Institute Scholarships and Graduate Teaching Assistantships, 1957-58 and 1958-59; National Science Foundation Fellowship, 1959-60; Hydrodynamics Laboratory, 1960-61. Financial support for the work was partially provided by a National Science Foundation research grant. Assistance from C. Eastvedt, G. Lundgren, M. Jessey, L. Gaard, and B. Wood helped bring the work to completion.

Finally, the author wishes to thank his wife, Pauline, for her continued encouragement and help.

ABSTRACT

The method of birefringent coatings is considered as an experimental means of studying wave propagation phenomena in metals. Experiments using the Ellis ultra-high-speed camera and a rectangular aluminum bar having a birefringent coating of PhotoStress indicate that transient fringe patterns resulting from impact can be successfully photographed using existing film and light sources at exposure times of 0.05 microseconds. Pronounced fringe curvatures, indicating the warping of plane sections, were observed in the pictures during the passage of the strain pulse.

The propagation of a longitudinal elastic strain pulse in a wide rectangular bar is considered on the basis of the approximate plane-stress equations of motion. Asymptotic expressions are obtained which, for large distances of travel, describe the propagation in a semi-infinite strip with stress free lateral edges, subject to the conditions that a uniform normal stress with a step-function time dependence is applied to the end and that the end undergoes no lateral extension. These expressions are shown to qualitatively predict the warping of plane sections observed in the high-speed pictures and in the dynamic photoelastic pictures obtained by other investigators.

Measurements using conventional measuring techniques are described in which wide rectangular aluminum bars of several thicknesses were subjected to a step-function pressure loading produced by a shock tube. Comparisons show that the gross features of the experimental records for the head of the pulse are qualitatively predicted by the plane-stress theory. Both theory and experiment show that short-wavelength second mode disturbances arrive very early. Experimentally it is observed that these disturbances are accompanied by thickness mode activity which cannot be accounted for by the two-dimensional plane-stress theory.

TABLE OF CONTENTS

TABLE OF CONTENTS (CONT'D)

I. INTRODUCTION

Although problems of vibration and elastic wave propagation in bars have been under investigation since the beginning of modern physical and mathematical analysis, much remains undone that is of active interest to present day engineers. There are at least two reasons for this state of affairs. (i) Even though the basic differential equations of motion have been known for over one hundred years, the mathematical difficulties are so great that exact solutions for normally encountered boundary conditions are usually not obtainable except in special cases. (ii) Recent advances in experimental techniques have pointed out problems which either were not previously conceived or which have made previous approximate solutions inadequate. In particular, present interest in the response of bars to extremely rapid rates of loading has made many of the early solutions inadequate since most of them were based on the assumption that the wavelength was of a different order of magnitude than the cross-sectional dimensions of the bar. The problem of wave propagation along a bar of rectangular cross-section falls under both of these categories.

The primary purpose of the studies reported in this thesis is to describe the propagation of a longitudinal elastic strain pulse in a wide rectangular bar, i.e., a bar having a small thickness-to-width ratio. Particular attention will be given to describing the warping of plane sections during the passage of the strain pulse. In later discussions, it will be pointed out that all of the present solutions for the propagation of longitudinal strain pulses in bars are based on the implicit or explicit assumption that plane sections remain plane.

The second objective of the thesis is to study the feasibility of

using a birefringent coating as an experimental means of studying wave propagation phenomena in metals. The results of this experimental investigation provided the stimulus for the rectangular bar studies.

Part II is concerned with the investigation of birefringent coatings as a possible means for experimentally studying transient strain distributions. A critical discussion of dynamic photoelasticity and the method of birefringent coatings is presented. Experiments are described in which ultra-high-speed motion pictures were obtained for the transient fringe patterns associated with strain pulse propagation in a rectangular aluminum bar. Fringe curvatures observed in the pictures, indicating that plane sections were warping noticeably, provided the motivation for detailed studies of longitudinal strain pulse propagation in rectangular bars.

In Part III, asymptotic expressions based on the plane-stress equations of motion are obtained which, for large distances of travel, describe the longitudinal elastic strain wave propagation in a semi-infinite strip with stress free lateral edges, subject to the conditions that a uniform normal stress with a step-function time dependence is applied to the end and that the end undergoes no lateral extension. These expressions are derived from the lowest order approximate equations of motion that might be capable of describing the observed warping of plane sections.

In Part IV, theoretical predictions of the plane-stress theory for the warping of plane sections are compared with the pictures obtained in Part II and the dynamic photoelastic pictures obtained by other investigators. An extensive experimental program using conventional measuring

techniques is described in which wide rectangular aluminum bars were subjected to a step-function pressure loading by a shock tube. This program was undertaken for the purpose of providing more critical tests of the plane-stress theory and gaining further insight into the physical problem. Extensive comparisons are made between the results of these experiments and the theoretical predictions.

Since the objectives of Part II and of Parts III and IV are of a different nature, it is convenient to present the conclusions and recommendations of this thesis in two sections. The first section is at the end of Part II and the second is at the end of Part IV.

II. INVESTIGATION OF BIREFRINGENT COATINGS AS AN EXPERIMENTAL MEANS OF STUDYING WAVE PROPAGATION PHENOMENA IN METALS

Introduction

The problem of determining the transient distribution of stress and strain in a metal specimen subjected to an impact type of loading is difficult to solve mathematically. Very few theoretical solutions have been obtained and generally those which are available deal only with very simple geometries and loadings. Also, these solutions are generally not applicable to all points in the specimen for all times, and they are often not in a readily usable mathematical form. The mathematical difficulties make an experimental approach to the problem highly desirable.

Much of the experimental work in this area has been conducted using resistance and piezoelectric strain gages. The disadvantage of this method is that observations are limited to a relatively few isolated points. Recently, considerable work has been done by numerous investigators in an attempt to apply photoelasticity to the study of wave propagation phenomena. The purpose of the present section, Part II, is to investigate birefringent coatings as an experimental means of studying wave propagation phenomena in metal specimens.

A critical survey of photoelasticity, both static and dynamic, and of the static method of birefringent coatings will serve to introduce needed concepts and emphasize the motivations for the present study.

Background

1. Birefringence and Static Photoelasticity

The photoelastic phenomenon is best introduced in connection with

its successful application to elastostatic problems. It provides a powerful experimental tool for quantitatively determining the elastostatic stresses in bodies having geometries and loading configurations which are not amenable to mathematical analysis. The technique is based on the fact that when most transparent solids are stressed they lose their optical isotropy and become birefringent, i.e. the value of the refractive index depends on the plane of polarization of the incident light. If a specimen in the form of a plate is stressed it is found that at every point of the specimen there are two mutually perpendicular directions of polarization parallel to the plate for which the refractive index has a maximum and minimum value respectively. For many birefringent materials these directions correspond to the directions of principal stress. Of these materials, those which are commonly used in static photoelasticity have a characteristically brittle behavior, exhibiting a more or less linear stress-strain relationship up to the point of failure, which usually takes place without appreciable permanent deformation. For most such materials it is found that up to the elastic limit the difference between the extreme values of the refractive index is proportional to the algebraic difference in the values of the principal stresses. The constant of proportionality is known as the stress-optical coefficient and is a physical constant of the material. A birefringent material exhibiting more or less all of these properties can be conveniently termed a "photoelastic material".

When a beam of plane polarized light passes through a stressed specimen made of photoelastic material it may be considered to be resolved into two components which are plane polarized in directions perpendicular to

each other and parallel to the directions of principal stress. The components travel through the specimen with different velocities so that a phase difference is developed between them which, in general, causes the emergent light to be elliptically polarized. If this light is viewed with an analyzer, e.g. a sheet of polaroid, the observed intensity depends on the phase difference introduced by the specimen and hence on the applied stress. If monochromatic light is used the specimen will appear to be traversed by light and dark fringes. Since the observed fringe pattern depends on the stress distribution in the specimen, it is possible to determine the difference in principal stresses throughout the specimen.

For a plate having a single boundary, the stress distribution does not depend on the elastic constants of the material. For a multiply-connected plate the stress distribution generally depends on the elastic constants; however, their effect on the maximum stress is usually very small, and in practice it can usually be neglected. These conclusions imply that an experimental stress distribution obtained with a photo-elastic material in most cases can be applied immediately to any other material, such as steel. This fact is the basis for the success of static photoelasticity. A very desirable feature of the photoelastic method is that it gives an overall visual picture of the shearing stress distribution throughout the specimen which facilitates the location of the regions of peak stresses. The difficulty in accurately separating the principal stresses at interior points of the specimen is a major disadvantage.

The photoelastic method has been widely used to experimentally determine the static stress distribution in engineering structures and

accounts of the theory and the application of the method to engineering problems can be found in books on the subject by Coker and Filon (1), Frocht (2,3), and Jessop and Harris (4).

2. Dynamic Photoelasticity

The success of photoelastic methods in dealing with elastostatic problems has naturally created considerable interest in their possible application to transient problems. It will be worthwhile to briefly describe the experimental work which has been done in this area and the difficulties which have been encountered.

Techniques: In order to photoelastically study wave propagation phenomena it is necessary to take high-speed photographs of the moving fringe field. Since stress waves propagate in the usual photoelastic plastics at velocities of roughly 60,000 inches per second, the exposure time for each photograph must not exceed 0.6 microsecond for a photographic resolution of at least 0.04 inch in the specimen. Consequently, early photoelastic pictures obtained by Frocht (5), Tuzi and Nisida (6), Findley (7), Murray (8), and Foeppl (9) which had relatively long exposure times, while showing time-dependent stress distributions, did not exhibit stress wave propagation.

In recent years advancements in the techniques of high speed photography have made it possible to obtain photoelastic records of stress wave propagation. Frocht, Flynn, Landsberg, and Betser (10-12) have greatly improved the technique of streak photography for photoelastic purposes. The method consists of placing a narrow slit close to the model, and the birefringence occurring in this section during the period of stress wave propagation is photographed on a strip in a revolving drum. This provides

a continuous method of recording which, with a very narrow slit, high drum velocity, and fast film emulsion speed, is capable of arresting birefringence variations of roughly one microsecond duration. The disadvantage of streak photography is that it records the birefringence along a single line of the specimen, but gives no information about the fringe pattern throughout the rest of the model. Frocht and his associates, using Castolite as the specimen material, examined transient stresses in the central sections of impacted solid disks and simply supported beams, and longitudinal waves in bars.

In the investigations of Schardin and Struth (13), Schardin (14), Christie (15,16), and Wells and Post (17) high-speed photographs have been taken of the whole specimen, or of an extended portion of it, by using a system proposed by Cranz and Schardin (18) some 30 years ago. The Cranz-Schardin system employs a set of separately fired spark sources and a corresponding number of image forming beams in juxtaposition to give a small number of pictures spaced arbitrarily in time. Christie (15) obtained excellent photoelastic photographs representing the propagation of stress waves in glass and perspex. In a thorough study, Wells and Post (17) photoelastically analyzed the stress distribution surrounding a moving crack in Columbia Resin CR-39.

If a given set of experimental conditions can be reproduced accurately a sequence of separate pictures, each produced by a single flash of light of very high intensity and very short duration (< 1 microsecond), can be obtained by using different delay times in successive tests. This technique is equivalent to high-speed cinematography and has been used by Senior and Wells (19), and more recently by Goldsmith and Norris (20).

Other investigators have utilized recently developed ultra-high-speed framing cameras for taking large-field pictures of wave propagation phenomena. Sutton (21) used the camera developed by Ellis (22) for examining stress waves caused by cavitation. Pictures were also obtained of stress waves propagating in an impacted bar made of CR-39. In the Ellis camera, light from a stationary source is reflected by a beveled rotating mirror, driven by a high-speed air turbine, onto a stationary circular film track, with a Kerr cell acting as a shutter. Framing rates of 10^6 pictures per second and effective exposure times of less than 0.1 microsecond have been attained using this system. Feder, Gibbons, Gilbert and Offenbacher (23) employed the Beckman-Whitley framing camera to record stress wave propagation in plates and bars of CR-39 at effective exposure times of approximately 0.6 microsecond. The chief disadvantage of this camera is that the exposure time is a function of the framing rate.

An alternative approach has been to use low-modulus photoelastic materials ($E < 800$ psi) in place of the more rigid materials. In low-modulus materials the velocity of propagation of the stress wave is decreased (by an order of magnitude) over the velocity of propagation in conventional photoelastic materials, and it is possible to record clearly the dynamic fringe patterns using a Fastax camera operating at about 13,000 frames per second. This approach was first introduced by Perkins (24) who obtained photographs of wave propagation in birefringent rubber and gelatin. Durelli, Riley, and Dally (25-27) have conducted extensive continuing dynamic photoelastic studies of low-modulus specimens. In particular Hysol 8705, a castable urethane rubber compound, gave striking dynamic photoelastic fringe patterns (e.g. (26)). Since this

low-modulus material exhibits relatively large displacements under small loads, Durelli and his associates found it feasible to embed a rubber-thread grid network in the specimen and then measure the displacements. Displacement measurements were used in conjunction with fringe photographs to separate the principal stresses and obtain quantitative results for transient stresses in a thin rectangular bar subjected to impact (27).

Fundamental Difficulties: In general the investigations described above have yielded little in the way of quantitative results. This is due to technical limitations and fundamental difficulties which will be briefly described.

The photoelastic technique of stress analysis is subject to several limitations when applied to static problems, and in stress wave studies these limitations are much more serious. Thus, only transparent materials can be used, and in general only two-dimensional analysis is possible. The fringe patterns give only the difference in magnitude between the principal stresses and not their absolute magnitudes. Also, unless the experiments can be accurately repeated a number of times, the principal stress directions cannot be determined.

There are, however, more fundamental difficulties which must be considered before dynamic photoelasticity can be used to model stress wave propagation in metal parts. Many of the viscoelastic polymers used for their high photoelastic sensitivity have elastic properties which exhibit marked dependence on the rate of loading. In particular the elastic modulus of these materials is found to increase with an increase in frequency of an applied sinusoidal stress. From the wave propagation view point this means that the medium itself is dispersive, i.e., sinusoidal waves of high-

frequency are propagated with a greater phase velocity than low-frequency waves, and, consequently, an arbitrary disturbance propagating through the medium continually changes its shape even in the absence of boundaries. The attenuation of high-frequency waves is also found to be greater than that of lower frequency waves, so that there is a differential absorption as well as a dispersion of the Fourier components of a pulse. A possible representation of these effects is in terms of a complex elastic modulus which is frequency dependent.

In static photoelasticity, the viscoelastic behavior of these high polymers gives rise to creep effects causing the stress-optical coefficient to be time-dependent. For the useful photoelastic polymers creep effects are negligible within the limits of the applied stresses. Also, in static applications the material must follow Hooke's law so that the model conforms to elastic theory. Under these conditions, the use of stress-optical coefficients rather than strain-optical coefficients is purely a matter of convenience. Now, under dynamic conditions, for which the elastic properties depend markedly on the loading rate, it is not known a priori whether the birefringence of these materials is proportional to the stress, is proportional to the strain, or is a function of both.

Recently, investigators have been giving increased attention to these problems. For a low-modulus cold-setting Araldite epoxy resin, Durelli and Riley (25) found that as the dynamic modulus of elasticity increased the stress-optical coefficient increased in about the same proportion. This gave a strain-optical coefficient essentially independent of the loading rate. Similar conclusions were reached by Sutton (21) and Clark (28) in tests conducted on Columbia Resin CR-39. Sutton (21) also obtained data indicating that the high frequency components of a

pulse would be very severely attenuated by CR-39. In tests on Hysol 8705, Durelli, Riley, and Dally (26,27) found that the stress-optical coefficient was independent of the loading rate except for very low strain rates, and both the modulus of elasticity and the strain-optical coefficient were dependent on the rate of loading. Frocht and his associates (29) found for Castolite that the stress-optical coefficient and the modulus of elasticity were independent of the loading rate. Frocht's conclusions are rather surprising in relation to the observations made with other photoelastic materials.

The diversity of the methods employed by the respective investigators in arriving at these results should be noted. In general, further tests of a more definitive nature are required before drawing any concrete conclusions.

It should be clear that dynamic photoelasticity, while providing valuable qualitative information on elastic wave propagation, may not be a particularly useful experimental tool for quantitatively studying transient phenomena in elastic materials. In static photoelasticity, the experimental stress distribution obtained with a photoelastic material in most cases can be immediately applied to useful structural materials, such as steel and aluminum, by virtue of the independence of the stress distribution on the elastic constants of the material. In the case of dynamic photoelasticity, the transient stress distribution is very markedly influenced by the elastic constants of the material. For high rates of loading it is not at all clear just how the experimental stress distributions obtained for common photoelastic materials having strongly frequency-dependent complex elastic moduli and Poisson's ratios of nearly one-half can be quantitatively applied to structural metals having real constant

moduli and Poisson's ratios of approximately one-third. Although this difficult problem has received very little attention, its solution is essential to the development of dynamic photoelasticity as a practical experimental tool for studying wave propagation phenomena in the usual structural materials. The desirability of obtaining full-field motion pictures of wave propagation phenomena is undeniably strong; but, it is apparent from this brief survey that the usefulness of dynamic photoelasticity for quantitatively studying transient stress distributions in metals is subject to considerable doubt.

3. Method of Birefringent Coatings for Static Strain Measurement

The technique of using a birefringent coating for determining surface strain distribution was originally conceived in 1930 by Mesnager (30), who suggested cementing a birefringent layer to a polished metal part and using a reflection polariscope to determine the surface strains of the loaded part. The underlying concepts are much the same as those of conventional photoelasticity although the need for a model is circumvented by having the actual structure or part load the birefringent material. The cemented face of the birefringent coating is forced to follow the strain of the metal surface giving rise to photoelastic fringe patterns. From these patterns the difference in magnitude of the principal strains and the principal strain directions can be determined. Since elastic and plastic strains are usually very small in metals, the birefringent coating must have a high strain-optical sensitivity.

The method became practicable only with the introduction of epoxy resins which strongly adhere to metals and which have high strain-optical sensitivities. D'Agostino, Drucker, Liu, and Mylonas (31,32) conducted

extensive investigations of the photoelastic properties of epoxy resins and of the behavior of birefringent coatings. It was found that the strain-optical sensitivity of some epoxy resins is sufficiently high (approximately $1.5 \cdot 10^{-4}$ strain difference per fringe per inch thickness) that even with a relatively thin coating an appreciable fringe order is obtained for elastic or plastic strains in metals. Similar investigations were being made almost simultaneously in France by Zandman (33) and shortly thereafter his birefringent materials along with specially developed pieces of optical equipment for making measurements were offered commercially in this country by Tatnall Measuring Systems Company under the name of PhotoStress (34).

An important advantage of the birefringent coating technique over other methods of measuring strain on actual structures and parts is that the strain distribution is obtained over the entire coated area in a single picture. However, in static applications, the observed birefringence is directly proportional to the surface strain at a point only as long as the strain is uniform over the surface or changes little over distances comparable to the coating thickness. In such cases it is relatively easy to determine the strain. However, in the presence of strain gradients at the metal surface the deformation of the coating will vary through its thickness and the observed birefringence will depend on the magnitude of the strain and also on the intensity of its gradient. In addition, the photoelastic pattern will be affected by any curvature of the metal occuring under load. Unfortunately, the manufacturers of PhotoStress have given these facts very little publicity.

Since the elastic modulus of a birefringent coating at room temperature is generally about one-twentieth the modulus of aluminum, it can be

assumed that the birefringent coating has a negligible effect on the surface strain distribution in the actual part provided the thickness of the part is several times the coating thickness. Also, when the metal is under strain the birefringent coating, in general, will undergo elastic deformation even for plastic strains in the metal of the order of several percent. Under these conditions, the problem of analyzing the static strain distribution in the coating is a boundary value problem in elasticity. Duffy (35) has considered the effects of coating thickness and surface curvature for an infinite coating of uniform thickness in which the variations in an arbitrary displacement at the metal surface are limited to one dimension and the stresses vanish on the other surface. His results for the case of no surface curvature indicate that very serious errors may result if it is assumed that at each point the strain throughout the thickness of the layer is the same as the interface strain. With a sinusoidally varying strain and a coating as thin as one-tenth of the wavelength of the strain variation the error may be as large as thirty-five percent. With sharper strain gradients and at discontinuities the errors will be much greater. The major difficulty is that the error is not in general constant over the coated area: its value depends on the variations in the wavelength of the strain gradient. In a later study Lee, Mylonas, and Duffy (36) analyzed the thickness effects in birefringent coatings with radial symmetry and arrived at the same general conclusions.

If the coating is sufficiently thin the error approaches zero and the surface strains can be simply related to the fringe pattern. However, this approach has the serious disadvantage that an extremely thin coating of any currently available birefringent material gives a very small

birefringence which implies large experimental errors. For example, a one-eighth inch thick coating of the most sensitive epoxy resin on aluminum shows only about two fringes in green light at one-half the yield point strain. Materials having much greater strain-optical sensitivities are needed; fortunately, physical chemists working on this problem feel that materials can be developed which have an order of magnitude more sensitivity than existing resins (37).

Preliminary Considerations

Although dynamic photoelasticity raises more questions than it answers when a quantitative correlation of transient stresses is attempted between an elastic part and its photoelastic model, the continuing interest in it reflects the attraction of an experimental technique which affords full-field visualization of wave propagation phenomena. Under certain conditions birefringent coatings, which also give full-field visualization, should be useful for experimentally studying elastic wave propagation without being subject to the fundamental difficulties of dynamic photoelasticity.

The propagation of waves in a metal part having a birefringent coating is actually a layered media problem in which one layer is elastic and the other is viscoelastic. For an arbitrary coating thickness, the birefringent response of the coating, being influenced by both layers, can be expected to be exceedingly complex. If, however, the coating thickness is "sufficiently thin" it is reasonable to expect that the birefringent response will be almost solely dependent on the surface strain of the metal. This statement requires elaboration.

It has already been noted that the modulus of a birefringent coating is approximately one-twentieth the modulus of aluminum. Consequently, in the case of a "sufficiently thin" coating applied to a relatively thick metal part, the constraint of the metal surface due to the coating should be negligible and the metal surface should behave very much as a free boundary. The poor impedance match between the coating and the metal surface should minimize the rate at which an elastic wave propagating in the metal loses energy to the coating. A "sufficiently thin" coating might be expected to satisfy the following conditions: (i) The wavelengths of the interface strain variations should be much greater than the coating thickness. (ii) The periods of the interface strain variations should be much greater than the time required for a shear wave to traverse the coating thickness. Under these conditions only very small high frequency disturbances should be generated in the coating; however, the viscoelastic coating will presumably attenuate such disturbances very severely. By using a sufficiently thin coating, then, the difficulties arising from a viscoelastic overlay on a metal part can possibly be circumvented with the coating serving as a continuum of homogeneous strain gages.

By this admittedly speculative and perhaps overly optimistic reasoning it seems possible that birefringent coatings might successfully be used for experimentally studying elastic wave propagation in metals. If so, then the technique could immediately be used to study plastic wave propagation in metals--an extremely attractive possibility.

The problem of obtaining an adequate fringe order with a sufficiently thin coating is immediately anticipated from the preceding discussion of static strain measurement. However, other technical difficulties arise in

connection with photographing the transient fringe patterns. Since strain waves propagate in most metals at velocities of approximately 200,000 inches per second, the exposure time for each photograph must not exceed 0.1 microsecond for a photographic resolution of approximately 0.02 inch in the specimen. The requirements for a high-speed camera are almost an order of magnitude more stringent than they were for dynamic photoelasticity. In particular, obtaining enough light to expose a picture becomes a major problem. Because of the shorter exposure times and the necessity of reflecting the light from a relatively unpolished metal surface, the intensity of the light must be roughly an order of magnitude greater than for dynamic photoelasticity. Also as the exposure times decrease the question of reciprocity failure becomes increasingly important. To evaluate the usefulness of birefringent coatings for transient strain measurements, then, experimental investigations are required to answer two general questions: (i) Is it technically possible to photograph the moving fringe patterns. (ii) Do the fringe patterns represent the surface strains of the metal. The second question is, of course, academic if the fringe patterns cannot be recorded.

An experimental program was undertaken during 1957-58 to answer the first question and, hopefully, to gain some insight into the second question. Although it was realized that the coatings should be thin, it was necessary to use relatively thick coatings in order to obtain photographically significant fringe orders. Preliminary experiments requiring a minimum of instrumentation were conducted to determine whether there was sufficient assurance of success to warrant attempting to take high-speed pictures.

Initial Experiments

1. Experimental Equipment and Procedure

Birefringent coatings: Professor C. Mylonas of Brown University very kindly provided two coated aluminum specimens which were used in the first few experiments. Shortly after the program's inception several ineffectual attempts were made to develop a technique for casting strain-free coatings of epoxy resins, in particular Epocast 205 (formerly Araldite CN501) which has a high strain sensitivity (32), onto metal surfaces. No further attempts were made when it was discovered that PhotoStress was commercially available.

There are two general types of PhotoStress material: one type which is suitable for strains up to 2.5 percent and the other for strains up to 30-50 percent. Both types are obtainable in either flat sheet or liquid form, the liquid form generally being used on curved surfaces. The sheet, after being cut to proper size, is bonded to the surface in question using a transparent epoxy cement. The sensitivity of a Photo-Stress resin is given in terms of a strain-optical constant K. The relationship between K and the conventional strain-optical coefficient C_e for a given wavelength of light λ is $C_e = \lambda/K$. For $\lambda = 5461$ Å, C_e for $K = 0.1$ resin is $2.15 \cdot 10^{-4}$ strain difference per fringe per inch thickness as compared to $3.48 \cdot 10^{-4}$ for less sensitive CR-39 and $1.7 \cdot 10^{-4}$ for Epocast 205.

Figure 1 shows a 2024 T4 aluminum bar 0.250 inches thick, 0.978 inches wide, and 10.75 inches long to which a 0.120 inch thick sheet of Type S ($K = 0.1$ and $e_{max} = 2.5$ percent) PhotoStress has been bonded. This particular bar was used exclusively in all but the first few experiments.

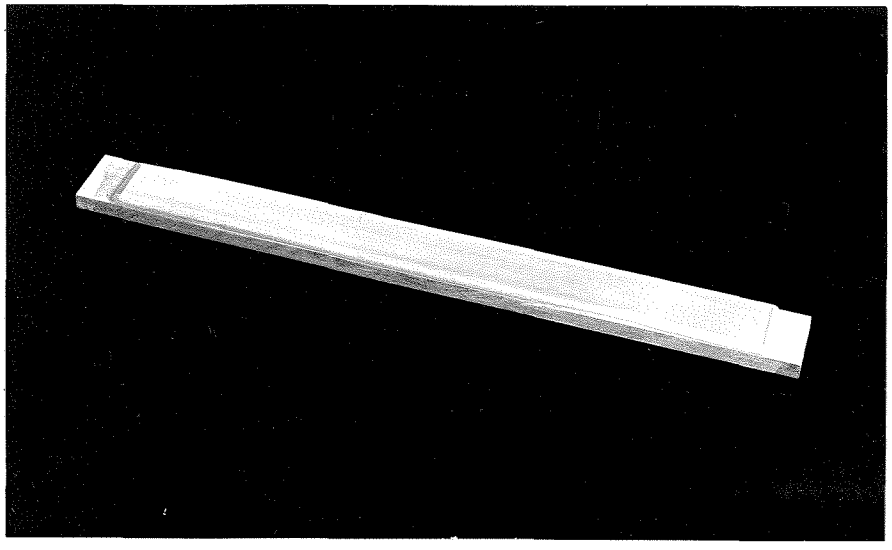

Figure 1. Aluminum bar with birefringent coating.

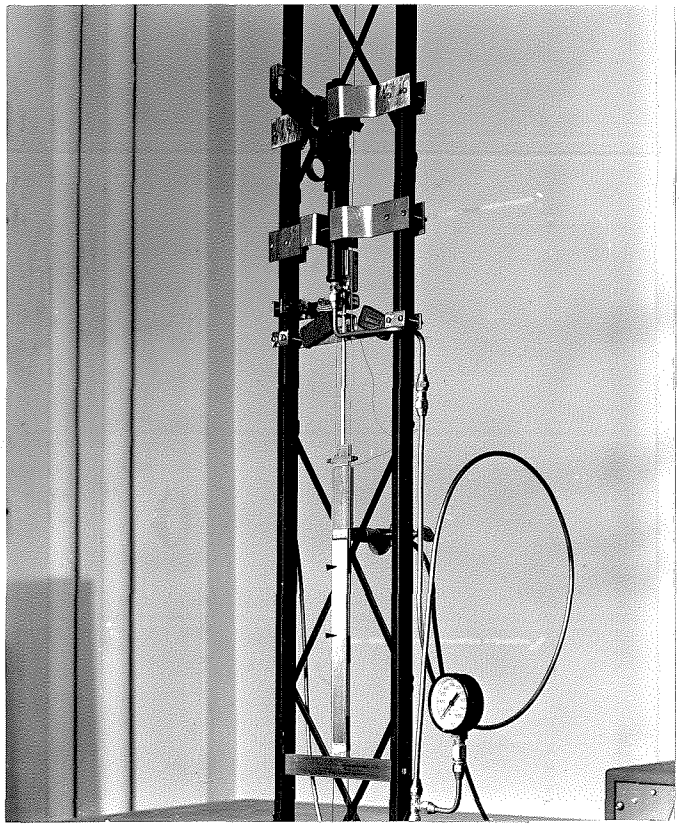

Figure 2. Close-up of impact loading apparatus.

Loading devices: In the first tests the bar was impacted in the loading frame built by Sutton (21). An aluminum tup falling through a distance of approximately 7 feet provided an impact capable of giving slightly more than one fringe if coating thickness effects were ignored.

For higher fringe orders, higher impact velocities were required to give larger strain differences. The essential arrangement used for obtaining higher velocities is shown in figure 2. A 0.062 pound aluminum hammer guided by two vertical wires is fired from a .22 caliber Crosman air pistol at impact velocities of approximately 35-40 feet per second for input chamber nitrogen pressures of approximately 500 psi. Two circumferential grooves filled with magnetic dispersion and spaced 0.25 inches apart on the cylindrical part of the hammer generate two pulses as they pass by a Brush tape recorder pickup head. The average velocity of the hammer at impact can be determined by measuring the time between these pulses with a Berkeley 7360 counter. Using the air pistol should give about two fringes if coating thickness effects are again neglected.

Photographic setup: Figure 3 is a schematic representation of the picture-taking equipment. A crystal pickup placed in contact with the bar near the point of impact generates a signal as the wave passes it. This signal, after amplification by a Tektronix 121 wide-band pre-amplifier, triggers the delay circuit of a Tektronix 513D oscilloscope which, after a prescribed time delay, puts out a sharp 90 volt pulse. This pulse "closes" a thyratron switch allowing a 0.04 microfarad condenser charged to 6800 volts to discharge into an Edgerton FX-2 xenon flash tube giving a flash of light approximately one microsecond in duration. The light passes through a No. 77A Wratten filter and then through a reflection polariscope made of a sheet of HN32 Polaroid, a sheet of

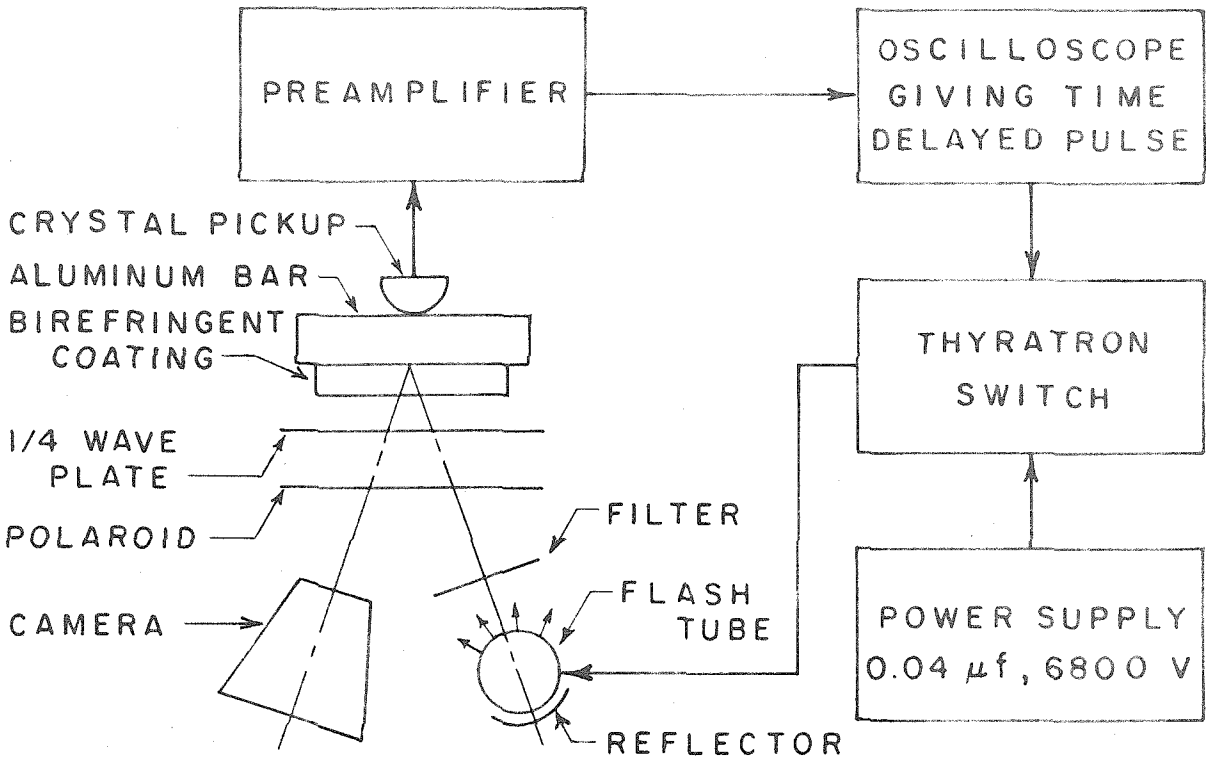

Figure 3. Schematic diagram of single-shot picture-taking apparatus.

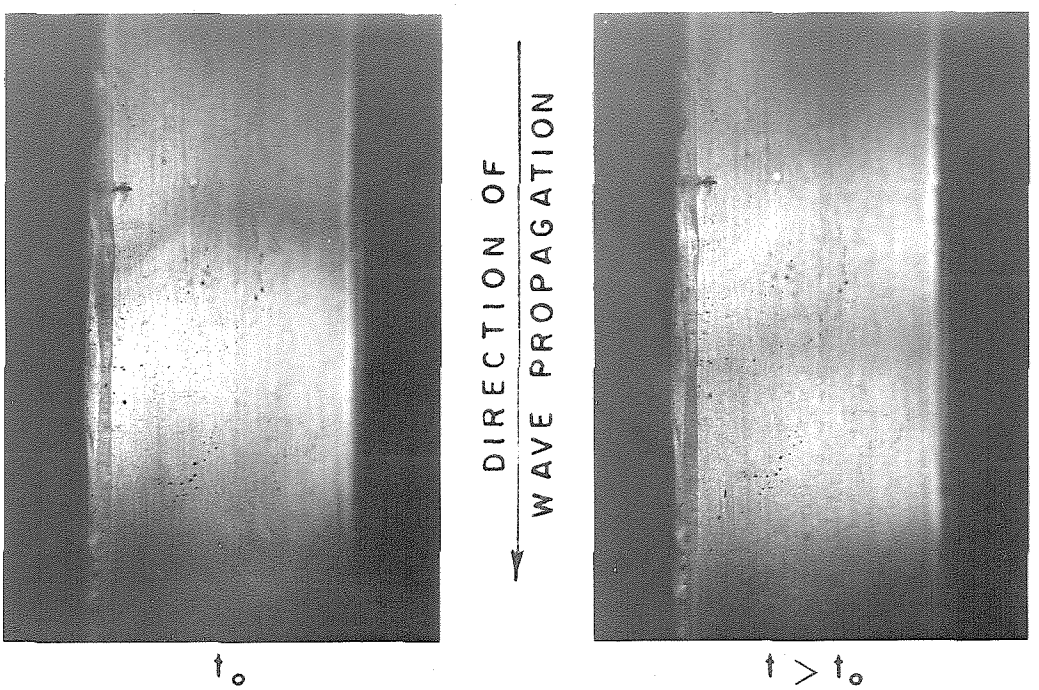

Figure 4. Single-shot photographs of transient fringe patterns resulting from impacting an aluminum bar having a birefringent coating.

quarter-wave plate, and the coated aluminum bar. This polariscope, arranged as shown in figure 3, behaves as a parallel circular polariscope and gives a dark field. The isochromatic fringe pattern is recorded on 4 x 5-inch Kodak-Royal-X Pan film using a 5 x 7-inch view camera fitted with a 7 inch f2.5 Kodak Aero-Ektar lens.

To take a photograph the oscilloscope time delay was set so that the wave front would be in the field of view when the flash tube fired. After darkening the room and uncovering the film, the loading device was actuated, setting into action the train of events described above. By assuming that the impact was fairly reproducible, a fringe time history was obtained by successively increasing the time delay and repeating the procedure.

2. Results

The gravity drop method of loading was tried with one of the specimens, a bar with a quarter inch thick coating, provided by Mylonas. After several unsuccessful tests it became apparent that the coating was not continuously bonded to the bar.

The next tests were made using the air pistol loading device and the coated aluminum bar described above. Figure 4 shows two fringe photographs taken at f4 which are assumed to be spaced 5 microseconds apart in time. The hammer impact velocity was approximately 34 feet per second in each case. Although the fringes are smeared out due to the relatively long exposure time of a microsecond, at least one fringe order is observable. These photographs also suggest that the wave is travelling roughly one inch in 10 microseconds; however, it is known from other sources (e.g. (38)) that a wave in aluminum should propagate about two inches in 10 microseconds.

This discrepancy was not taken seriously since it had been very difficult to obtain reliable triggering with the crystal pickup.

Based on these photographs, it was the opinion of Professor Ellis that high-speed motion pictures could be successfully taken using his camera. The shorter exposure time would be offset by a larger aperture and a flash tube having a higher intensity output. No further single-shot photographs were taken and the experimental effort was directed toward obtaining high-speed motion pictures of the fringe patterns.

Ultra-High-Speed Motion Pictures of Transient Fringe Patterns

1. Experimental Equipment and Procedure

In order to take motion pictures of the transient fringe patterns resulting from strain waves propagating in a coated metal specimen, the camera must be capable of framing rates of at least 10^5 pictures per second and effective exposure times of approximately 0.05 microsecond. The Ellis Kerr cell camera developed by Professor Ellis is capable of satisfying and even exceeding these very stringent requirements. In fact, the availability of this camera made this study technically feasible.

The particular camera which was used in the present investigation is shown in figure 5 and in a schematic sketch in figure 6. A brief discussion of the workings of the Ellis camera will be given here; more complete details are given in a publication by Ellis (22).

An electro-optical Kerr cell shutter is the basis of the Ellis camera. The Kerr cell consists of a glass barrel filled with nitro-benzene in which there are two flat electrodes parallel to the length of the barrel spaced 0.375 inches apart. Crossed polaroids cover the optically flat ends of the cell so that normally almost no light is

transmitted. When a voltage difference of 16,000 volts exists across the electrodes, the electro-optical Kerr effect operates to rotate the plane of polarization of the light polarized by the front polaroid so that it will pass through the rear polaroid. In the Ellis camera 16 kilovolt pulses of variable frequency and width are applied to the Kerr cell to operate it as a high speed shutter. Since the Kerr cell pulse voltage increases with the interelectrode distance, two lenses are used so that an image is formed between the electrodes which allows a small spacing to be used.

After passing through the Kerr cell shutter, a rotating mirror driven by an air turbine distributes the series of images onto a stationary 7 1/2 foot length of 35mm film lying on the inner periphery of a stationary drum. So there will be no double exposures, the Kerr cell is pulsed only during one revolution of the mirror. To avoid frame overlapping, the framing rate must be considered in relation to negative size and mirror speed.

The light source is a General Electric FT524 flashtube (xenon-filled quartz helix) into which the energy stored at 7000 volts in a 42 section lumped parameter transmission line is discharged. Each section consists of a 0.5 microfarad condenser and an 8 microhenry inductance: the impedance of the flashtube being taken as 4 ohms. With this arrangement the light intensity stays approximately constant over a period of 130 microseconds. About 50 microseconds are required to reach full intensity after triggering.

The arrangement of the polariscope, coated bar and camera is shown in figure 5 and in the schematic diagram of figure 6. The polariscope behaves as a mixed circular polariscope with parallel polarizer and analyzer and gives a light field. The bar is impacted with the air pistol loading

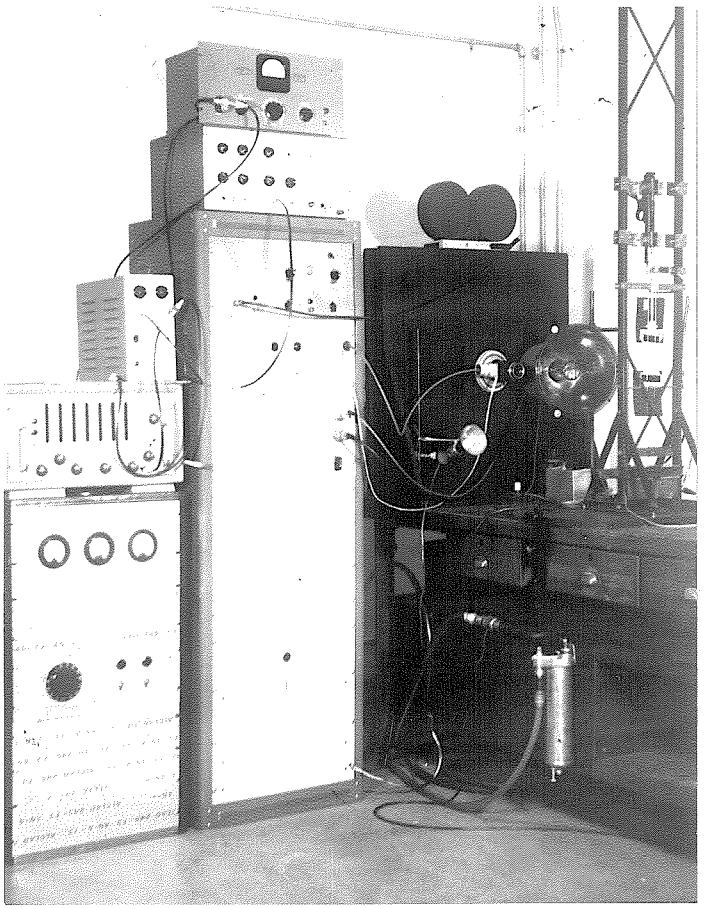

Figure 5. Ultra-high-speed motion picture apparatus.

(Left, power supply; left center, tachometer, delay timer and pulser; right center, camera and flashtube; right, bar and loading apparatus.)

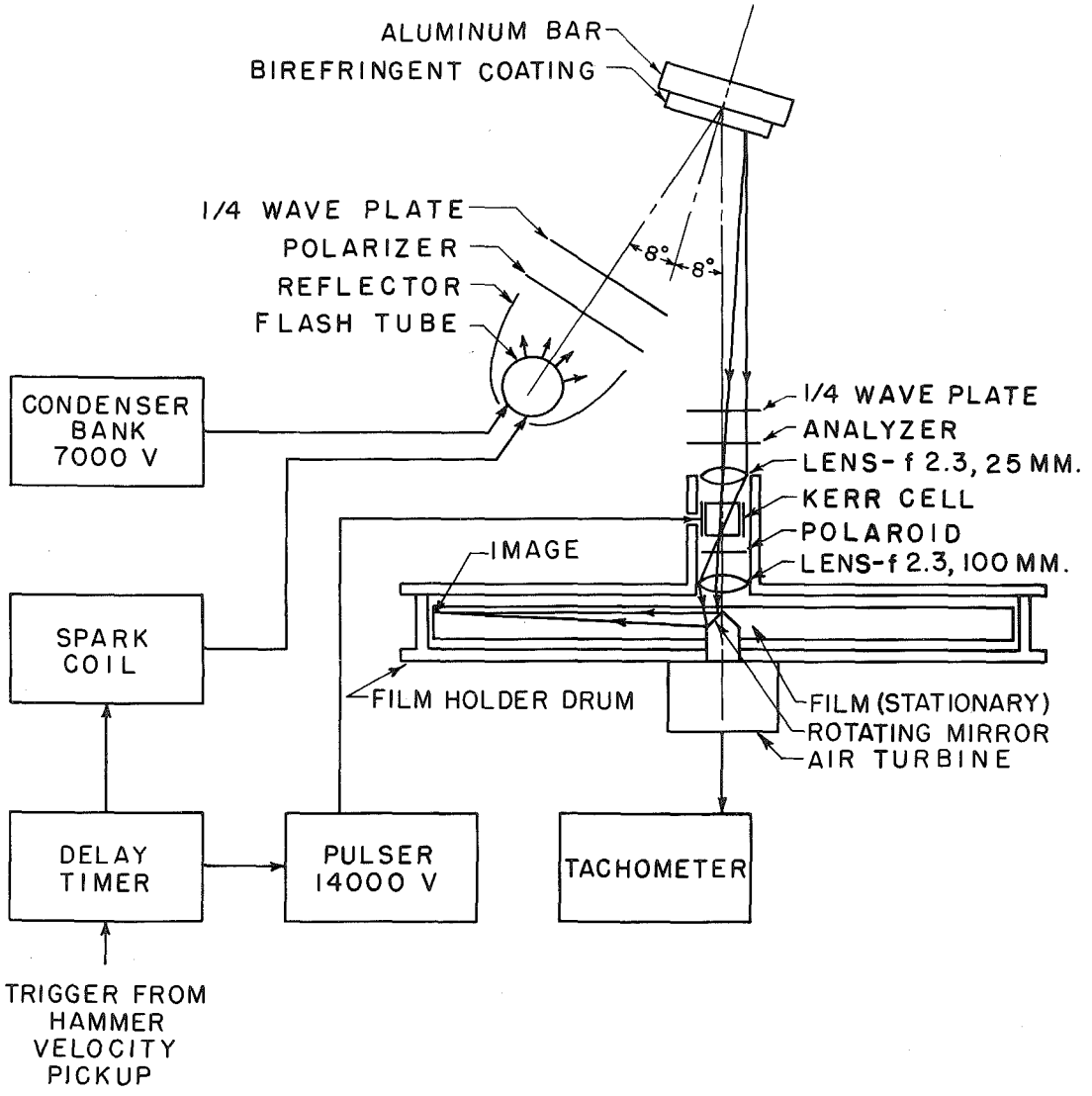

Figure 6. Schematic diagram of ultra-high-speed motion picture setup for photographing transient fringe patterns.

device used in the initial experiments. A pulse from the hammer velocity-pickup triggers the delay timer which in turn triggers the flashtube and the Kerr cell shutter after appropriate time delays. The time delays are chosen so that the shutter will be operating and the light will be of constant intensity when the wave front passes through the field of view of the camera.

In the first high-speed picture-taking attempts, Kodak Spectrum Analysis film, Type I-D(2), was used on the basis of tests (39) which indicated a very high sensitivity for very short exposure times. This film, available only on special order, could not be exposed because of an apparently defective emulsion. As an alternative, du Pont Superior 4 928 B film developed 15 minutes in D76 developer gave excellent results.

2. Results

Ultra-high-speed motion pictures of transient fringe patterns for two separate loadings of the bar are shown in figures 7 and 8. The time between consecutive frames is 10 and 5 microseconds, respectively. For both sequences the exposure time is approximately 0.05 microseconds. The impact velocity is approximately 35 feet per second in each case. A black pointer which was used for alignment purposes is visible along one side of each frame. The stationary dark line across each frame is the shadow cast by a spring clip holding the lamp in the reflector. The bar was masked off to give a field of view starting three-quarters of an inch from the impacted end and extending three inches along the bar. The black pointer lies between the dark line and the impact end of the frame. In figure 8 the indistinct strips along the sides of each frame are due to the beveled edges of the birefringent coating.

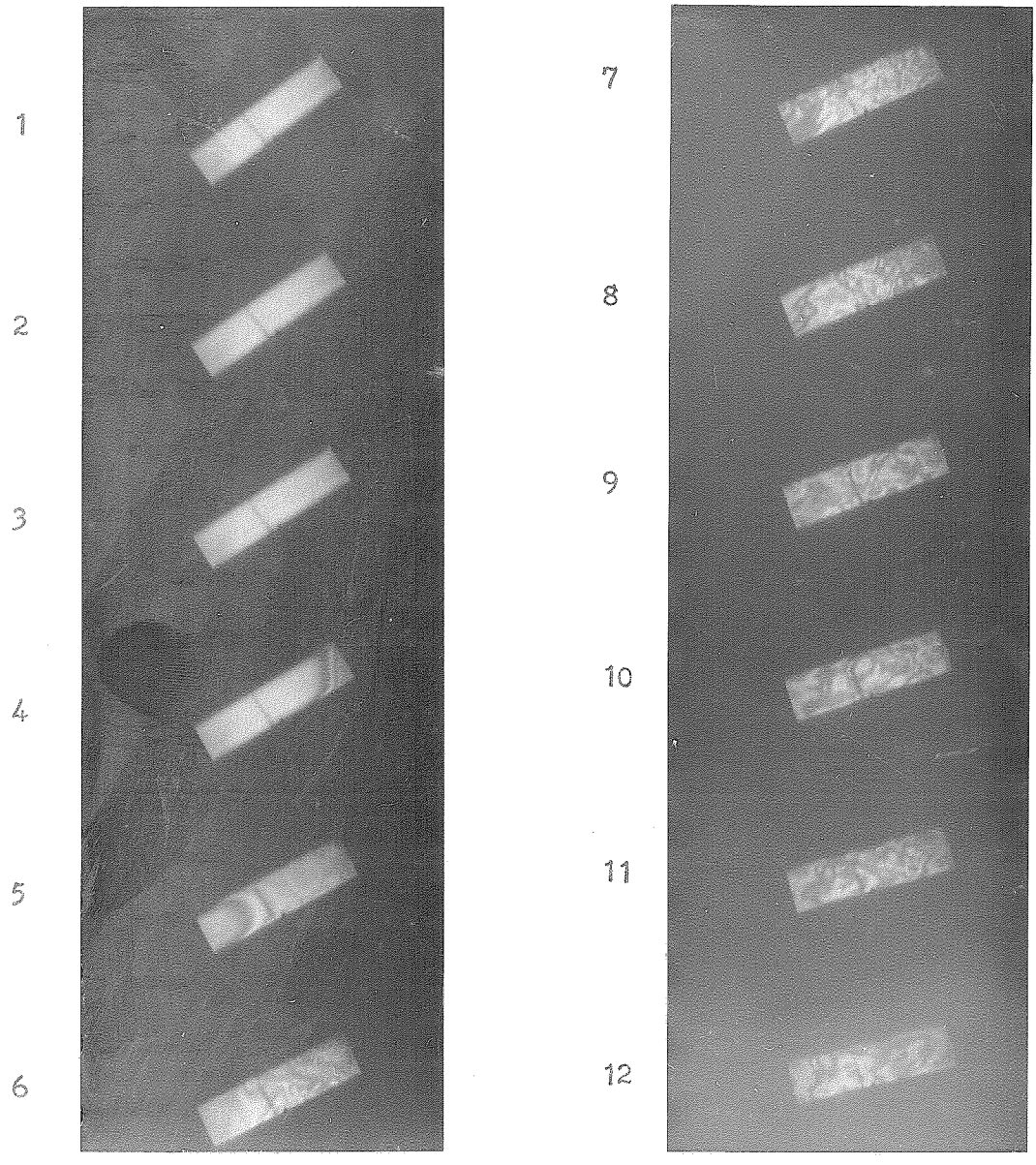

Figure 7. Ultra-high-speed motion pictures of transient fringe patterns resulting from impacting an aluminum bar having a birefringent coating. Time between frames, 10 microseconds; exposure time, 0.05 microseconds.

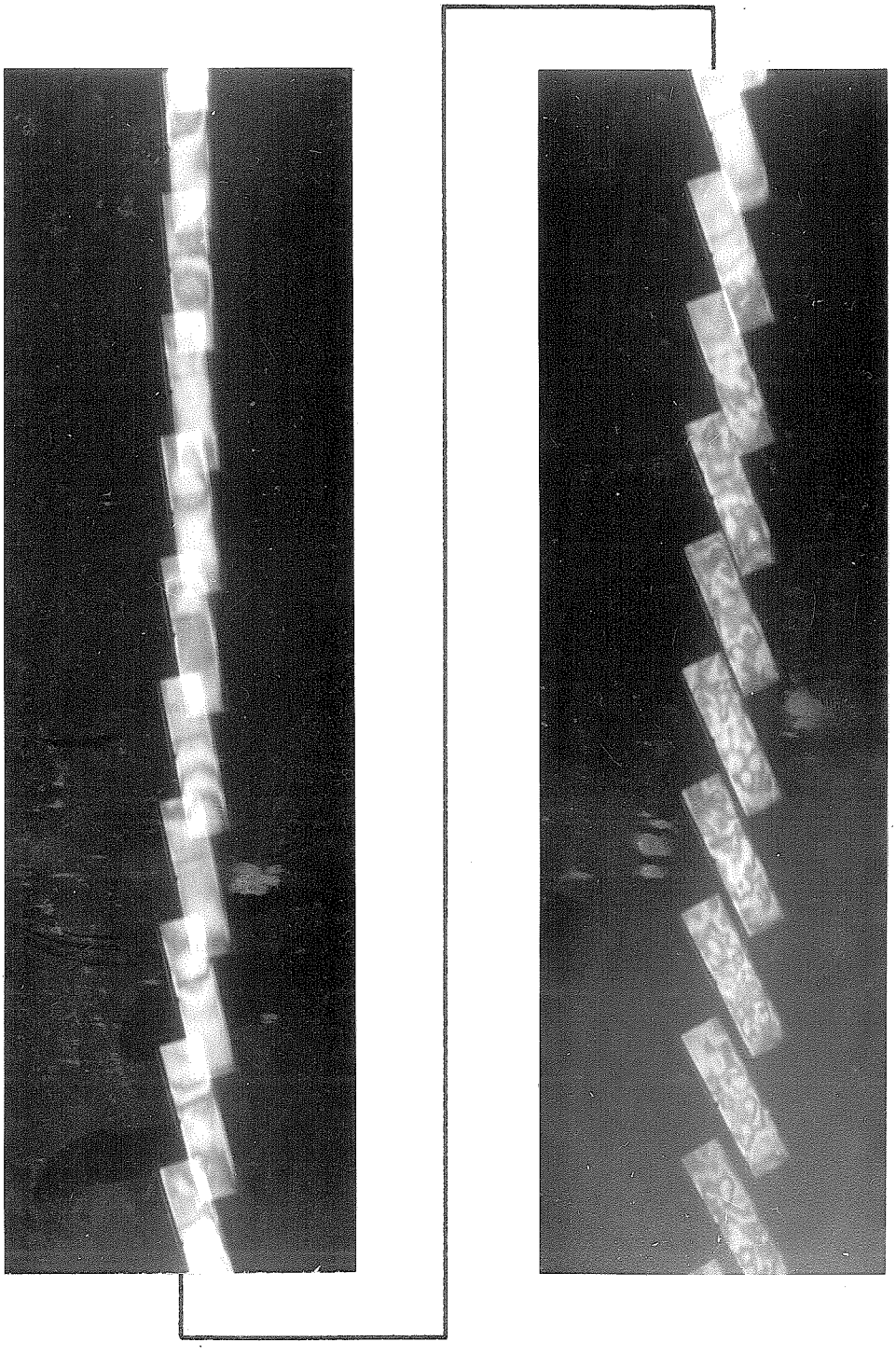

Figure 8. Ultra-high-speed motion pictures of transient fringe patterns resulting from impacting an aluminum bar having a birefringent coating. Time between frames, 5 microseconds; exposure time, 0.05 microseconds.

These pictures demonstrate that transient fringe patterns can be successfully photographed with existing film, light sources, and high-speed Kerr cell shutters. This was the major objective of the investigation. Examination of the pictures reveals several interesting features.

Considering figure 7, the uniformly bright field of frames 1, 2, and 3 indicates that the wave has not yet arrived. Frames 4 and 5 show the wavefront advancing across the field of view; the leading fringe travels slightly more than two inches, measured along the frame center-lines, during the ten microseconds between frames which corresponds to a velocity of approximately 200,000 inches per second. This is in excellent agreement with the long-wave velocity for aluminum of 202,800 inches per second given by Mason (38). Also, the distance between consecutive fringes increases between these two frames indicating some dispersion of the wave front. A fringe order of at least one and one-half is visible in frame 4 which is reasonable. The fringe pattern at the top of frame 4 indicates that the hammer hit on one corner. In frame 5 the shape of the fringe pattern suggests that bending modes are no longer present at the head of the pulse. The pictures obtained by Sutton (21) appear to confirm this supposition. A very interesting feature of frame 5 is the pronounced curvature of the fringes which implies that plane sections of the bar are warping. The remaining frames, beginning with frame 6, show very complex and confused fringe patterns of unknown origin. They are probably due to short-wavelength, high-frequency waves travelling in the metal and to associated coating thickness effects. Since dispersion is not so important near the point of impact, high-frequency waves are expected to be strongly present very early in the wavetrain.

In figure 8 the quiescent state is not present making it impossible to determine the starting time after impact of this frame sequence. Triggering difficulties which were not considered beforehand are responsible for this. Since the hammer is approximately 9/16 inch from the bar when the trigger pulse is generated by the velocity pickup, approximately 1340 microseconds elapse before the hammer strikes the bar as compared to 8 microseconds for the resulting strain wave to come into the field of view. Since the wave front travels out of view in 15 microseconds, the delay time must be accurate to within one percent if the wave front is to be observed. Complicating the situation is the fact that the hammer velocity is not a priori reproducible to more than one or two feet per second which gives rise to uncertainties of perhaps 80 microseconds, making it nearly impossible to correctly set the delay time beforehand. In view of this it is surprisingly good luck that the wavefront is observed in figure 7. Since the wave front is not observable as a reference, little can be said about figure 8; it is interesting, however, to note the pronounced curvature of the fringes in certain frames.

Further experiments are required to determine whether the fringe patterns truly represent the surface strains of the metal; however, several interesting observations can be made from the motion pictures which were obtained. The fringe pattern appears to travel with the metal wave velocity, which is reassuring. The pronounced concave curvature of the leading fringes with respect to the direction of wave propagation indicates that plane sections of the bar are warping for relatively long-wavelength waves. If there was no warpage, the fringes would have no curvature. Since dynamic photoelasticity can give some qualitative insight into elastic wave propagation, it is interesting to note that this fringe curvature is present

to some degree in all the full-field dynamic photoelastic fringe patterns which have been obtained for the longitudinal impact of rectangular bars. Concave curvatures of the leading fringes with respect to the direction of wave propagation are observed in the pictures of Sutton (21) and Feder, et al. (23). In the pictures of Durelli, et al. (26,27), the curvature continuously changes from concave to convex as the fringe order increases to its maximum value. No explanations as to why the curvature of the leading fringe, for example, should be concave rather than convex are offered in the literature. In the next part, Part III, mathematical expressions will be obtained which qualitatively describe the observed fringe patterns.

Conclusions and Recommendations

In view of serious doubts about the usefulness of dynamic photoelasticity for quantitatively modeling transient stress distributions in metals, an alternative approach using birefringent coatings applied to actual metal specimens has been considered. An experimental program was undertaken to determine whether it would be technically possible to photograph the transient fringe patterns. The results of experiments using a rectangular aluminum bar coated with PhotoStress and the Ellis ultra-high-speed camera indicate that transient fringe patterns resulting from impact can be successfully photographed using existing film and light sources at exposure times of 0.05 microseconds. Pronounced fringe curvatures observed in the pictures indicate that plane sections of the bar were warping during the passage of the strain pulse. Similar fringe curvatures are observed in dynamic photoelastic pictures obtained by other investigators for the longitudinal impact of rectangular bars.

Before taking further pictures, it is recommended that the relationship between coating birefringence and surface strain as a function of frequency be experimentally investigated for varying thicknesses of promising coatings. To this end a longitudinal elastic wave would be introduced into a long circular aluminum bar by a strong aerodynamic shock wave generated by a shock tube. At a station more than twenty diameters from the loaded end of the bar, two effects of the wave would be observed simultaneously on a dual-beam oscilloscope: one, the time variation of the strains at the surface of the bar using either piezoelectric or solid state strain gages; the other, the time variation of the corresponding fringe order in a birefringent coating of given thickness, observed by a photocell as alternate extinction and transmission of a beam of polarized monochromatic light reflected from the bar through the coating. A round bar is used because its symmetry allows the strain gage and coating to be arranged around the circumference of the bar at the same station. Also, when the coating is applied to the bar, several accurate thicknesses can be easily produced using a lathe. As will be pointed out in Part III, analytical solutions for the surface strain response of a circular bar subjected to an axial pressure step are available which are in excellent agreement with experimental results for stations more than twenty diameters down the bar. Due to dispersion, the operative frequencies and wavelengths respectively increase and decrease during the passage of the wave; by comparing the oscilloscope traces, the birefringent response for a particular coating thickness can be observed as a function of time and frequency in relation to the surface strain. Also, by using calibrated strain gages, the strain-optical coefficient can be evaluated from the strain-time trace and a plot of the fringe order as

a function of time.

Simultaneously, a search for birefringent materials having higher strain-optical sensitivities should be undertaken in order that photographically significant fringe orders can be obtained with very thin coatings. It has already been pointed out that physical chemists working in this area feel confident that materials can be developed which are an order of magnitude more sensitive than existing epoxy resins (37).

Assuming that high sensitivity materials can be found and that for sufficiently thin coatings of such materials the birefringence represents the surface strains of the metal for a substantial frequency range, it is suggested that several improvements for photographing the transient fringe patterns be considered. From the high-speed pictures obtained in the present investigation it is clear that better resolution is required if fringe pattern details around discontinuities are to be investigated. Since the total observation time will generally be quite short, Professor Ellis has suggested that it might be practicable to use a modified Cranz-Schardin system in which a set of separately pulsed Kerr cell shutters and a corresponding number of image forming beams in juxtaposition would give a small number of large-negative pictures spaced in time. The light source would be at constant intensity during the duration of the picture taking. In conjunction with such a system it might be worthwhile to consider incorporating the reflectance method of fringe multiplication originated and used by Post (40,17). Multiplied fringe patterns would greatly improve the numerical evaluation of the strains; however, they may be difficult to obtain since the fringe multiplication is accompanied by a considerable loss in light

intensity.

If excellent fringe photographs which accurately represent the surface strains of the metal part are obtained, it will be possible to establish the difference of principal strains over the coated surface. However, the problem remains of determining the individual principal strains over the surface of the metal structure or part. In static systems the only body force present is the weight of the structure, which is usually negligible compared to the external forces. For this case the maximum strains generally occur on the boundaries of the structure. In sharp contrast, inertial body forces in a dynamic system are often greater than the external forces, and the maximum strains need not occur along boundaries. The common integration and iteration procedures for the determination of interior strains, as used in static photoelasticity, are not applicable to dynamic problems. All of these methods require that body forces be negligible.

Since the thickness change of a plane stress part is proportional to the sum of the principal strains, it may be possible to use interferometric techniques to experimentally obtain fringe patterns of equal thickness change in a plane stress part. The individual principal strain values could then be obtained by simple addition and subtraction of the sums and differences of the principal strains. The new solid-state laser devices are promising light sources for interferometers.

III. LONGITUDINAL ELASTIC STRAIN WAVE PROPAGATION IN WIDE RECTANGULAR BARS: THEORETICAL CONSIDERATIONS

The Physical Problem

In Part II, the time sequence of isochromatic fringe photographs obtained for an aluminum bar of rectangular cross section impacted at one end revealed that the leading fringe was markedly concave with respect to the direction of wave propagation. It was noted that this concavity implies that plane sections of the bar are warping during the passage of the strain wave. In the present section, Part III, mathematical expressions based on approximate equations of motion will be developed for describing this warping.

The physical problem which will be approximated is the determination of the elastic strains in a long bar of rectangular cross section having stress-free lateral surfaces, subject to the conditions that a uniform normal stress with a step-function time dependence is applied to the end and that the shear stresses applied to the end are zero.

Background

Inasmuch as there is very little information in the literature concerning rectangular bars, it will be advantageous to begin by surveying existing techniques and solutions for describing the propagation of longitudinal strain waves in cylindrical bars. This survey will serve to introduce concepts and techniques which will be carried over into the present analysis. Then, the work which has been done on rectangular bars will be discussed.

Although the basic equations of motion for an elastic body form a system of linear partial differential equations, it is a difficult task

to obtain exact solutions which satisfy given boundary and initial conditions for even the most simply shaped bounded body. The relative ease with which reasonable approximate solutions to such a problem can be obtained depend on the distribution and rate of application of the input, and on the geometry of the body.

Considering the behavior of a long elastic bar subjected to time-dependent loading on one end, it is convenient to think in terms of the longitudinal strain pulse which propagates away from the stressed end. The elementary plane wave theory predicts that the strain pulse should propagate along the bar without appreciable change in shape and, consequently, the strain at any position along the bar should vary with time in essentially the same way as the applied load.* It has been shown experimentally by Davies (41) that this is a reasonable prediction only when the force producing the pulse is applied relatively slowly. For rapid rates of loading it is observed that the strain pulse spreads out during travel and develops oscillations which have no counterpart in the applied force.

In discussing the cause of this dispersion in a cylindrical bar, Davies (41) called attention to the early theoretical work of Pochhammer and Chree (cf. (42)) on the propagation of sinusoidal waves in a bar of infinite length where all stresses and strains are symmetric about the axis of the bar. In order to separate variables, Pochhammer and Chree

---

* In the elementary rod theory, the axial stress and strains are assumed to be uniformly distributed over the cross section of the bar. It is easily shown that longitudinal strains should travel at "bar velocity" $c_o = (E/\rho)^{1/2}$, where E is Young's modulus and ρ is the density of the bar material.

considered product solutions of the form $g(r)\, e^{i(\gamma z - \omega t)}$, where z is a distance along the bar axis and r is a radial distance. The homogeneous boundary conditions of zero stress at the lateral surface $r = a$ of the bar restrict the possible values of the wave number γ (= 2π divided by the wavelength) for a given angular frequency ω. The restricting relation is a transcendental secular equation called "the Pochhammer frequency equation". According to this equation, γ is a non-linear, multiple valued function of ω. Each permissible value of γ for a particular frequency ω is associated with a particular "mode of vibration".

Davies suggested that a pulse in a bar of semi-infinite or finite length could be considered as the superposition of "Pochhammer waves" of all frequencies. Inasmuch as γ is not directly proportional to ω, each component of a pulse made up of such waves should travel with a difference phase velocity c (= ω / γ). The relative phases of the individual waves should therefore change with time causing the shape of the resultant pulse to vary during propagation along the bar. It has been shown by several investigators (41,43,44,45) that this is an adequate basis for predicting pulse behavior at large distances from the loaded end of the bar. These investigators found agreement between measured values for the periods of oscillation and the values predicted by a group velocity analysis based on numerical solutions (e.g. (46,41)) of the Pochhammer frequency equation.

Adem (47) treated the steady state wave propagation in an infinite elastic cylindrical rod due to a delta function body force in the z-direction which varies harmonically in time. Fox (45) expanded Adem's solution to include a step function time dependence and presented solutions for

large distances down the bar. Fox's problem is interesting because his numerical results for large z agree so well with his experimental results which were obtained for a zero shear stress and a uniform normal stress suddenly applied to the end of a semi-infinite cylindrical bar. Folk (48) introduced a double transform method to solve the problem of determining the elastic strains in a semi-infinite cylindrical bar with a stress free lateral surface, subject to the end conditions that the stress applied normally to the end is uniform and has a step function time dependence and that the radial displacement at the end is always zero. For large distances down the bar, the strain solutions correspond with those of Fox (45). Skalak (49) examined the problem in which all points on the end of a semi-infinite cylindrical bar are suddenly given a velocity whose axial component is known and constant. The end stresses were unspecified in this problem except that their tangential component was taken to be zero.

The above solutions essentially constitute approximate solutions of the exact equations of motion. Another approach which has yielded important contributions to the theory is based on devising approximate equations of motion which exhibit the long wave behavior of the lower modes of the Pochhammer frequency equation. The principal approximate theories are the Love equation (50), the Mindlin-Herrmann theory (51), and the Bishop (52)-Sutton (21) theory which all preserve the long wave behavior of the lowest mode of the Pochhammer frequency equation. Davies (41) used the Love equation and Miklowitz (53,54,55) used the Mindlin-Herrmann theory in solving longitudinal impact and pressure shock problems in semi-infinite bars. Miklowitz (55) has compared these three approximate theories and concludes that the Mindlin-Herrmann theory gives the

best approximation for long distances down the bar. All of these theories are based on the fundamental assumption of plane sections remaining plane. A more recent approximate theory proposed by Mindlin and McNiven (56) allows for the warping of plane sections and closely approximates the first few modes of the Pochhammer frequency equation; however, it has not been used for the solution of transient wave propagation problems.

As mentioned earlier, very little work has been done on wave propagation in rectangular bars when the wavelength is of the same magnitude as the lateral dimensions. This is not unexpected since the specification of an additional characteristic length makes the rectangular bar problem an order of magnitude more complicated than the corresponding circular bar problem. As suggested above, the circular bar problem is still not completely analyzed, especially in the region of the bar extending from the loaded end to a distance of perhaps twenty diameters.

Morse (57) experimentally measured the compressional wave velocity in rectangular brass bars of different width-to-thickness ratios as a function of frequency by means of standing wave patterns made visible by the use of lycopodium powder. An X-cut quartz crystal was used to excite the various resonant modes between frequencies of 200 and 650 kc. Considering only the lowest modes of vibration he found that the dispersion curves are made up of two branches with a discontinuity occurring in one of them when the half wavelength is close to the larger dimension. It was demonstrated that the lower branch was associated with the width mode and the upper branch with the thickness mode. The discontinuity in the thickness mode was characterized by an infinite phase velocity corresponding to a "cut-off" frequency.

Approximate solutions which described the experimental results quite well were formulated by Morse (58) from the general elastic equations of motion. Two general modes of propagation were constructed which satisfied the boundary conditions for the free vibrations of a long bar of "wide" rectangular cross section (i.e., a bar for which the width is considerably greater than the thickness). The thickness mode was shown to have an infinite phase velocity at a cut-off frequency occurring when the thickness mode is in resonance in the width dimension. For frequencies below the cut-off frequency no transmission takes place in the thickness mode, the waves decaying exponentially.* An analogous phenomenon occurs in the propagation of electromagnetic waves in a wave guide (e.g. (60)). The phase velocity of both modes approaches that of Rayleigh surface waves when the wavelengths are much smaller than the lateral dimensions.

Recently, Mindlin and Fox (61) have obtained exact solutions of the elastic equations for a family of modes of vibration in an infinite rectangular bar having stress-free lateral surfaces for particular ratios of width to thickness. A set of points and associated slopes were found on the branches of the complete frequency versus wave number spectrum. The complete solution was not obtained and it was pointed out that the complete solution cannot be expressed in terms of a finite number of elementary functions.

---

* Hok (59) has presented an interesting discussion of this situation and a general classification of elastic waves in solids in the appendix of his paper.

Assumptions

The problem stated above is extremely formidable; however, by introducing several reasonable assumptions based on the experimental and theoretical studies discussed above, a mathematically tractable approximate theory can be used which presumably retains the important physical features of the problem. Experimental evidence will provide the final test of the validity of the assumptions.

It will be assumed that the bar is made of a homogeneous, isotropic, dissipationless material and that the classical elastic equations of motion govern its behavior. The analysis will be restricted to a wide rectangular bar, i.e. a bar for which the width-to-thickness ratio is large, which is semi-infinite in length. For such a bar, the following assumptions are introduced: (i) A state of plane stress exists in the plane of the bar defined by the width and the length dimensions. (ii) At large distances down the bar the "pure" end conditions stated above may be replaced by "mixed" end conditions specifying that the applied normal stress is uniform and has a step function time dependence and that the lateral displacement at the end of the bar is always zero. The implications of these two assumptions will be discussed in detail.

If the bar is sufficiently thin, the deformations may be regarded as uniform over its thickness. Since the normal and shearing stresses are zero at both surfaces, the corresponding stress components must be small throughout the thickness of the bar, and it is therefore convenient to take them as approximately zero everywhere in the bar. Under these conditions, the bar can be regarded as a two-dimensional medium (an "elastic strip"), of zero thickness. Taking the displacement vector $\vec{s}$ to be a two-dimensional vector, the plane stress equations of motion can

be written in the two-dimensional vector form (cf. (62))

$$\text{grad div } \vec{s} - \frac{1}{2}(1-\sigma)\,\text{curl curl } \vec{s} = \frac{\rho(1-\sigma^2)}{E}\,\frac{\partial^2 \vec{s}}{\partial t^2}, \qquad (1)$$

where all the vector operators are two dimensional. E and σ are the elastic parameters describing the medium.

Before proceeding it should be noticed that the formal transformation

$$E \to \frac{E}{1-\sigma^2} \qquad \text{and} \qquad \sigma \to \frac{\sigma}{1-\sigma} \qquad (2)$$

converts equation 1 into the corresponding plane strain equation of motion for an infinite thick plate. This important observation implies that results and techniques used in investigating plate problems can be utilized in analyzing the elastic strip. Bishop (63) has compared the two cases for elastodynamic problems. His calculations on the lowest mode of the respective frequency equations indicate that the above transformation shifts the roots of the plane stress frequency equation. For very long waves the limiting plane strain phase velocity is plate velocity $c_p = \sqrt{\frac{1}{(1-\sigma^2)}\,\frac{E}{\rho}}$, whereas bar velocity $c_o = \sqrt{\frac{E}{\rho}}$ is the limiting plane stress phase velocity. The higher velocity in the plane strain case results from the effective stiffening of the medium due to the motional restraint provided by the infinite extent of material perpendicular to the direction of wave propagation. For very short waves, the limiting plane strain phase velocity is that of Rayleigh surface waves and the limiting plane stress phase velocity closely approximates Rayleigh surface wave velocity. Gazis and Mindlin (64) discussed the long wavelength phase velocity behavior in the transition region between the states of plane stress and plane strain (i.e., for arbitrary width-to-thickness

ratios) on the basis of approximate equations of motion.

At this point, it is also appropriate to note the mathematical similarity between the symmetrical vibrations of an infinite isotropic elastic plate (state of plane strain) and the corresponding vibrations discussed earlier for a circular elastic bar. This similarity has been pointed out by Holden (65). The theoretical developments for the plate parallel those quoted for the cylindrical bar. However, very little experimental work has been done on the plate and for this reason it was considered more satisfying to initially discuss the cylindrical rod for which considerable effort has been expended in correlating experiment and analysis. The theoretical work for the elastic plate will be discussed as the need for it arises in analyzing the elastic strip.

Equation 1, based on the assumption of plane stress, is the lowest order approximate theory that might describe the experimentally observed warping of plane sections. In the work of Kane and Mindlin (66), it is pointed out that the plane stress theory gives a good approximation in plates provided the operative wavelengths are long compared to the plate thickness. For bars, Morse's experimental work (57), which was discussed earlier, indicates that for frequencies below a cut-off frequency no propagation takes place in the thickness mode and that the dispersion is closely predicted by the plane stress theory. This cut-off frequency occurs when the thickness mode is in resonance in the width dimension, i.e., when the half wavelength is equal to the bar width. It will be assumed, then, that the plane stress theory yields a good approximation for a wide rectangular bar provided the half wavelengths involved are greater than the bar width. Due to dispersion this will be

the case at long distances down the bar for a period of time following the arrival of the initial signal.

Regarding the second assumption in which pure end conditions were replaced by mixed end conditions, it is necessary to turn to the theoretical and experimental work of Folk, Fox, Shook and Curtis (48) and the theoretical studies of Folk (67). The agreement between theory based on mixed end conditions and experiment based on pure end conditions for large distances down the bar has already been noted. Folk considered a semi-infinite slab (state of plane strain) with stress free lateral surfaces subject to the end conditions that the stress applied normally is **uniform with a step function** time dependence and that the lateral end displacement is taken as a Fourier sine series having arbitrary coefficients. The plan was to carry this arbitrary series into the stress expressions, set the shear stress equal to zero at the end, and subsequently determine the coefficients. Unable to solve for the coefficients, Folk then considered the case where only one coefficient is retained which allowed him to make the shear stress zero along two lines on the slab edge. This solution was compared with the solution in which the lateral end displacement is everywhere zero. The percentage difference between the two was shown to be negligible for low frequencies. This result is anticipated from the static problem. If a slab is statically loaded at its end with a shearing force (which is an odd function across the thickness and thus in static equilibrium), it has been shown (e.g. (68)) that the slab deformation will decrease rapidly with distance from the edge. The conclusions of these and other arguments suggest that the initial signal for large distances down a bar depends only on the normal end stress,

and is little affected by applied shear stresses. On the basis of these arguments, it is assumed that the replacement of the pure end conditions by mixed end conditions will yield a good approximation at long distances down the bar provided that the wavelength is long and the applied normal stress is left unchanged.

It is important to note that these two assumptions are valid in the same region of the space-time domain.

Statement of the Mathematical Problem

The physical problem under consideration and the assumptions which are introduced to render it mathematically tractable have been discussed above. Using rectangular Cartesian coordinates having x along and y at right angles to the centerline of the strip, the plane stress equations of motion written in terms of the areal dilatation Δ and the rotation Ω are

$$\frac{\partial \Delta}{\partial x} - (1 - \sigma) \frac{\partial \Omega}{\partial y} = \frac{\rho(1 - \sigma^2)}{E} \frac{\partial^2 u}{\partial t^2} , \tag{3}$$

$$\frac{\partial \Delta}{\partial y} + (1 - \sigma) \frac{\partial \Omega}{\partial x} = \frac{\rho(1 - \sigma^2)}{E} \frac{\partial^2 v}{\partial t^2} , \tag{4}$$

where

$$\Delta = \frac{\partial u}{\partial x} + \frac{\partial v}{\partial y} , \tag{5}$$

$$2\Omega = \frac{\partial v}{\partial x} - \frac{\partial u}{\partial y} . \tag{6}$$

In these equations u and v are longitudinal and transverse particle displacements, respectively, t is time, ρ is the material density, E is Young's modulus, and σ is Poisson's ratio; Δ and Ω are defined by equations 5 and 6, respectively.

Solutions to these equations must satisfy the following conditions:

(i) the initial conditions at $t = 0$,

$$u(x,y,0) = v(x,y,0) = \frac{\partial u}{\partial t}(x,y,0) = \frac{\partial v}{\partial t}(x,y,0) = 0, \tag{7}$$

which reflect the assumed initial state of rest of the strip;

(ii) the boundary conditions at the lateral edges of the strip, where $y = \pm a$ (the half-width of the strip),

$$\tau_{yy}(x, \pm a, t) = \tau_{xy}(x, \pm a, t) = 0 ; \tag{8}$$

(iii) the input boundary conditions at the end of the strip, $x = 0$,

$$\tau_{xx}(0,y,t) = - P_o S(t), \tag{9a}$$

$$v(0,y,t) = 0 ; \tag{9b}$$

(iv) the displacements and stresses must vanish

as x approaches infinity. (10)

In equation 9a P_o is the applied pressure and $S(t)$ is a step function in time. The stress components τ_{xx}, τ_{yy}, and τ_{xy} are related to the displacements by the stress-strain equations for plane stress,

$$\tau_{xx} = \frac{E}{1 - \sigma^2}\left(\frac{\partial u}{\partial x} + \sigma \frac{\partial v}{\partial y}\right), \tag{11}$$

$$\tau_{yy} = \frac{E}{1 - \sigma^2}\left(\frac{\partial v}{\partial y} + \sigma \frac{\partial u}{\partial x}\right), \tag{12}$$

$$\tau_{xy} = \frac{E}{2(1 + \sigma)}\left(\frac{\partial u}{\partial y} + \frac{\partial v}{\partial x}\right). \tag{13}$$

The coordinate system and the boundary conditions are illustrated in figure 9.

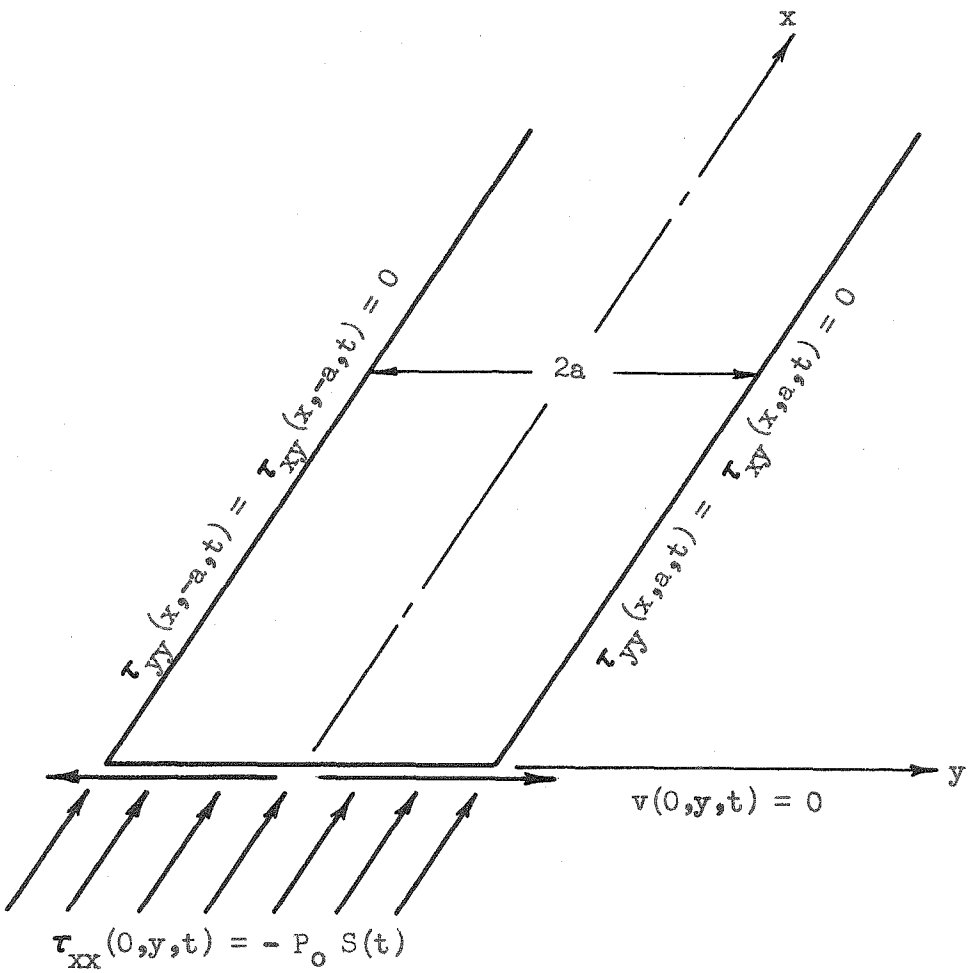

Figure 9. Coordinate system and boundary conditions.

Method of Solution

The boundary value problem posed above lends itself to the double transform method of solution used by Folk (48,67,69)*.

If Fourier exponential, sine, and cosine transforms are applied to equations 3 through 6, it is possible to introduce the initial conditions and the end boundary conditions at $x = 0$. The transforms applied to a particular differential equation are chosen in such a way that only the available initial and end boundary information is required. The following transforms, notation, and terminology are introduced.

$$\text{Sine transform} \quad f^S(\gamma,y,t) = \int_0^\infty f(x,y,t)\sin(\gamma x)dx, \tag{14}$$

$$\text{Cosine transform} \quad f^C(\gamma,y,t) = \int_0^\infty f(x,y,t)\cos(\gamma x)dx, \tag{15}$$

$$\text{Fourier transform} \quad f^F(\gamma,y,\omega) = \int_0^\infty f(\gamma,y,t)\, e^{i\omega t}dt. \tag{16}$$

The transforms of the derivatives of a function for each of the above transforms have particular properties which will determine when each transform is to be used. These properties are

$$\left(\frac{\partial f}{\partial x}\right)^S = -\gamma f^C, \tag{17}$$

$$\left(\frac{\partial f}{\partial x}\right)^C = -f(0,y,t) + \gamma f^S, \tag{18}$$

$$\left(\frac{\partial^2 f}{\partial t^2}\right)^F = -\frac{\partial f}{\partial t}(\gamma,y,0) + i\omega f(\gamma,y,0) - \omega^2 f^F. \tag{19}$$

---

* A concise discussion of integral transforms and their inversion formulae is given by Tranter (70).

For future reference, the inversion formulas for the three transforms are

$$f(x,y,t) = -\frac{i}{\pi}\int_{-\infty}^{\infty} f^S(\gamma,y,t)\, e^{i\gamma x}\, d\gamma \ , \tag{20}$$

$$f(x,y,t) = \frac{1}{\pi}\int_{-\infty}^{\infty} f^C(\gamma,y,t)\, e^{i\gamma x}\, d\gamma \ , \tag{21}$$

$$f(x,y,t) = \frac{1}{2\pi}\int_{-\infty+i\varepsilon}^{\infty+i\varepsilon} f^F(x,y,\omega)\, e^{-i\omega t}\, d\omega \ . \tag{22}$$

Solution Transforms

To exclude x, the cosine transformation is applied to equations 3 and 6 and the sine transformation to equations 4 and 5. Using the transform properties of equation 17 and 18, this gives

$$[-\Delta(0,y,t) + \gamma \Delta^S] - (1-\sigma)\frac{\partial \Omega^C}{\partial y} = \frac{\rho(1-\sigma^2)}{E}\frac{\partial^2 u^C}{\partial t^2} \ , \tag{23}$$

$$\frac{\partial \Delta^S}{\partial y} - (1-\sigma)\gamma\,\Omega^C = \frac{\rho(1-\sigma^2)}{E}\frac{\partial^2 v^S}{\partial t^2} \ , \tag{24}$$

$$\Delta^S = -\gamma\, u^C + \frac{\partial v^S}{\partial y} \ , \tag{25}$$

$$2\Omega^C = -v(0,y,t) + \gamma\, v^S - \frac{\partial u^C}{\partial y} \ . \tag{26}$$

The functions $\Delta(0,y,t)$ and $v(0,y,t)$ are obtained from the end conditions 9, by using equation 5 and the stress-strain relation of equation 11;

$$v(0,y,t) = 0 \quad \text{and} \quad \Delta(0,y,t) = -\frac{(1-\sigma^2)}{E}\, P_o\, S(t). \tag{27}$$

The explicit forms (27) for $v(0,y,t)$ and $\Delta(0,y,t)$ are substituted in equations 23 through 26.

The variable t is excluded and the initial conditions 7 are introduced by applying the Fourier transformation to the equations resulting from the above substitution. To secure the existence of the integrals, the imaginary part of ω is taken to be greater than zero.

$$-\rho \frac{(1-\sigma^2)}{E} \omega^2 u^{CF} = i \frac{(1-\sigma^2)}{E\omega} P_o + \gamma \Delta^{SF} - (1-\sigma) \frac{d\Omega^{CF}}{dy}, \quad (28)$$

$$-\rho \frac{(1-\sigma^2)}{E} \omega^2 v^{SF} = \frac{d\Delta^{SF}}{dy} - (1-\sigma)\gamma \Omega^{CF}, \quad (29)$$

$$\Delta^{SF} = -\gamma u^{CF} + \frac{dv^{SF}}{dy}, \quad (30)$$

$$2\Omega^{CF} = \gamma v^{SF} - \frac{du^{CF}}{dy}. \quad (31)$$

The transformed displacements are obtained from equations 28 and 29 in terms of Δ^{SF} and Ω^{CF}.

$$u^{CF} = \frac{E}{\rho(1-\sigma^2)\omega^2} \left[-\gamma \Delta^{SF} + (1-\sigma) \frac{d\Omega^{CF}}{dy}\right] - \frac{iP_o}{\rho\omega^3}, \quad (32)$$

$$v^{SF} = \frac{E}{\rho(1-\sigma^2)\omega^2} \left[-\frac{d\Delta^{SF}}{dy} + (1-\sigma)\gamma \Omega^{CF}\right]. \quad (33)$$

Substitution of equations 32 and 33 into equations 30 and 31 leads to two linear ordinary uncoupled differential equations in Δ^{SF} and Ω^{CF}.

$$\frac{d^2\Delta^{SF}}{dy^2} + h^2\Delta^{SF} = i \frac{(1-\sigma^2)}{E\omega} \gamma P_o \quad (34)$$

and

$$\frac{d^2 \Omega^{CF}}{dy^2} + k^2 \Omega^{CF} = 0, \tag{35}$$

where

$$h^2 = \rho \frac{(1-\sigma^2)}{E} \omega^2 - \gamma^2 \quad \text{and} \quad k^2 = 2\rho \frac{(1+\sigma)}{E} \omega^2 - \gamma^2. \tag{36}$$

The solutions of these equations are

$$\Delta^{SF} = A(\gamma, \omega) \sin(hy) + B(\gamma, \omega) \cos(hy) + \frac{i(1-\sigma^2)\gamma P_o}{E \omega h^2}, \tag{37}$$

$$\Omega^{CF} = C(\gamma, \omega) \sin(ky) + D(\gamma, \omega) \cos(ky). \tag{38}$$

For the coordinate system and symmetric boundary conditions of figure 1, it is concluded from physical arguments that

$$\Delta^{SF}(y) = \Delta^{SF}(-y) \qquad \text{and} \qquad \Omega^{CF}(y) = -\Omega^{CF}(-y),$$

and consequently,

$$A(\gamma, \omega) = D(\gamma, \omega) = 0. \tag{39}$$

Equations 37, 38, and 39 are next substituted into equations 32 and 33 to obtain expressions for the particle displacements;

$$u^{CF} = \frac{E}{\rho(1-\sigma^2)\omega^2} [-\gamma B(\gamma, \omega)\cos(hy) + (1-\sigma)k\, C(\gamma, \omega)\cos(ky)] - \frac{iP_o}{\rho \omega^3} \left(1 + \frac{\gamma^2}{h^2}\right), \tag{40}$$

$$v^{SF} = \frac{E}{\rho(1-\sigma^2)\omega^2} [h\, B(\gamma, \omega)\sin(hy) + (1-\sigma)\gamma C(\gamma, \omega)\sin(ky)]. \tag{41}$$

To evaluate $B(\gamma, \omega)$ and $C(\gamma, \omega)$ the transformed boundary conditions corresponding to $\tau_{yy}(x, \pm a, t) = \tau_{xy}(x, \pm a, t) = 0$ must be introduced. Taking the sine-Fourier transform of equation 12 and the cosine-Fourier transform of equation 13 and using the end condition 9b gives

$$\tau_{yy}^{SF} = \frac{E}{1-\sigma^2}\left(\frac{dv^{SF}}{dy} - \sigma\gamma u^{CF}\right), \tag{42}$$

$$\tau_{xy}^{CF} = \frac{E}{2(1+\sigma)}\left(\frac{du^{CF}}{dy} + \gamma v^{SF}\right). \tag{43}$$

The transformed boundary conditions at $y = \pm a$ remain homogeneous,

$$\tau_{yy}^{SF}(\gamma, \pm a, \omega) = \tau_{xy}^{CF}(\gamma, \pm a, \omega) = 0. \tag{44}$$

Substituting equations 40 and 41 for u^{CF} and v^{SF} into equations 42 and 43 and then substituting the resulting expressions into equation 44, two linear simultaneous algebraic equations result.

$$(k^2-\gamma^2)\cos(ha)\,B(\gamma, \omega) + 2(1-\sigma)\gamma k\cos(ka)\,C(\gamma, \omega) = \frac{-2iP_o\rho\sigma(1+\sigma)(1-\sigma^2)\gamma\omega}{E^2h^2}, \tag{45}$$

and

$$2\gamma h\sin(ha)\,B(\gamma, \omega) - (1-\sigma)(k^2-\gamma^2)\sin(ka)\,C(\gamma, \omega) = 0. \tag{46}$$

Equations 45 and 46 are solved for $B(\gamma, \omega)$ and $C(\gamma, \omega)$;

$$B(\gamma, \omega) = \frac{-2iP_o\rho\sigma(1-\sigma)(1+\sigma)^2\gamma(k^2-\gamma^2)\omega\sin(ka)}{E^2h^2\,F(\gamma, \omega)} \tag{47}$$

and

$$C(\gamma, \omega) = \frac{-4iP_o \rho \sigma (1+\sigma)^2 \gamma^2 \omega \sin(ha)}{E^2 h F(\gamma, \omega)} , \tag{48}$$

where

$$F(\gamma,\omega) = (k^2-\gamma^2)^2 \sin(ka)\cos(ha) + 4\gamma^2 h k \sin(ha)\cos(ka). \tag{49}$$

The equation $F = 0$ is the frequency equation for the free vibrations of an infinite isotropic elastic strip of vanishing thickness (state of plane stress). Under the formal transformation 2 this equation is identical to the frequency equation given by Rayleigh (71) for the symmetric vibrations of an infinite isotropic elastic plate (state of plane strain). This fact is utilized in subsequent development.

For comparison with the experimental results described in Part IV, values are required for the strain components e_{xx}, e_{yy}, and e_{xy} where

$$e_{xx} = \frac{\partial u}{\partial x} , \tag{50}$$

$$e_{yy} = \frac{\partial v}{\partial y} , \tag{51}$$

$$e_{xy} = \frac{\partial v}{\partial x} + \frac{\partial u}{\partial y} . \tag{52}$$

The transformed strains in terms of the transformed displacements are obtained by taking the sine-Fourier transform of equations 50 and 51 and the cosine-Fourier transform of equation 52.

$$e_{xx}^{SF} = - \gamma u^{CF} , \tag{53}$$

$$e_{yy}^{SF} = \frac{dv^{SF}}{dy} , \tag{54}$$

$$e_{xy}^{CF} = \gamma v^{SF} + \frac{du^{CF}}{dy} . \tag{55}$$

The end condition 9b was used in arriving at equation 55.

Substituting equations 40, 41, 47, and 48 into equations 53, 54 and 55 gives the transformed strains for the specific problem under consideration;

$$e_{xx}^{SF} = \frac{-2iP_o \sigma (1+\sigma)\gamma^3(k^2-\gamma^2)\sin(ka)\cos(hy)}{E\omega h^2 F(\gamma,\omega)} + \frac{4iP_o \sigma (1+\sigma)\gamma^3 k \sin(ha)\cos(ky)}{E\omega h F(\gamma,\omega)} + \frac{i(1-\sigma^2)\gamma P_o}{E\omega h^2} , \tag{56}$$

$$e_{yy}^{SF} = \frac{-2iP_o \sigma (1+\sigma)\gamma(k^2-\gamma^2)\sin(ka)\cos(hy)}{E\omega F(\gamma,\omega)} - \frac{4iP_o \sigma (1+\sigma)\gamma^3 k \sin(ha)\cos(ky)}{E\omega h F(\gamma,\omega)} , \tag{57}$$

$$e_{xy}^{CF} = \frac{4iP_o \sigma (1+\sigma)\gamma^2(k^2-\gamma^2)}{E\omega h F(\gamma,\omega)} [\sin(ha)\sin(ky)-\sin(ka)\sin(hy)] . \tag{58}$$

Inversion of the Transforms and Discussion of the Frequency Equation

1. Preliminary discussion of the inverse sine and cosine transforms of e_{xx}^{SF}, e_{yy}^{SF}, and e_{xy}^{CF}

The inverse sine transforms of e_{xx}^{SF} and e_{yy}^{SF} and the inverse cosine transform of e_{xy}^{CF} are expressed in the following integral forms by using equations 20 and 21, respectively:

$$e_{xx}^{F} = -\frac{i}{\pi} \int_{-\infty}^{\infty} e_{xx}^{SF}(\gamma, y, \omega)\, e^{i\gamma x}\, d\gamma \,, \tag{59}$$

$$e_{yy}^{F} = -\frac{i}{\pi} \int_{-\infty}^{\infty} e_{yy}^{SF}(\gamma, y, \omega)\, e^{i\gamma x}\, d\gamma \,, \tag{60}$$

$$e_{xy}^{F} = \frac{1}{\pi} \int_{-\infty}^{\infty} e_{xy}^{CF}(\gamma, y, \omega)\, e^{i\gamma x}\, d\gamma \,. \tag{61}$$

These integrals may be evaluated by applying Cauchy's residue theorem in the complex γ-plane. For each integral the path of integration is closed by adding a semicircle of infinite radius about the origin in the upper half of the complex γ-plane. The closing arcs for the integrals of equations 59, 60, and 61 are denoted by C_1, C_2, and C_3, respectively.

If the various trigonometric functions in e_{xx}^{SF} are replaced by their respective infinite series, it is found that only even powers of h and k appear; hence, there are no branch points in the complex γ-plane even though h and k are irrational functions of γ. Similarly, it can be shown that this conclusion is applicable to e_{yy}^{SF} and e_{xy}^{CF}.

In order to investigate the effect of adding a closing arc, γ is written in polar coordinates, $\gamma = Re^{i\theta}$, where $0 \leq \theta \leq \pi$. By applying Jordan's lemma it can be shown that the integrals over the infinite semicircles C_1 and C_2 are zero for $x > 0$ and $0 \leq y \leq a$. For large R, $x > 0$, and $0 < y < a$, it can be shown that the integrand of the

complex integral formed from equation 61 is of negative exponential order (Me^{-aR}) for $0 \leq \theta \leq \pi$; thus, the contribution from C_3 vanishes. For $y = 0$ and $y = a$, e_{xy}^{SF} identically vanishes.

Thus, since the integral over the infinite semicircle C_1 is zero, the original integral of equation 59 is $2\pi i$ times the sum of the residues of the poles in the upper half of the γ-plane. Similar statements apply to the evaluation of the integrals in equations 60 and 61.

Although the functions e_{xx}^{SF}, e_{yy}^{SF}, and e_{xy}^{CF} appear at first glance to have poles for $h = 0$, each function can be defined to be analytic at this point. The only poles of these functions occur for the values of γ which satisfy the frequency equation

$$F(\gamma, \omega) = 0. \tag{62}$$

Since F is a function of both the wave number γ and the frequency ω, the position of a pole in the γ-plane depends on the value used for ω and thus defines the functions $\gamma = \gamma(\omega)$. Anticipating the inverse Fourier transforms (see equation 22) in which the integrations over ω will be taken limitingly close to, but just above, the real axis in the complex ω-plane, the frequency to be used for calculating the poles takes on values $\mathrm{Re}\,\omega + i\varepsilon$, where $\mathrm{Re}\,\omega$ varies from $-\infty$ to $+\infty$ and ε is vanishingly small but positive.

To complete the inversions in the complex γ-plane, it is necessary to answer such questions as whether the roots of the frequency equation are single so the poles are simple, and whether any of the roots lie on the real γ axis. The behavior of the solutions $\gamma = \gamma(\omega)$ of equation 62, a transcendental secular equation, is not immediately obvious.

A limited study of equation 62 will be undertaken to obtain sufficient information about its solutions to answer such questions as those above and others relevant to this problem.

2. The frequency equation

It has already been noted that equation 62 is identical to the classical Rayleigh frequency equation for symmetric vibrations if the transformation $E \to E/(1-\sigma^2)$ and $\sigma \to \sigma/(1-\sigma)$ is introduced. This fact will be utilized to infer much of the needed general behavior of the solutions to equation 62 from existing solutions of the Rayleigh frequency equation. The Rayleigh frequency equation has been intensively studied. The investigators include Rayleigh (71), Lamb (72), and others, and more recently Prescott (73), Cooper (74), Firestone (75), Morse (57, 58), Sato (76), Holden (65), Fay and Fortier (77), Bishop (63), Aggarwal and Shaw (78-81), Lyon (82), Tolstoy and Usdin (83,84), Mindlin and others (85-89), Folk (67), Sherwood (90), Pursey (91), Redwood (92), and others.

The following discussion of the solutions of equation 62 is based largely on the work of Mindlin (86) and of Folk (67) and summarizes the features important in the present problem. Specific calculations have been carried out when necessary.

The values of the wave number γ for a given value of frequency ω are restricted by the frequency equation

$$F = (k^2-\gamma^2)^2 \sin(ka)\cos(ha) + 4\gamma^2 h\, k \sin(ha)\cos(ka) = 0, \qquad (63)$$

where $k^2 = \frac{2\rho(1+\sigma)\omega^2}{E} - \gamma^2$ and $h^2 = \frac{\rho(1-\sigma^2)\omega^2}{E} - \gamma^2$.

The solution $k = 0$ is trivial.

The relation between the wave number and the frequency depends on certain physical properties of the strip; that is, on the elastic constants E and σ, the material density ρ, and the strip half width a.

For purposes of generality, the following dimensionless variables are introduced:

$$\alpha = \gamma a \qquad \text{and} \qquad \beta = \frac{a\omega}{c_s}, \tag{64}$$

where c_s, the shear wave velocity in an infinite medium, is given by $c_s^2 = \frac{E}{2(1+\sigma)\rho}$. In terms of these variables, equation 63 becomes

$$a^4 F = (\beta^2 - 2\alpha^2)^2 \sin\sqrt{\beta^2-\alpha^2}\ \cos\sqrt{\kappa\beta^2-\alpha^2}$$

$$+ 4\alpha^2 \sqrt{\beta^2-\alpha^2}\sqrt{\kappa\beta^2-\alpha^2}\ \sin\sqrt{\kappa\beta^2-\alpha^2}\ \cos\sqrt{\beta^2-\alpha^2} = 0, \tag{63'}$$

where $\kappa = \frac{1-\sigma}{2}$.* For a specified value of Poisson's ratio, the solutions of equation 63' are viewed as determining a set of functions $\alpha = \alpha(\beta)$.

Zero frequency solutions: The zero frequency solutions of equation 63' make a convenient starting point for studying these functions and for introducing some notation. The limiting behavior of the frequency equation is

---

* For the plane strain case, $\kappa = \frac{1-2\sigma}{2(1-\sigma)}$.

$$\lim_{\beta \to 0} \left[\frac{a^4 F}{i\alpha^2 \beta^2 (\kappa - 1)} \right] = 2\alpha + \sinh 2\alpha = 0. \qquad (65)$$

Equation 65 defines the values of $\alpha = \alpha(\beta)$ for $\beta = 0$. The first few roots of this equation are illustrated in figure 10.

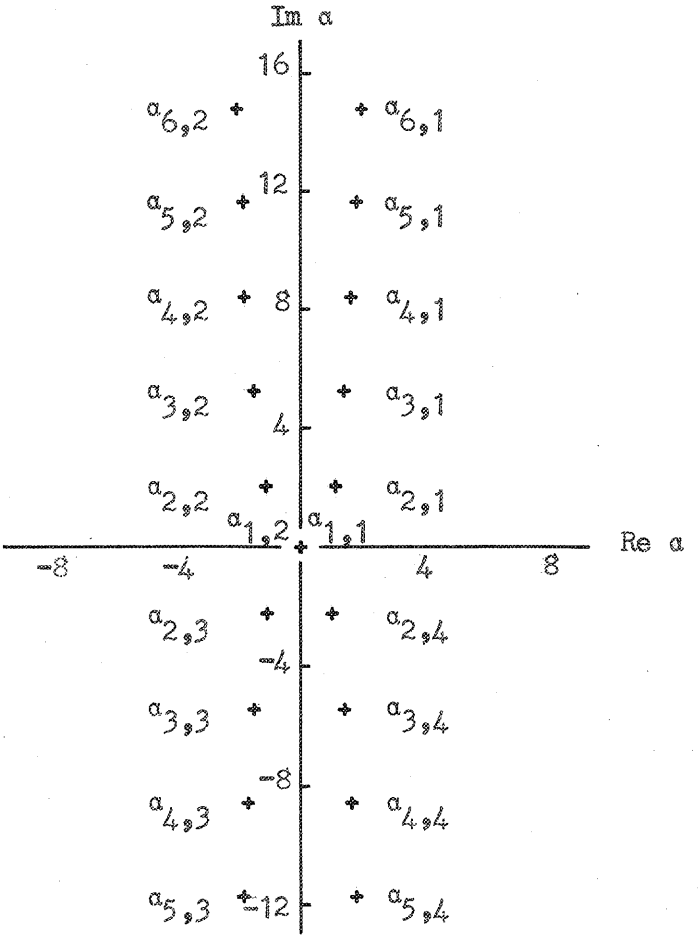

Figure 10. Zero frequency solutions of equation 63'.

It will be convenient to use the scheme introduced by Folk (67) for labelling the roots. A root is identified as $\alpha_{r,s}(0)$ where r orders the root according to its absolute value and s gives its quadrant in the complex α-plane. Roots with larger absolute values will be referred to as higher modes. As indicated in figure 10, there are four roots with equal magnitudes, one in each quadrant. The only exception is the root $\alpha = 0$. It will be seen later from a series solution for β small, but non-zero, that it is a double root. The root for which $\frac{d\alpha}{d\beta}$ is positive is labelled $\alpha_{1,1}$, the other root is labelled $\alpha_{1,2}$.

The roots of equation 65 for large values of $|\alpha|$ in the first quadrant of the α-plane are approximately (cf. (67))

$$\alpha_{r,1} \cong \ln \sqrt{(4r-5)\pi} + i(2r-5/2)\pi, \tag{66}$$

where r, the modulus subscript of the roots, is large. Clearly there is a countably infinite number of such roots.

In addition to being an approximation to the solutions of equation 65, equation 66 is also applicable to equation 63'. This is apparent from the following argument: For a given value of β only those values of α are considered for which $|\beta/\alpha|$ is arbitrarily small. For this condition, equation 63' reduces to equation 65 which has the solutions given by equation 66. Therefore, it follows that there is a countably infinite set of solutions to equation 63'.

Since for a given finite β there are no roots of equation 66 on the axes for large $|\alpha/\beta|$, it follows that there is a finite number of roots on them.

Solutions for real β : The solutions of equation 63' for real values of β will be considered next. For real β, there are real

and imaginary as well as complex values of α which satisfy equation 63'. Aggarwal and Shaw (81) and Lyon (82) demonstrated the imaginary roots. Mindlin (86), in connection with his second order approximate equations for the extensional vibrations of elastic plates, established the existence of the complex roots. Sherwood (90) has also discussed the complex roots. The real roots represent propagated waves and the imaginary roots represent exponentially attenuated waves. The complex roots correspond to exponentially attenuated waves having a superimposed sinusoidal variation.

The final strain solutions in the present problem will be obtained by approximate methods requiring that x, the distance along the strip, be large; consequently, the strain contributions due to the complex and imaginary roots of the frequency equation will be negligible. For this reason only the qualitative behavior of the complex and imaginary solutions will be discussed. The major strain contributions will be due to the real roots; hence, these roots will be examined quantitatively.

Since equation 63' is invariant to the substitution of $-\beta$ for β, it is only necessary to calculate the roots for positive β. Also, only the roots in (and on the boundaries) of the first quadrant of the complex α-plane need to be computed since the symmetry of the $\alpha_{r,s}(0)$ roots exhibited in figure 10 is still present. The reasoning is as follows: If α is a solution, then $-\alpha$ is a solution since α appears in equation 63' only as α^2. Also α^*, the complex conjugate of α, is a solution since F is a real function of α for real β. It follows that $-\alpha^*$ is also a solution.

The functions $\alpha_{r,s}(\beta)$ will be defined as the analytic continuations of the roots $\alpha_{r,s}(0)$ as β varies continuously from zero.

The computation of roots to equation 63' is tedious unless machine methods are employed. However, Mindlin (85,86) has developed a very ingenious and simple process for sketching the real and imaginary solutions without extensive computations of the roots.

Mindlin showed that the frequency equation analogous to Rayleigh's frequency equation, but with mixed boundary conditions on the plate faces, is characterized by a simple set of uncoupled dilatational and distortional solutions. Relaxation from mixed to free boundaries gives Rayleigh's frequency equation. The simple solutions of the mixed boundary condition problem form upper and lower bounds of frequency and wave number for Rayleigh's equation. In addition, the Rayleigh solutions pass through certain intersections of the bounds. Mindlin (86) obtains explicit formulas for the ordinates, slopes, and curvatures for $\alpha = 0$ and for the coordinates and slopes at the intersection points for both the Rayleigh solutions and the bounds. This information permits detailed construction of the Rayleigh solutions. This work is, as noted previously, applicable to equation 63'.*

Mindlin's sketches of the Rayleigh solutions are valuable guides to

---

* The following correspondence table relates the notation of Mindlin (86) to that of the present problem.

Text		Mindlin
ω	→	ω
γ	→	ϵ
a	→	b
β	→	$\frac{\pi}{2}\,\omega/\omega_s \equiv \frac{\pi}{2}\,\Omega$
α	→	$(\pi/2)z$
κ	→	$1/e^2$

the overall behavior of the solutions of equation 63'.* Numerical calculations of the values of $\alpha_{1,1}(\beta)$, $\alpha_{2,1}(\beta)$, and $\alpha_{2,2}(\beta)$ in the ranges of β for which these roots are real were made for several values of σ using an IBM 704 computer programmed to essentially apply Newton's iterative method. The roots obtained converged to six or seven places. The derivatives were obtained by taking first and second differences of α and β. The results of these computations are summarized in Appendix A and figures 11 and 12. $\alpha_{1,1}(\beta)$ is real for all real values of β. $\alpha_{2,1}(\beta)$ has a branch point where $\frac{d\beta}{d\alpha}$ is zero for $\alpha > 0$ which corresponds to the intersection of $\alpha_{2,1}$ and $\alpha_{2,4}$. From numerical calculations carried out by Folk (67) for $\sigma = 1/2$, the real roots at this point can be expected to join smoothly to the complex roots forming the analytic continuation of the complex root $\alpha_{2,1}(0)$. Points of zero slope also occur for $\alpha = 0$.

Both Mindlin (86) and Sherwood (90) have analyzed the conditions for which complex branches intersect real and imaginary branches. Following Sherwood's analysis, the coordinate differences between any two closely adjacent points $[\beta_o, \alpha_o]$ and $[(\beta_o + \delta\beta), (\alpha_o + \delta\alpha)]$ lying on the branch line system are given by

$$\delta\beta = \left(\frac{d\beta}{d\alpha}\right)_o \delta\alpha + \frac{1}{2!}\left(\frac{d^2\beta}{d\alpha^2}\right)_o (\delta\alpha)^2 + \ldots , \qquad (67)$$

where each derivative of β with respect to α is evaluated at $[\beta_o, \alpha_o]$ and is single valued. When $\left(\frac{d\beta}{d\alpha}\right)_o$ is non-zero, equation

---

* Mindlin (86) exhibits the solution spectrum in his Figs. 2 and 3. His Fig. 4 and Table II summarize the effect of Poisson's ratio on the $\alpha_{2,s}$ solutions.

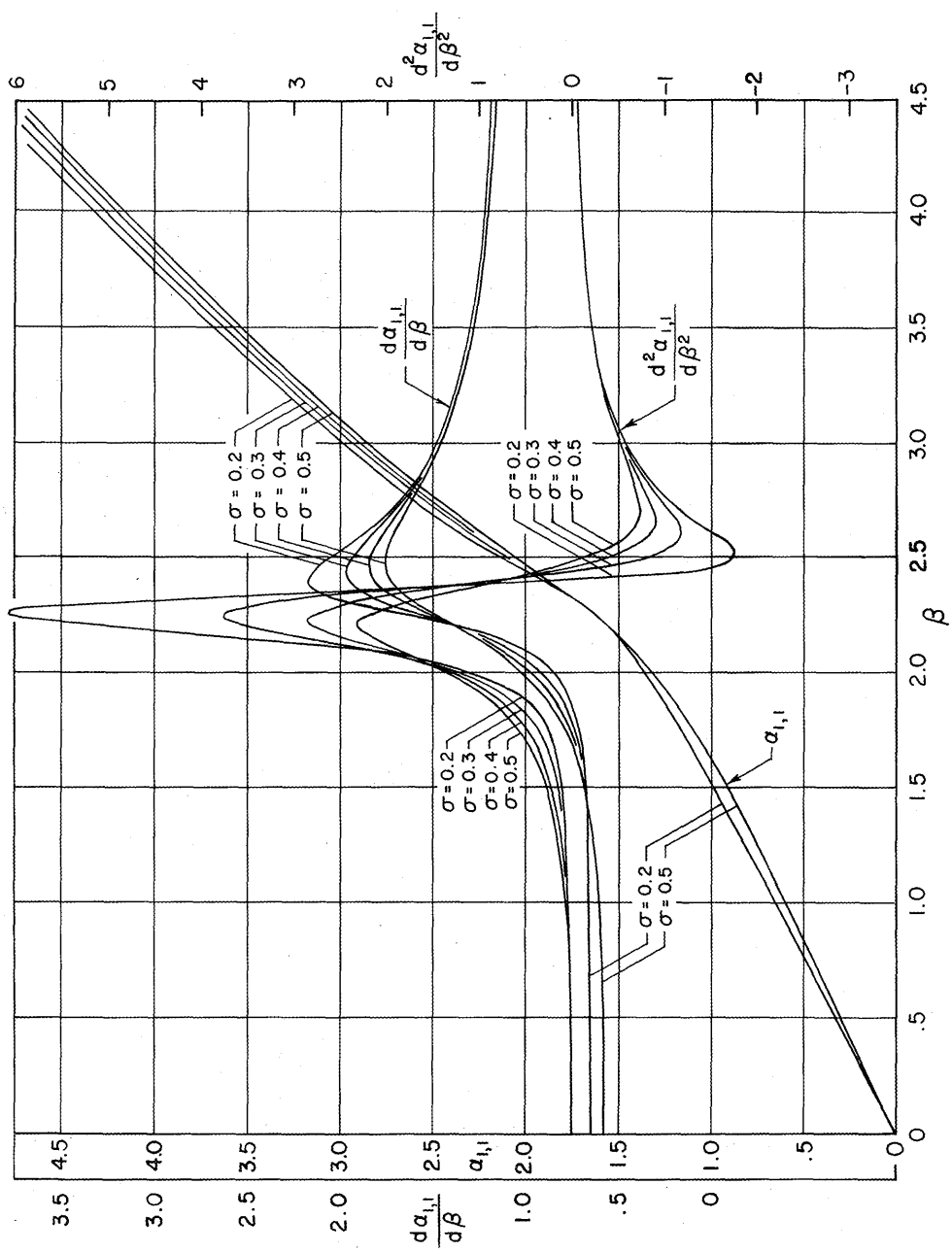

Figure 11. The solution $\alpha_{1,1}$ and its derivatives, $\frac{d\alpha_{1,1}}{d\beta}$ and $\frac{d^2\alpha_{1,1}}{d\beta^2}$, for real positive β and $\sigma = 0.2$, 0.3, 0.4, and 0.5.

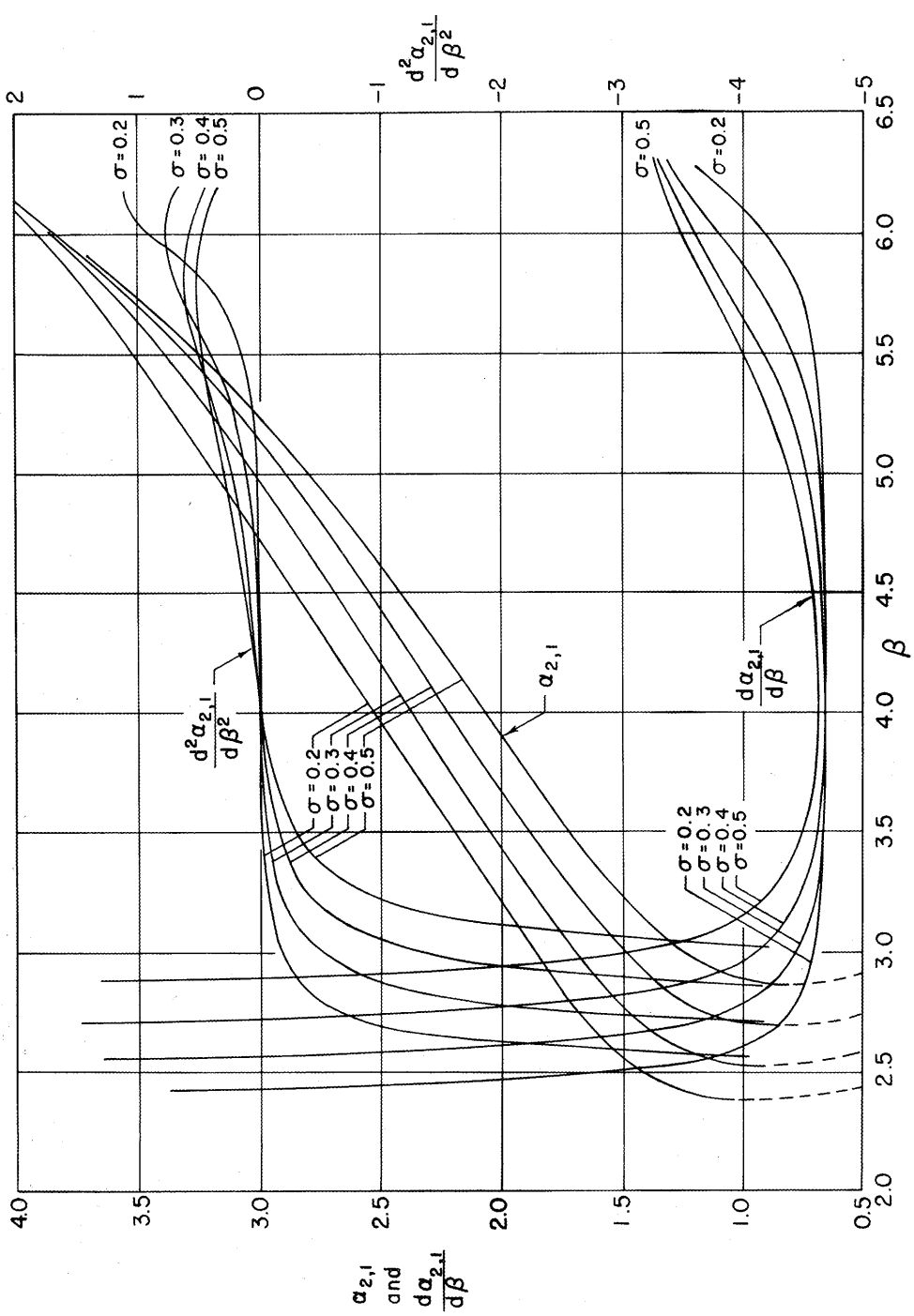

Figure 12. The solution $\alpha_{2,1}$ and its derivatives, $\frac{d\alpha_{2,1}}{d\beta}$ and $\frac{d^2\alpha_{2,1}}{d\beta^2}$, in the region of real positive β corresponding to real $\alpha_{2,1}$ for $\sigma = 0.2$, 0.3, 0.4, and 0.5.

67 gives the approximate linear relationship $\delta\beta \cong \left(\frac{d\beta}{d\alpha}\right)_o \delta\alpha$ indicating that only one branch line passes through the point $[\beta_o, \alpha_o]$ (e.g., see point A in figure 13). At any point where $\left(\frac{d\beta}{d\alpha}\right)_o$ is zero but $\left(\frac{d^2\beta}{d\alpha^2}\right)_o$ is nonzero (for example, see point B in figure 13), equation 67 gives the approximate quadratic relationship $\delta\beta \cong \frac{1}{2!}\left(\frac{d^2\beta}{d\alpha^2}\right)_o (\delta\alpha)^2$. Since $\delta\beta$ must be real, $\delta\alpha$ can be only real or imaginary. Therefore, at such a point two branches of approximately parabolic form intersect orthogonally with their axes oppositely directed in the positive and negative β directions. From this analysis, it is concluded that complex modes intersect real or imaginary branches at each point for which $\frac{d\beta}{d\alpha}$ is zero. If $\frac{d\beta}{d\alpha}$ is zero for $\alpha = 0$, imaginary branches intersect real branches.

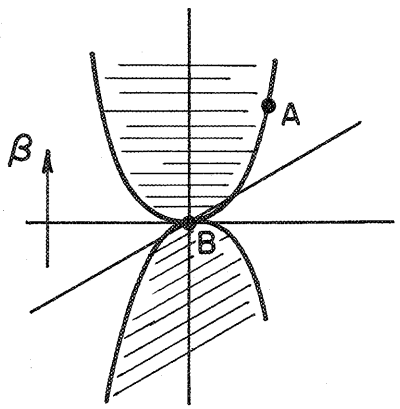

Figure 13. Intersection of branch lines.

From the calculations shown in figure 12, from asymptotic solutions which will be given later, and from the above branch point analysis, it is apparent that one branch has a positive slope and the other a negative slope for $|\beta| > \beta_{b.p.}$, the branch point value for $\alpha > 0$. $\alpha_{2,1}$ for $|\beta| > \beta_{b.p.}$ is defined as the branch with positive slope, and $\alpha_{2,4}$ is defined as the other branch. Due to the symmetry properties of the frequency equation, $\alpha_{2,2}$ and $\alpha_{2,3}$ also intersect for the same critical

value of frequency; $\alpha_{2,2}$ is chosen as the branch with positive slope. The $\alpha_{2,4}$ branch has branch points when $\alpha = 0$ corresponding to intersections of $\alpha_{2,2}$ and $\alpha_{2,4}$; $\alpha_{2,2}$ is taken as the branch with positive slope as above. At each branch point the analytic continuation of the solutions is defined so that roots having a positive slope when they are real have a positive imaginary component when they are complex. Figure 14 illustrates qualitatively the behavior of the $\alpha_{2,s}$ solutions for β real and $0 < \sigma < \frac{1}{2}$.

For reasons which will become apparent later, the major contributions to the strains e_{xx}, e_{yy}, and e_{xy} come from the modes $\alpha_{r,s}$ for $r = 1$ and 2; consequently, their behavior will be summarized in view of the above definitions.

$\alpha_{1,1}$ is a monotonic odd function of β passing through the origin and having a positive slope for all β. To examine the behavior of $\alpha_{1,1}$ for small β, a series expansion $\alpha_{1,1}^2 = \sum_{n=1}^{\infty} A_n \beta^{2n}$ is assumed. Substituting this series into equation 63' and evaluating the first few coefficients gives

$$\alpha_{1,1}^2 = \frac{\beta^2}{4(1-\kappa)} + \frac{(1-2\kappa)^2\beta^4}{48(1-\kappa)^2} + \frac{(1-2\kappa)^2(7-4\kappa^2)\beta^6}{2880(1-\kappa)^3} + \cdots ,$$

or

$$\alpha_{1,1} = \frac{\beta}{2(1-\kappa)^{1/2}} + \frac{(1-2\kappa)^2\beta^3}{48(1-\kappa)^{3/2}} + \frac{(1-2\kappa)^2}{576(1-\kappa)^{5/2}}\left[\frac{(7-4\kappa^2)}{5} - \frac{(1-2\kappa)^2}{4}\right]\beta^5 + \cdots , \tag{68}$$

where $\kappa = \frac{1-\sigma}{2}$.

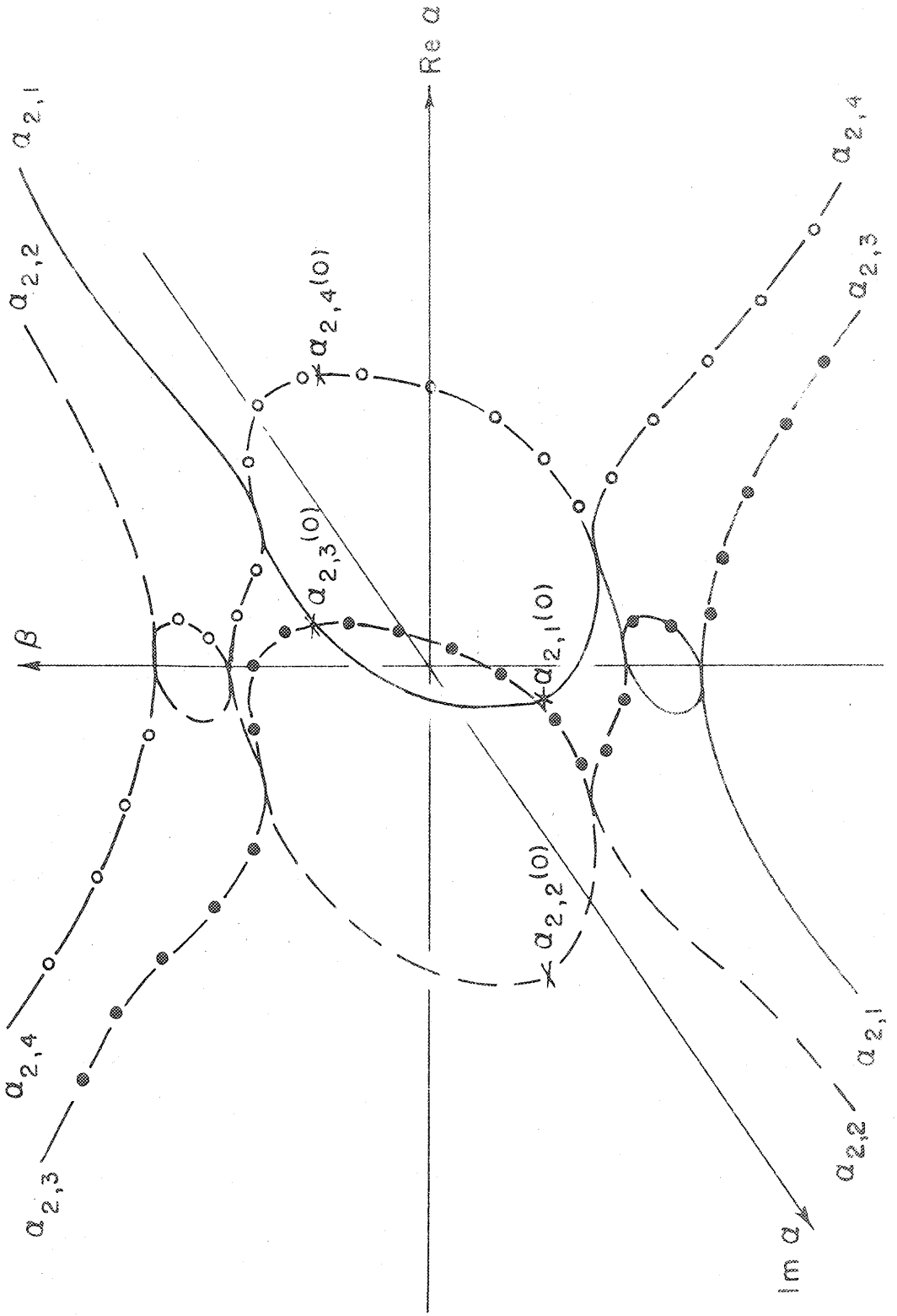

Figure 14. Qualitative behavior of the functions $\alpha_{2,s}$ for real β and $0 < \sigma < 1/2$.

This series can be used to evaluate $\alpha_{1,1}$ for small β. As mentioned above, values of $\alpha_{1,1}$ for larger β were numerically calculated. Figure 11 shows that the function approaches a linear behavior, $\alpha = \left(\frac{1}{m_1}\right)\beta$, for large β. Assuming this behavior, it can be shown that m_1 is the real root, in the range $0 < m < 1$, of the equation

$$m^6 - 8m^4 + 8(3 - 2\kappa)m^2 - 16(1 - \kappa) = 0, \tag{69}$$

which has the form of the Rayleigh surface wave equation. Thus

$$\frac{\alpha_{1,1}}{\beta} \cong \frac{1}{m_1} = \frac{c_s}{c_R}, \tag{70}$$

for large β, where c_R closely approximates Rayleigh surface wave velocity.* In this case both h and k approach i∞ as β increases.

Knowing the behavior of $\alpha_{1,1}$, $\alpha_{1,2}$ is determined by the relation $\alpha_{1,2}(\beta) = -\alpha_{1,1}(\beta)$.

Much of the behavior of $\alpha_{2,1}$ has already been discussed. The behavior of $\alpha_{2,2}$, $\alpha_{2,3}$, and $\alpha_{2,4}$ can be obtained from the $\alpha_{2,1}$ solution due to the symmetry properties of equation 63' mentioned above. In the region of β for which the solutions are complex,

$$\alpha_{2,1}(\beta) = -\alpha^*_{2,2}(\beta) = -\alpha_{2,3}(\beta) = \alpha^*_{2,4}(\beta). \tag{71a}$$

---

* The value of m_1 for a given σ can be obtained from Fig. 2-5 of Ewing, Jardetzky, and Press (93). For the plane stress case κ ($=\frac{1-\sigma}{2}$) is computed, equated to $\frac{1-2\sigma}{2(1-\sigma)}$ and a ficticious σ is obtained. Entering Fig. 2-5 for this value, m_1 is given by the c_R/β curve. (For the plane strain case, Fig. 2-5 is entered for the true value of σ).

When the solutions are imaginary and real, the symmetry conditions and the definitions of the roots when passing through the branch points give

$$\alpha_{2,1}(-\beta) = \alpha_{2,2}(\beta) = \alpha^{*}_{2,3}(-\beta) = \alpha^{*}_{2,4}(\beta) \quad \text{for the imaginary} \tag{71b}$$

solutions, and,

$$\alpha_{2,1}(\beta) = -\alpha_{2,2}(-\beta) = -\alpha_{2,3}(\beta) = \alpha_{2,4}(-\beta) \quad \text{for the real} \tag{71c}$$

solutions.

The asymptotic solutions for $\alpha_{2,1}$ (and for $\alpha_{r,s}$ having $r \geq 2$) are characterized by ha approaching $i\infty$ and ka approaching $n\pi$, where the n are properly chosen integers.* Assuming a series of the form $\alpha/\beta = \sum_{n=0}^{\infty} B_n/\beta^n$, substituting it into equation 63', and evaluating the first few coefficients subject to the restrictions on ha and ka gives

$$\alpha_{2,1} \cong \beta - \frac{2\pi^2}{\beta} + \dots , \tag{72}$$

for β large and negative. For β large and positive,

$$\alpha_{2,1} \cong \beta - \frac{\pi^2}{2\beta} + \dots . \tag{73}$$

The behavior of $\alpha_{2,1}$ as β varies from $-\infty$ to $+\infty$ can now be summarized. $\alpha_{2,1}$ increases smoothly from the asymptotic value of equation 72 and remains real until a branch point on the β axis is encountered, where $\alpha_{2,1}$ becomes positive imaginary until another branch point on the β axis, but closer to the origin, is reached and $\alpha_{2,1}$ again becomes real and increases smoothly until a branch

---

* The criterion for choosing n is established by a generalization of arguments given by Folk (67).

point at $\beta = -|\beta_1|$ and Re $\alpha = \alpha_1 > 0$ is reached. $\alpha_{2,1}$ then becomes complex with a positive imaginary component and remains complex until the branch point at $\beta = +|\beta_1|$ and Re $\alpha = \alpha_1 > 0$ is reached, where it again becomes real and approaches the asymptotic value given by equation 73.

The behavior of the solutions $\alpha_{r,s}(\beta)$ for $r = 3,4,5,\ldots$ will not be discussed in detail. The qualitative behavior of the real and imaginary roots of equation 63' can be seen from the sketch by Mindlin (86) (see his Fig. 3) for the corresponding roots of the Rayleigh frequency equation. Complex branches intersect the real branches at points of zero slope of the latter. When $\alpha = 0$, pure imaginary branches intersect the real arms since, usually, the latter have zero slope at $\alpha = 0$. Complex branches emanate from points of zero slope on the imaginary branches. However, Mindlin (86) has shown that whereas there are at most two points of zero slope on each real branch, there are certain imaginary branches which have an infinite number of such points. Folk (67) has speculated on how the higher modes $\alpha_{r,s}$ for $r = 3,4,\ldots$ are to be constructed from these real, imaginary, and complex branches. It will be seen later that these modes are relatively unimportant in the present problem and it will be assumed that they can be constructed according to the definitions given previously; that is, the $\alpha_{r,s}(\beta)$ solutions are defined to be the analytic continuations of the $\alpha_{r,s}(0)$ solutions, and the $\alpha_{r,s}(\beta)$ solutions for $s = 1$ and 2 are defined to have positive slopes when they are real and positive imaginary components when they are complex or imaginary.

Solution behavior for complex β: Folk (67) has discussed briefly several features of the analytic behavior of the solutions to

Rayleigh's frequency equation when β is complex, and his remarks can be generalized to apply to the solutions of equation 63'. However, the infeasibility of detailed analysis forced him to assume much of the solution behavior. This unsatisfactory procedure, of assuming much of the analytic behavior of the roots, will be continued here.

The functions $\alpha_{r,s}$ can be shown to have no pole-like singularities in the finite β plane. This is proved by assuming a pole exists; then, a neighborhood of this pole must exist such that $|\alpha/\beta|$ is arbitrarily large. It has already been noted that the solution to the frequency equation for very large $|\alpha/\beta|$ reduces to equation 66,

$$\alpha_{r,1} \cong \ln \sqrt{(4r-5)\pi} + i(2r - \tfrac{5}{2})\pi .$$

Hence, $|\alpha|$ cannot continuously become arbitrarily large for finite β, which implies that there are no poles.

The limiting behavior of $\alpha_{1,1}/\beta$ as $|\beta|$ becomes very large is revealing. If β is increased along the real β axis, it was found that $\lim_{\beta\to\infty} \frac{\alpha_{1,1}}{\beta} = \frac{1}{m_1}$ where $0 < m_1 < 1$. If β is increased along the imaginary β axis, it can be shown that

$$\lim_{\beta\to i\infty} \frac{\alpha_{1,1}}{\beta} \cong \kappa^{1/2} - \frac{\pi^2}{8\,\kappa^{1/2}\,\beta^2} + \cdots . \qquad (74)$$

Since the function $\alpha_{1,1}/\beta$ has different limits as β is increased along the real and imaginary β axes, it is concluded that it has an essential singularity at infinity. Further analysis suggests that the functions $\alpha_{r,s}/\beta$, for $r \geq 2$, also have essential singularities at infinity.

Summarizing, it has been found that the functions $\alpha_{r,s}$ defined by equation 63' have no poles, probably an infinity of them have essential singularities for β infinite, and all modes except $\alpha_{1,s}$ have branch points along the real β axis and probably along the imaginary β axis.

For the present problem, it will be assumed that $\alpha_{1,1}$ is analytic everywhere in the finite β plane. For the higher modes, it will be assumed that the only singularities are the branch points along the real and imaginary axes, and that analytic functions can be obtained by appropriate branch cuts.

3. Inverse sine and cosine transforms of e_{xx}^{SF}, e_{yy}^{SF}, and e_{xy}^{CF}

Having discussed the solutions of the frequency equation 63', it is now possible to complete the inversions of the sine and cosine transforms.

The position of the roots of equation 63' in the complex γ-plane depends on the value used for ω ; it has been shown that there are an infinite number of roots for a given ω . When the frequency is real, it was found that the frequency equation has real roots--the number depending on the frequency. However, the inverse Fourier transforms involve slightly complex frequencies, that is, $\omega = \omega_o + i\varepsilon$ where ε is a vanishingly small but positive number and ω_o varies from $-\infty$ to $+\infty$. The real roots $\gamma_{r,s} (= \alpha_{r,s}/a)$ of equation 63' when the frequency is real are shifted to slightly complex roots when the frequency is in the above range. From the Taylor series

$$\gamma_{r,s}(\omega_o + i\varepsilon) = \gamma_{r,s}(\omega_o) + \left(\frac{d\gamma_{r,s}}{d\omega}\right)_{\omega=\omega_o} (i\varepsilon) + \frac{1}{2!}\left(\frac{d^2\gamma_{r,s}}{d\omega^2}\right)_{\omega=\omega_o} (i\varepsilon)^2 + \dots , \quad (75)$$

it is seen that for ε very small and positive, the imaginary part of $\gamma_{r,s}(\omega_o + i\varepsilon)$ is positive or negative according to the sign of $\frac{d\gamma_{r,s}}{d\omega}$ evaluated for $\omega = \omega_o$. The functions $\gamma_{r,s}$ were defined so that the roots in the upper and lower halves of the complex γ-plane remain in the upper and lower halves, respectively, as ω_o varies from $-\infty$ to $+\infty$. Thus, when the frequency is in the range noted above, the roots of the frequency equation are all single and no roots lie on the real axis.

There is no doubt which roots to include in applying Cauchy's residue theorem to equations 59, 60, and 61; the integrals can be evaluated as sums of the residues for all the poles in the upper half of the γ-plane. Since $\gamma_{r,1}$ and $\gamma_{r,2}$ are always in the upper half of the γ-plane, the summations will include all roots with the second index 1 or 2, while the roots with the second index 3 or 4 are excluded. There is one exception to this rule: $\gamma_{1,1}$ is included but $\gamma_{1,2}$ is not.

Taking the residues of the poles according to the above rule and multiplying by $2\pi i$, e^F_{xx} becomes

$$e^F_{xx}(x,y,\omega) = i\frac{P_o}{E}\sum_{r,s}\phi_{xx}(\gamma_{r,s},y,\omega)\, e^{i\gamma_{r,s}x}, \tag{76}$$

where

$$\phi_{xx}(\gamma_{r,s},y,\omega) = \frac{4\sigma(1+\sigma)\gamma^3}{\omega h^2 \frac{\partial F}{\partial \gamma}} \left[2hk\sin(ha)\cos(ky) - (k^2 - \gamma^2)\sin(ka)\cos(hy)\right]\Bigg|_{\gamma=\gamma_{r,s}}. \tag{77}$$

Similarly,

$$e^{F}_{yy}(x,y,\omega) = -\frac{i\sigma P_o}{E} \sum_{r,s} \phi_{yy}(\gamma_{r,s},y,\omega)e^{i\gamma_{r,s}x} , \tag{78}$$

where

$$\phi_{yy}(\gamma_{r,s},y,\omega) = \frac{4(1+\sigma)\gamma}{\omega \frac{\partial F}{\partial \gamma}} \left[(k^2 - \gamma^2)\sin(ka)\cos(hy) + 2\gamma^2 \frac{k}{h} \sin(ha)\cos(ky)\right]\Bigg|_{\gamma=\gamma_{r,s}} , \tag{79}$$

and

$$e^{F}_{xy}(x,y,\omega) = \frac{P_o}{E} \sum_{r,s} \phi_{xy}(\gamma_{r,s},y,\omega)e^{i\gamma_{r,s}x} , \tag{80}$$

where

$$\phi_{xy}(\gamma_{r,s},y,\omega) = \frac{-8\sigma(1+\sigma)\gamma^2}{\omega h \frac{\partial F}{\partial \gamma}} (k^2 - \gamma^2) \left[\sin(ha)\sin(ky) - \sin(ka)\sin(hy)\right]\Bigg|_{\gamma=\gamma_{r,s}} . \tag{81}$$

In the above equations,

$$\frac{\partial F}{\partial \gamma} = -8\gamma(k^2 - \gamma^2)\sin(ka)\cos(ha) - \frac{a\gamma}{k} \frac{\omega^4}{c_s^4} \cos(ha)\cos(ka) + \frac{a\gamma}{h} \left[(k^2 - \gamma^2)^2 + 4\gamma^2h^2\right] \sin(ha)\sin(ka) + \frac{4\gamma}{hk} \left[2h^2k^2 - k^2\gamma^2 - h^2\gamma^2\right] \sin(ha)\cos(ka). \tag{82}$$

4. Inverse Fourier transforms of e^F_{xx}, e^F_{yy}, and e^F_{xy}

The inverse Fourier transforms of e^F_{xx}, e^F_{yy}, and e^F_{xy} are expressed in the following integral forms by means of the inversion formula 22:

$$e_{xx}(x,y,t) = \frac{1}{2\pi} \int_{-\infty + i\varepsilon}^{\infty + i\varepsilon} e^F_{xx}(x,y,\omega) e^{-i\omega t}\, d\omega \quad , \tag{83}$$

$$e_{yy}(x,y,t) = \frac{1}{2\pi} \int_{-\infty + i\varepsilon}^{\infty + i\varepsilon} e^F_{yy}(x,y,\omega) e^{-i\omega t}\, d\omega \quad , \tag{84}$$

$$e_{xy}(x,y,t) = \frac{1}{2\pi} \int_{-\infty + i\varepsilon}^{\infty + i\varepsilon} e^F_{xy}(x,y,\omega) e^{-i\omega t}\, d\omega \quad . \tag{85}$$

Each of these expressions involves an improper integral of an infinite sum. For frequencies in the range of integration, the terms in the series for the higher modes approach zero as $Me^{-2r\pi x}$, where r is the modulus subscript of the roots $\gamma_{r,s}(\omega)$. Thus, the infinite sums in the above expressions are uniformly convergent with respect to frequency, and so the order of integration and summation can be interchanged in each case. The inversion expressions become

$$e_{xx}(x,y,t) = -\frac{P_o}{E} \sum_{r,s} \frac{1}{2\pi i} \int_{-\infty + i\varepsilon}^{\infty + i\varepsilon} \phi_{xx}(\gamma_{r,s},y,\omega) e^{i(\gamma_{r,s}x - \omega t)}\, d\omega \quad , \tag{86}$$

$$e_{yy}(x,y,t) = \frac{\sigma P_o}{E} \sum_{r,s} \frac{1}{2\pi i} \int_{-\infty + i\varepsilon}^{\infty + i\varepsilon} \phi_{yy}(\gamma_{r,s},y,\omega) e^{i(\gamma_{r,s}x - \omega t)}\, d\omega \quad , \tag{87}$$

$$e_{xy}(x,y,t) = \frac{P_o}{E} \sum_{r,s} \frac{i}{2\pi i} \int_{-\infty + i\varepsilon}^{\infty + i\varepsilon} \phi_{xy}(\gamma_{r,s},y,\omega) e^{i(\gamma_{r,s}x - \omega t)}\, d\omega \quad , \tag{88}$$

where ϕ_{xx}, ϕ_{yy}, and ϕ_{xy} are given by equations 77, 79, and 81, respectively.

It will be convenient to rewrite these expressions in dimensionless form. In addition to α and β given by 64, the following dimensionless variables are introduced:

$$T = \frac{t}{\left(\frac{a}{c_s}\right)}, \qquad X = \frac{x}{a}, \quad \text{and} \quad Y = \frac{y}{a}. \tag{89}$$

In non-dimensional form, equations 86, 87, and 88 become

$$e_{xx}(X,Y,T) = \sum_{r,s} (I_{xx})_{r,s} \equiv$$

$$= -\frac{P_o}{E} \sum_{r,s} \frac{1}{2\pi i} \int_{-\infty+i\varepsilon}^{\infty+i\varepsilon} \theta_{xx}(\alpha_{r,s}, Y, \beta) e^{i(\alpha_{r,s}X - \beta T)} d\beta , \tag{90}$$

$$e_{yy}(X,Y,T) = \sum_{r,s} (I_{yy})_{r,s} \equiv$$

$$= \frac{\sigma P_o}{E} \sum_{r,s} \frac{1}{2\pi i} \int_{-\infty+i\varepsilon}^{\infty+i\varepsilon} \theta_{yy}(\alpha_{r,s}, Y, \beta) e^{i(\alpha_{r,s}X - \beta T)} d\beta , \tag{91}$$

$$e_{xy}(X,Y,T) = \sum_{r,s} (I_{xy})_{r,s} \equiv$$

$$= \frac{P_o}{E} \sum_{r,s} \frac{i}{2\pi i} \int_{-\infty+i\varepsilon}^{\infty+i\varepsilon} \theta_{xy}(\alpha_{r,s}, Y, \beta) e^{i(\alpha_{r,s}X - \beta T)} d\beta , \tag{92}$$

where $\theta_{xx} = (c_s/a)\phi_{xx}$, $\theta_{yy} = (c_s/a)\phi_{yy}$, and $\theta_{xy} = (c_s/a)\phi_{xy}$. (93)

$(I_{xx})_{r,s}$, $(I_{yy})_{r,s}$, and $(I_{xy})_{r,s}$ are defined in equations 90, 91, and 92, respectively. The path of integration is still $-\infty + i\varepsilon$ to $\infty + i\varepsilon$

since the change of variables only changes its scale.

The complexity of θ_{xx}, θ_{yy}, θ_{xy}, and the functions $\alpha_{r,s}$ makes it impossible, in general, to evaluate the integrals in equations 90, 91, and 92 by simple means. However, asymptotic solutions can be obtained which are valid for large values of X.

Evaluation of Strain Integrals by Asymptotic Methods

1. Saddlepoint methods of integration

Provided X is large, saddlepoint methods can be used to evaluate the integrals in equations 90, 91, and 92; however, the same approximation cannot be used to describe all portions of the pulse. Pertinent discussions of saddlepoint methods of integration have been given by Havelock (94), Jeffreys and Jeffreys (95), Cerrillo (96), and Brillouin (97). In preparation for the evaluation of the strain integrals, the saddlepoint methods will be discussed in relation to the representative integral

$$I = \frac{1}{2\pi i} \int G(\beta)\, e^{f(\beta)}\, d\beta \,, \tag{94}$$

where $f(\beta) = i[\alpha_{r,s}(\beta)X - \beta T]$ is an analytic function, $G(\beta)$ varies slowly compared with the exponential factor, and the integration follows a path in the complex β-plane.

The ordinary saddlepoint method: In this approximation the path of integration is deformed through the saddlepoints, defined by $f'(\beta) = \frac{df(\beta)}{d\beta} = 0$, along paths of steepest descent (Im $f(\beta)$ = constant) so that in the neighborhood of these points Re $f(\beta)$ is a large negative number. The second order saddlepoints are defined by

$$f'(\beta) = i[X \frac{d\alpha_{r,s}}{d\beta} - T] = 0, \quad \text{or} \quad \frac{d\alpha_{r,s}}{d\beta} = \frac{T}{X} . \tag{95}$$

For a fixed X and a given T, $\alpha_{r,s}$ and β are chosen from values consistent with the frequency equation 63' so that $\frac{d\alpha_{r,s}}{d\beta} = \frac{T}{X}$. A set of such values will be labelled $\bar{\alpha}_{r,s}$ and $\bar{\beta}$, and a point $\bar{\beta}$ in the complex β-plane identifies a saddlepoint.

The major contributions to the integral, then, come from the portions of the paths in the neighborhood of the saddlepoints and from any poles that are crossed in deforming the contour. The contributions of these poles are $2\pi i$ times their residues.

Approximate contributions from the saddlepoints are obtained by expanding $G(\beta)$ and $f(\beta)$ about a saddlepoint $\bar{\beta}$ and retaining only the most important terms. Taylor series expansions can be used if there are no poles or zeros near $\bar{\beta}$. In this case

$$G(\beta) \cong G(\bar{\beta}) \tag{96}$$

and

$$f(\beta) = i[\alpha_{r,s}X - \beta T] \cong i[(\bar{\alpha}_{r,s}X - \bar{\beta} T) + \frac{X}{2} \bar{\alpha}''_{r,s}(\beta - \bar{\beta})^2], \tag{97}$$

where $\bar{\alpha}''_{r,s}$ denotes the value of $\frac{d^2\alpha_{r,s}}{d\beta^2}$ at the point $\beta = \bar{\beta}$. It can be shown (e.g. Jeffreys and Jeffreys (95)) that the contribution of the saddlepoint $\bar{\beta}$ to the integral of equation 94 is

$$\frac{1}{i} \frac{G(\bar{\beta})\, e^{i(\bar{\alpha}_{r,s}X - \bar{\beta} T \pm \pi/4)}}{\sqrt{2\pi X |\bar{\alpha}''_{r,s}|}} , \tag{98}$$

where the plus sign is used if $\bar{\alpha}''_{r,s}$ is positive, the minus sign if

it is negative. In this method of integration $X|\bar{\alpha}''_{r,s}|$ must be "large" in order that the path of steepest descent is sufficiently steep. The ordinary saddlepoint (o.s.p.) method therefore gives an evaluation of the integral which is approximate but becomes better as X increases. The case when $|\bar{\alpha}''_{r,s}|$ is small will be discussed in the following section.

The extended saddlepoint method: If the integral of equation 94 is evaluated for a fixed X, $f(\beta) = i[\alpha_{r,s}(\beta)X - \beta T]$ is a function of time; consequently the positions of the saddlepoints are time dependent. When the saddlepoints are widely separated, the derivatives of $f(\beta)$ at a saddlepoint $\bar{\beta}$ vary slowly with time as $\bar{\beta}$ moves. At certain times, however, the second order saddlepoints collide to form a third order saddlepoint (cf. figure 21) for which the second derivative of $f(\beta)$ is zero. Consequently, during the time interval when the saddlepoints are close together, the o.s.p. method is inapplicable.

The extended saddlepoint (e.s.p.) method (cf. Cerrillo (96)), like the o.s.p. method, is based on the concept of deforming the path of integration so as to localize the contributions to the integral. In the o.s.p. method the integrand is expanded in a series around the moving saddlepoint; in the e.s.p. method the integrand is expanded in a series about the collision point $(f''(\beta) = 0)$ of two second order saddlepoints in the β-plane.

The function $f(\beta)$ is approximated in the e.s.p. method by the first four terms of its Taylor series expansion about the point $\bar{\bar{\beta}}$ where $f''(\beta) = 0$.

$$f(\beta) \cong f_0(\beta) = i[\bar{\alpha}_{r,s}X - \bar{\bar{\beta}}T + (X\bar{\alpha}'_{r,s} - T)(\beta - \bar{\bar{\beta}}) + \frac{X}{6}\bar{\alpha}'''_{r,s}(\beta - \bar{\bar{\beta}})^3]. \quad (99)$$

The path of integration is chosen so that $\exp[\frac{iX}{6}\bar{\bar{a}}'''_{r,s}(\beta-\bar{\bar{\beta}})^3]$ approaches zero exponentially along the path of steepest descent for large $|\beta|$. In the applications of the e.s.p. method to the present problem, $\bar{\bar{\beta}}$ and $\bar{\bar{a}}'''_{r,s}$ are real. When $\bar{\bar{a}}'''_{r,s}$ is positive, the paths extending from $\bar{\bar{\beta}}$ which satisfy this steepest descent condition are shown in figure 15a. Figure 15b shows the paths for negative $\bar{\bar{a}}'''_{r,s}$. (For small $|\beta-\bar{\bar{\beta}}|$ these are not the paths of steepest descent.)

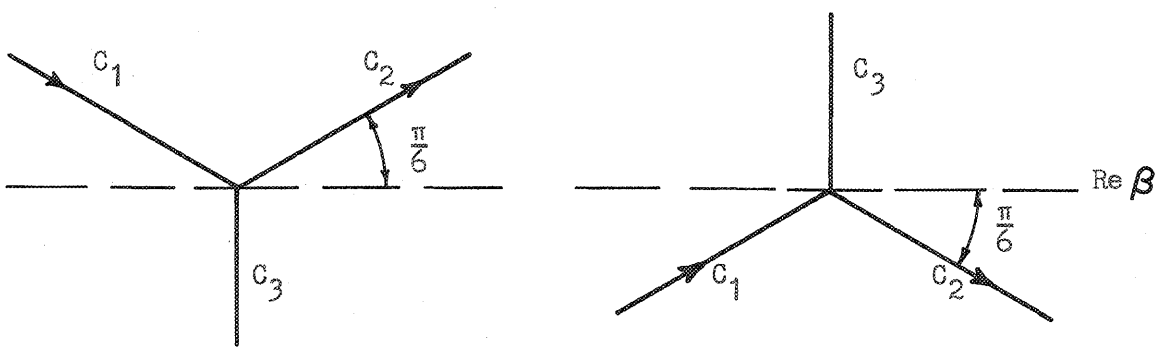

(a) $\bar{\bar{a}}'''_{r,s}$ positive

(b) $\bar{\bar{a}}'''_{r,s}$ negative

Figure 15. Integration paths for the extended saddlepoint method.

In each case the path of integration is chosen along C_1 to $\bar{\bar{\beta}}$ and back to infinity along C_2.

The remaining part of the integrand, $G(\beta)$, is expanded in a Laurent series about $\bar{\bar{\beta}}$, and then the integration is performed term by term. All of the typical terms which will arise in the present problem are included if $G(\beta)$ is approximated by

$$G(\beta) \cong \frac{G_{-1}}{\beta-\bar{\beta}} + G_o + G_1(\beta-\bar{\beta}) + G_2(\beta-\bar{\beta})^2 + G_3(\beta-\bar{\beta})^3 . \qquad (100)$$

To illustrate the procedure, the integration corresponding to the first term in this series will be performed in detail at the real saddlepoint $\bar{\beta}$. The integral may be written as

$$\frac{1}{2\pi i}\int_{C_1,C_2} \frac{G_{-1}e^{f_o(\beta)}\,d\beta}{\beta-\bar{\beta}} = \frac{G_{-1}}{2\pi i}\int_{C_1,C_2} \frac{1}{\Delta\beta}\, e^{i(A_1+B_1\Delta\beta+D_1\Delta\beta^3)}\,d\beta, \qquad (101)$$

where $A_1 = \bar{a}_{r,s}X - \bar{\beta}T$, $B_1 = X\bar{a}'_{r,s} - T$, $D_1 = \frac{X}{6}\bar{a}'''_{r,s}$, and $\Delta\beta = \beta - \bar{\beta}$. In the present problem, $\bar{a}'''_{r,s}$ is positive when this integral arises; hence, only the contour C_1,C_2 of figure 15a will be considered. If the substitution $\Delta\beta = \frac{\mu}{\sqrt[3]{3D_1}}$ is made, which shifts the contour C_1,C_2 and changes its scale, the integral becomes

$$G_{-1}e^{iA_1}\frac{1}{2\pi i}\int_{C_1,C_2}\frac{1}{\mu}\, e^{i(-B\mu+\mu^3/3)}\,d\mu , \qquad (102)$$

where

$$B = \left(\frac{2}{X\,\bar{a}'''_{r,s}}\right)^{1/3}(T - \bar{a}'_{r,s}X). \qquad (103)$$

The integral 102 may be written as

$$G_{-1}e^{iA_1}\left\{\frac{1}{2\pi i}\int_{C_1,C_2}\frac{1}{\mu}\, e^{i\mu^3/3}\,d\mu - \int_0^B\left[\frac{1}{2\pi}\int_{C_1,C_2} e^{i(-B\mu+\mu^3/3)}\,d\mu\right]dB\right\} , \qquad (104)$$

since

$$\frac{e^{-iB\mu}}{i\mu} = \frac{1}{i\mu} - \int_0^B e^{-iB\mu}\, dB. \tag{105}$$

Thus, the evaluation of the integral corresponding to the first term in equation 100 is

$$\frac{1}{2\pi i}\int_{C_1,C_2} \frac{G_{-1}\, e^{f_o(\beta)}\, d\beta}{\beta - \bar{\beta}} =$$

$$= -G_{-1} e^{i(\bar{a}_{r,s}X - \bar{\beta}T)}\left[\frac{1}{3} + \int_0^B \mathrm{Ai}(-\xi)\, d\xi\right], \tag{106}$$

where B is given by equation 103 and $\mathrm{Ai}(z) = \frac{1}{2\pi}\int_{C_1,C_2} e^{i(z\mu + \mu^3/3)}\, d\mu$.

The function $\mathrm{Ai}(z)$, called the Airy function, and its first derivative and integral have been tabulated for a wide range of z by Miller (98), Fox (45), and Tyler and Rouleau (99). The second and third derivatives can be calculated from the differential equation $\frac{d^2\mathrm{Ai}(z)}{dz^2} - z\mathrm{Ai}(z) = 0$. Appendix B summarizes these tabulations and calculations which are presented graphically in figures 16 and 17. The integrals corresponding to the remaining terms in equation 100 are evaluated for positive $\bar{a}'''_{r,s}$ in a generally similar manner. It is necessary to also consider negative $\bar{a}'''_{r,s}$ for the second term.

The evaluations are

$$\frac{1}{2\pi i}\int_{C_1,C_2} G_o e^{f_o(\beta)}\, d\beta = \frac{1}{i}\,\frac{G_o e^{i(\bar{a}_{r,s}X - \bar{\beta}T)}}{\sqrt[3]{\frac{X}{2}|\bar{a}'''_{r,s}|}}\; \mathrm{Ai}(\mp B), \tag{107}$$

where the negative sign is used in $\mathrm{Ai}(\mp B)$ when $\bar{a}'''_{r,s}$ is positive and the positive sign when it is negative.

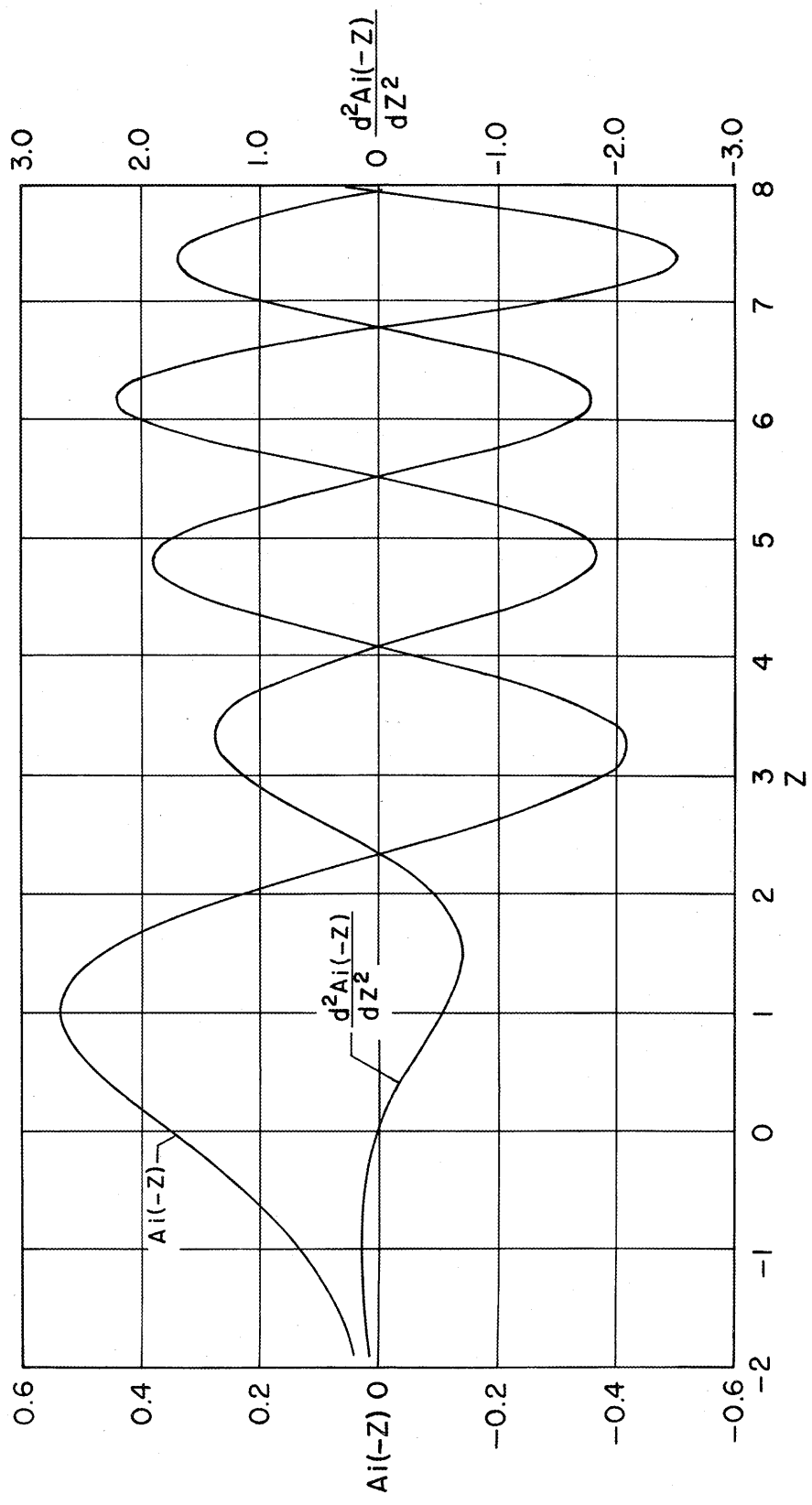

Figure 16. The Airy function Ai(-z) and its second derivative $\frac{d^2Ai(-z)}{dz^2}$.

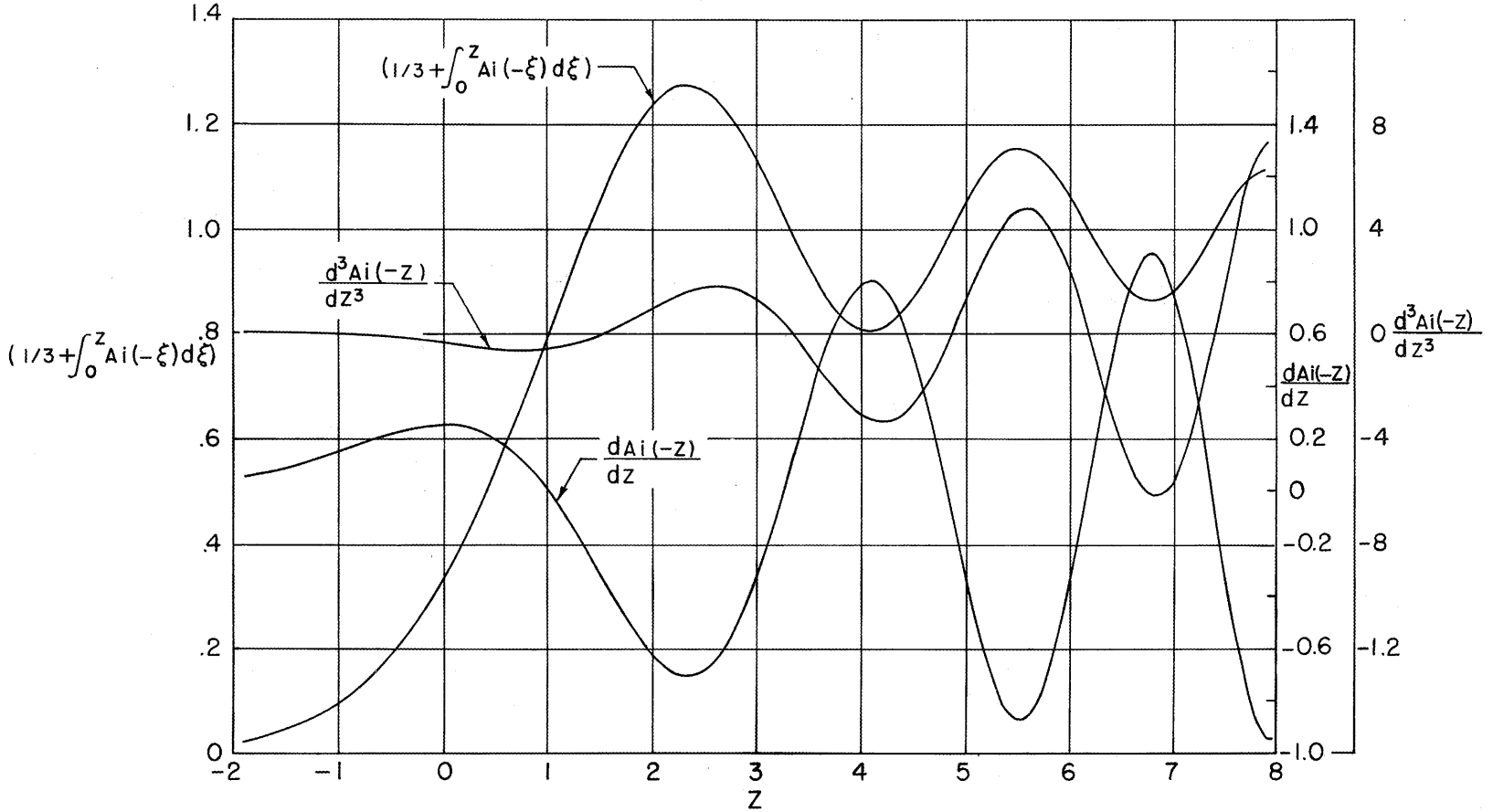

Figure 17. The integral $(\frac{1}{3} + \int_0^z Ai(-\xi)d\xi)$, the first derivative $\frac{dAi(-z)}{dz}$, and the third derivative $\frac{d^3Ai(-z)}{dz^3}$ of the Airy function $Ai(-z)$.

$$\frac{1}{2\pi i}\int_{C_1,C_2} G_1(\beta-\bar{\beta})e^{f_o(\beta)}d\beta = G_1\left[\frac{2}{\alpha'''_{r,s}X}\right]^{2/3} e^{i(\bar{\alpha}_{r,s}X-\bar{\beta}T)}\frac{dAi(-B)}{dB}, \quad (108)$$

$$\frac{1}{2\pi i}\int_{C_1,C_2} G_2(\beta-\bar{\beta})^2 e^{f_o(\beta)}d\beta = iG_2\left[\frac{2}{\alpha'''_{r,s}X}\right] e^{i(\bar{\alpha}_{r,s}X-\bar{\beta}T)}\frac{d^2Ai(-B)}{dB^2}, \quad (109)$$

and

$$\frac{1}{2\pi i}\int_{C_1,C_2} G_3(\beta-\bar{\beta})^3 e^{f_o(\beta)}d\beta = -G_3\left[\frac{2}{\alpha'''_{r,s}X}\right]^{4/3} e^{i(\bar{\alpha}_{r,s}X-\bar{\beta}T)}\frac{d^3Ai(-B)}{dB^3}. \quad (110)$$

2. First mode strain contributions

In equations 90 and 91 for the strains $e_{xx}(X,Y,T)$ and $e_{yy}(X,Y,T)$, respectively, the functions $\theta_{xx}(\alpha_{r,s},Y,\beta)$ and $\theta_{yy}(\alpha_{r,s},Y,\beta)$ are large only for small β. They reflect the behavior of the applied stress at the end of the strip where $\tau^F_{xx} = -iP_o/\omega$. Except for the root $\alpha_{1,1}$, the exponential terms $\exp[i(\alpha_{r,s}X-\beta T)]$ approach zero exponentially as X increases because all the roots of the frequency equation (that are included in the strain expressions) have a positive imaginary component for small β except the root $\alpha_{1,1}$. The root $\alpha_{1,1}$ is the only real root for small β, and therefore, the only root for which θ_{xx}, θ_{yy}, and the exponential part of the integrands are large in the same range of β. Thus, in equations 90 and 91, the first term of each series $(r = 1, s = 1)$ is expected to be large and all other terms to be small in comparison.

From physical arguments it is clear that these comments cannot be applied to the strain $e_{xy}(X,Y,T)$. The function $\theta_{xy}(\alpha_{r,s},Y,\beta)$ in equation 92 is small for small β. There will be an interval of time

at the head of the pulse during which the first term will be dominant. However, as time progresses and the higher modes become operative, it is expected that higher mode terms will be relatively important.

The saddlepoint methods of the previous section will be used to approximately evaluate the first terms,

$$(I_{x,x})_{1,1} = -\frac{P_o}{E}\left[\frac{1}{2\pi i}\int_{-\infty+i\varepsilon}^{\infty+i\varepsilon}\theta_{xx}(\alpha_{1,1},Y,\beta)e^{i(\alpha_{1,1}X-\beta T)}\,d\beta\right], \qquad (111)$$

$$(I_{y,y})_{1,1} = \frac{\sigma P_o}{E}\left[\frac{1}{2\pi i}\int_{-\infty+i\varepsilon}^{\infty+i\varepsilon}\theta_{yy}(\alpha_{1,1},Y,\beta)e^{i(\alpha_{1,1}X-\beta T)}\,d\beta\right], \qquad (112)$$

$$(I_{x,y})_{1,1} = \frac{P_o}{E}\left[\frac{i}{2\pi i}\int_{-\infty+i\varepsilon}^{\infty+i\varepsilon}\theta_{xy}(\alpha_{1,1},Y,\beta)e^{i(\alpha_{1,1}X-\beta T)}\,d\beta\right]. \qquad (113)$$

The functions θ_{xx}, θ_{yy}, and θ_{xy} for the root $\alpha_{1,1}$ and real positive β were evaluated using an IBM 704 computer for a range of values of σ and Y. The results of these calculations are summarized in figures 18, 19 and 20.

Saddlepoint behavior as a function of time: In order to determine during what time intervals a particular method of saddlepoint integration is valid, it is necessary to examine the behavior of saddlepoints in the complex β-plane as a function of time T. From equation 95 the saddlepoints for the $\alpha_{1,1}$ root are defined by the equation

$$\alpha'_{1,1} = \frac{d\alpha_{1,1}}{d\beta} = \frac{T}{X}. \qquad (114)$$

$\alpha'_{1,1}$ is plotted for real β in figure 3, and equation 68 can be used to find this derivative when β is slightly imaginary. As mentioned

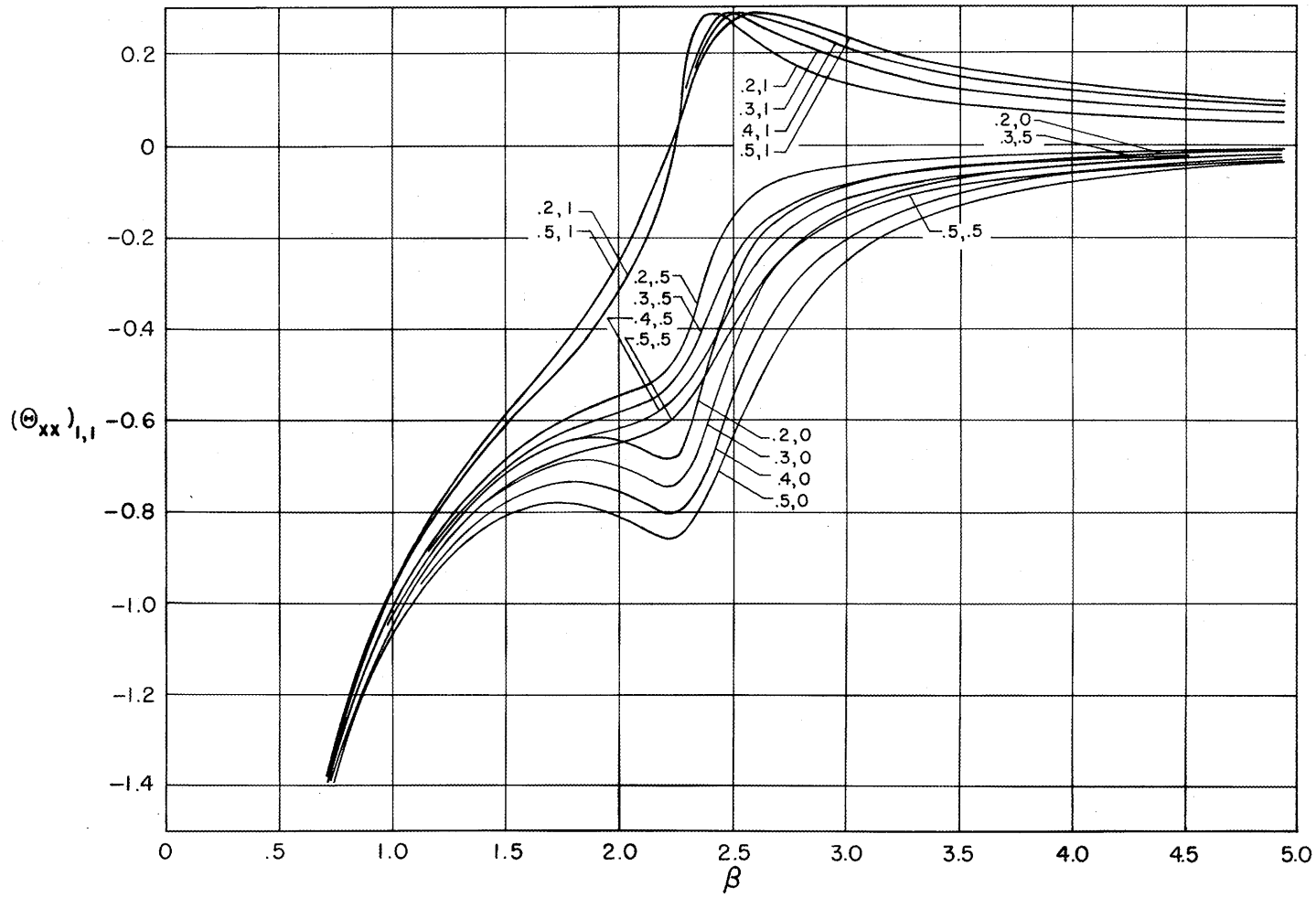

Figure 18. The functions $\Theta_{xx}(\alpha_{1,1},0,\beta)$, $\Theta_{xx}(\alpha_{1,1},0.5,\beta)$, and $\Theta_{xx}(\alpha_{1,1},1.0,\beta)$ for real positive β and σ = 0.2, 0.3, 0.4, and 0.5.

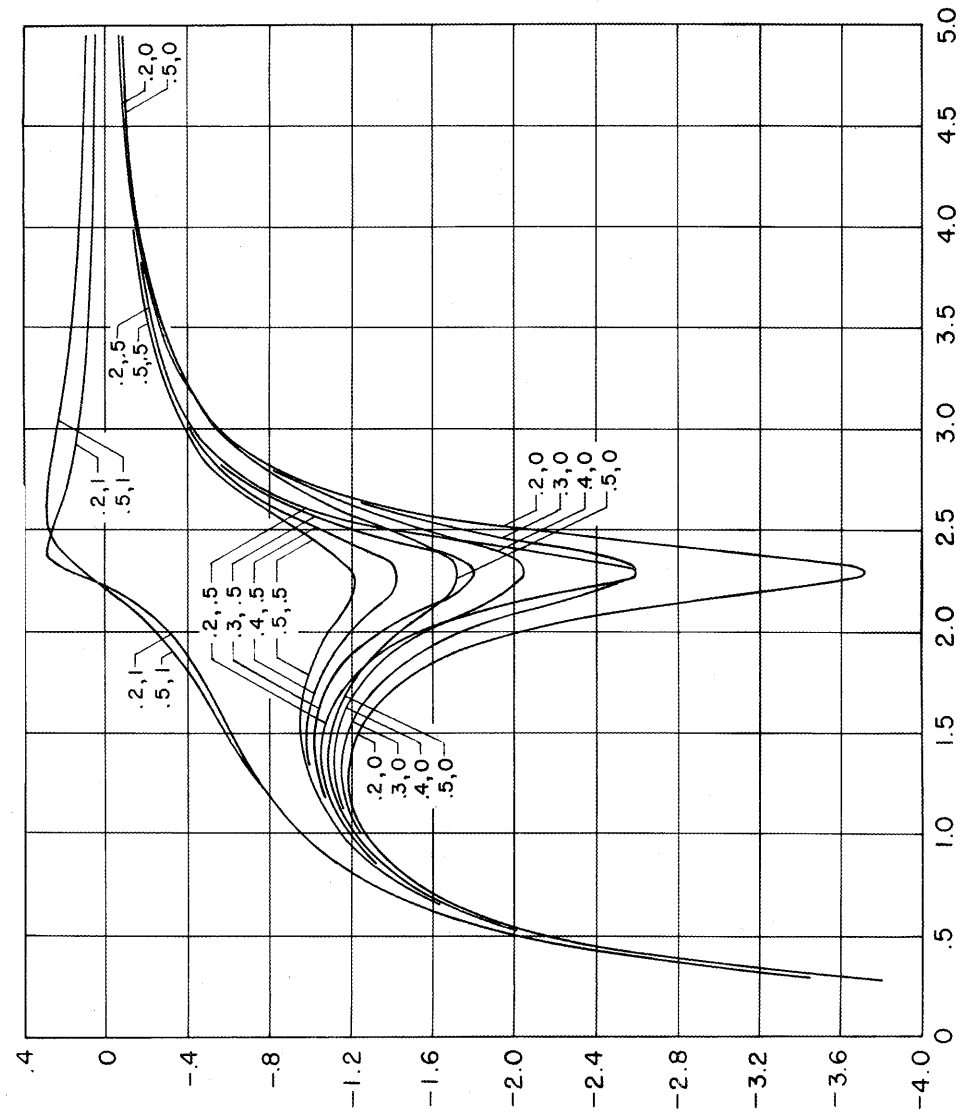

Figure 19. The functions $\theta_{yy}(\alpha_{1,1},0,\beta)$, $\theta_{yy}(\alpha_{1,1},0.5,\beta)$, and $\theta_{yy}(\alpha_{1,1},1.0,\beta)$ for real positive β and $\sigma = 0.2$, 0.3, 0.4, and 0.5.

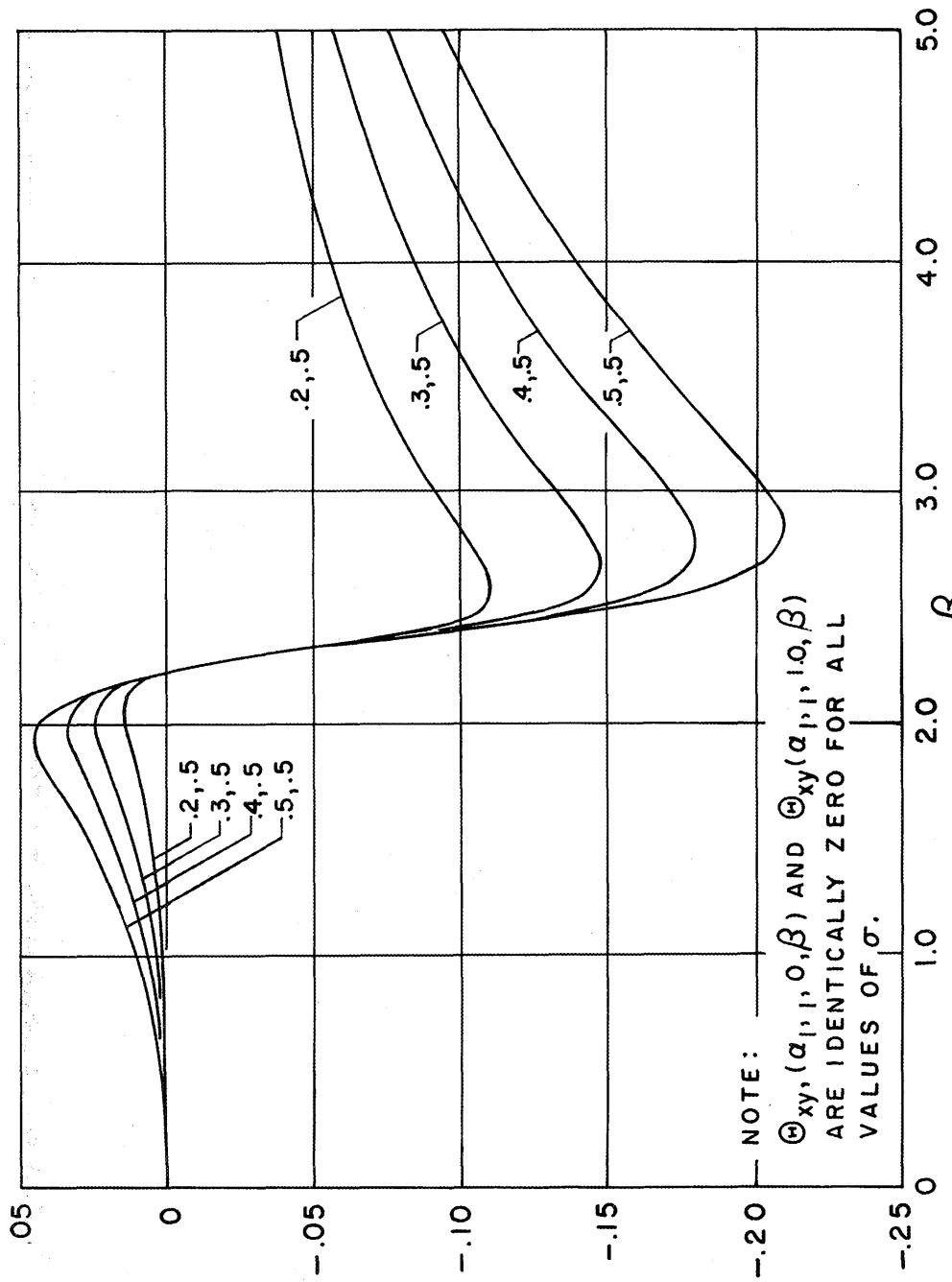

Figure 20. The functions $\theta_{xy}(\alpha_{1,1},0,\beta)$, $\theta_{xy}(\alpha_{1,1},0.5,\beta)$, and $\theta_{xy}(\alpha_{1,1},1.0,\beta)$ for real positive β and $\sigma = 0.2$, 0.3, 0.4, and 0.5.

previously, a complete description of $a_{1,1}$ for complex β is not available.

Based on the findings of Folk (67), second order saddlepoints in the complex region of the β-plane for $\frac{T}{X} < \left[\frac{1-2\sigma}{2(1-\sigma)}\right]^{1/2}$ (which corresponds to $\frac{X}{t} = c_d$, the dilatational wave velocity in an infinite medium) move toward the imaginary β axis as $\frac{T}{X}$ increases. For $\frac{T}{X} > \left[\frac{1-2\sigma}{2(1-\sigma)}\right]^{1/2}$, second order saddlepoints move on the imaginary axis. Two of these saddlepoints move toward the origin (as shown in figure 21a) and collide at the origin to form a third order saddlepoint for $\frac{T}{X} = \frac{1}{[2(1+\sigma)]^{1/2}}$ (see figure 21b). As $\frac{T}{X}$ increases this third order saddlepoint separates into two ordinary saddlepoints moving apart on the real β axis (see figure 21c). At $\frac{T}{X} = \frac{1}{m_1}$, a second pair of saddlepoints appear at $\beta = \pm\infty$ and move along the real β axis toward the origin (see figure 21d). Again, collisions form two third order saddlepoints (see figure 21e) at the value of $\pm\beta$ corresponding to the maximum value of $a'_{1,1} = \frac{T}{X}$ taken from figure 11 for a particular value of σ. After this collision, the ordinary saddlepoints move into the complex β-plane (see figure 21f).

As discussed in the previous section, the o.s.p. method of integration is used when the ordinary saddlepoints are far apart, and the e.s.p. method is used when they are close together. The accuracy of both methods becomes poor in the intermediate ranges. On the diagrams of figure 21, the deformed path of integration is represented by the solid line during the time intervals when the o.s.p. method is valid, and by the dotted line when the e.s.p. method is valid. The shaded areas represent the regions around the paths of steepest descent. The

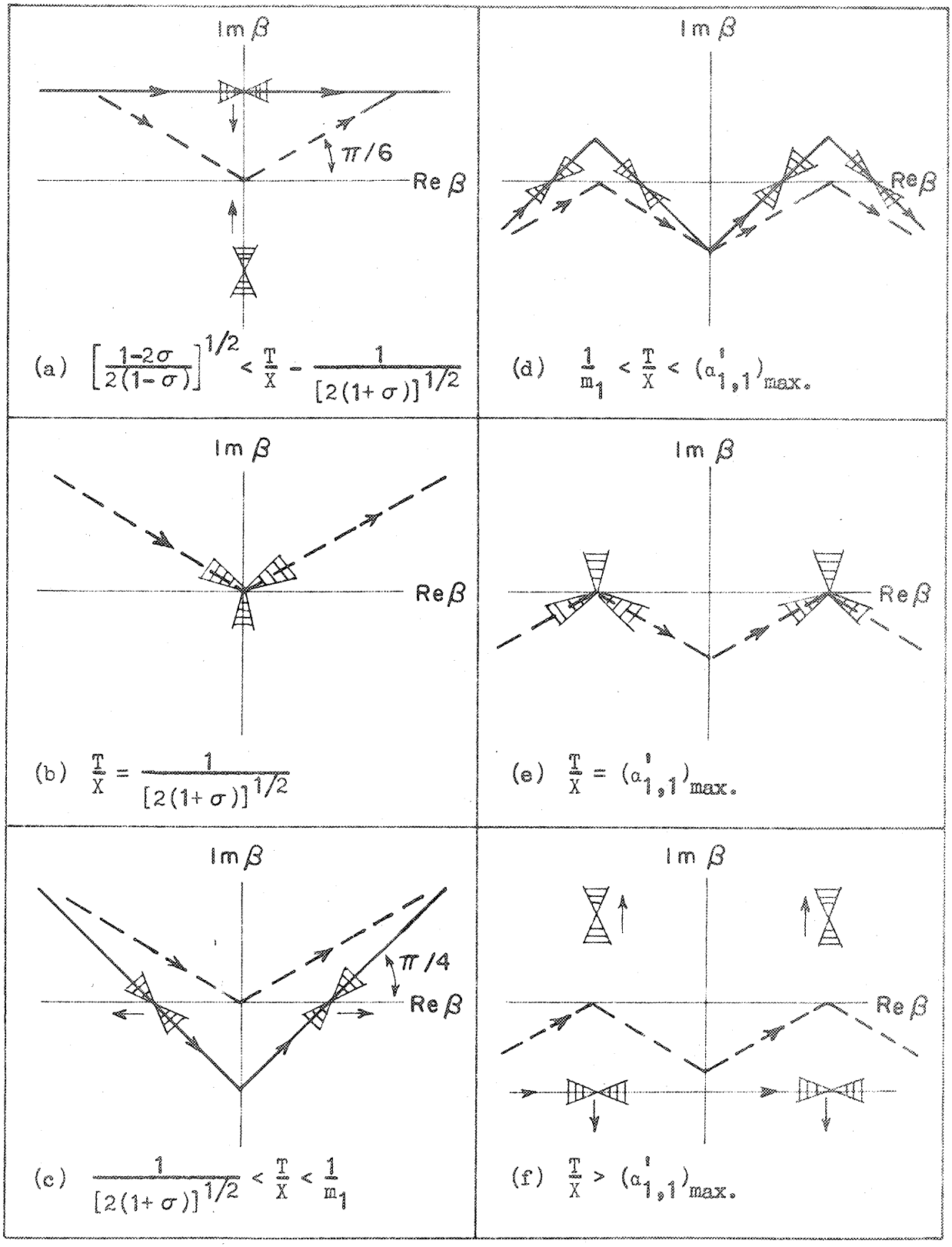

Figure 21. Time-dependent behavior of $\alpha_{1,1}$ saddlepoints.

integrals $(I_{xx})_{1,1}$, $(I_{yy})_{1,1}$, and $(I_{xy})_{1,1}$ will be evaluated quantitatively only when the saddlepoints lie on the real β axis (corresponding to figures 21b, c, d, and e). The following discussion will describe mathematically the features of the pulse observed at a position X as time T progresses. The physical significance of the results will be examined in Part IV.

Head of the pulse: Since detailed calculations of the root $a_{1,1}$ were not made for imaginary β, numerical results cannot be obtained for o.s.p. integrations during the time interval $\left[\frac{1-2\sigma}{2(1-\sigma)}\right]^{1/2} < \frac{T}{X} < \frac{1}{[2(1+\sigma)]^{1/2}}$. However, the expression obtained using the o.s.p. method for a saddlepoint at $\bar{\beta}$ would include the factor

$$e^{iX(\bar{a}_{1,1} - \bar{\beta}\frac{T}{X})} = e^{iX(\bar{a}_{1,1} - \bar{\beta}\,\bar{a}'_{1,1})} . \qquad (115)$$

From equation 68, it can be shown that $iX(\bar{a}_{1,1} - \bar{\beta}\,\bar{a}'_{1,1})$ is negative as the saddlepoint approaches the origin, and is zero at the origin; therefore, for large X the initial signal is very small and probably has a time dependence of the form $e^{-\zeta}$, where ζ becomes smaller as $\frac{T}{X}$ approaches $\frac{1}{[2(1+\sigma)]^{1/2}}$.

The shape of the first large signal to arrive can be quantitatively calculated. As the saddlepoints move closer together, the e.s.p. method is used and the path of integration is taken as the dotted path in figures 21a, b, and c. It is hoped that this method will be valid during an interval of time including the collision time $\frac{T}{X} = \frac{1}{[2(1+\sigma)]^{1/2}}$.

To use this method, the Laurent series expansions of $\theta_{xx}(a_{1,1}, Y, \beta)$, $\theta_{yy}(a_{1,1}, Y, \beta)$, and $\theta_{xy}(a_{1,1}, Y, \beta)$ about $\beta = 0$ are required. For

low values of frequency, the relationship between $\alpha_{1,1}$ and β is given by the Taylor series of equation 68. By substituting equation 68 into the expressions for θ_{xx}, θ_{yy}, and θ_{xy} given by equations 93, 77, 79, and 81, the first few terms of the respective Laurent series are found, after very extensive algebraic manipulations (which will not be shown here), to be:

$$\theta_{xx}(\alpha_{1,1},Y,\beta) = -\frac{1}{\beta} - \frac{1}{(1+\sigma)}\left[\frac{\sigma}{4}(1-Y^2) - \frac{\sigma(1-\sigma)}{6}\right]\beta$$

$$-\left[\eta_x(\sigma) - \upsilon_x(\sigma)(1-Y^2) - \chi_x(\sigma)Y^2(1-\Psi_x(\sigma)Y^2)\right]\beta^3$$

$$+ \cdots , \qquad (116)$$

$$\theta_{yy}(\alpha_{1,1},Y,\beta) = -\frac{1}{\beta} - \frac{1}{(1+\sigma)}\left[\frac{(1+\sigma-\sigma^2)}{4}(1-Y^2) - \frac{\sigma(1-\sigma)}{6}\right]\beta$$

$$-\left[\eta_y(\sigma) - \upsilon_y(\sigma)(1-Y^2) - \chi_y(\sigma)Y^2(1-\Psi_y(\sigma)Y^2)\right]\beta^3$$

$$+ \cdots , \qquad (117)$$

$$\theta_{xy}(\alpha_{1,1},Y,\beta) = \frac{\sigma^2 Y(1-Y^2)\beta^2}{6(2+2\sigma)^{1/2}} + \cdots , \qquad (118)$$

where σ is Poisson's ratio. The values of $\eta_x(\sigma)$, $\upsilon_x(\sigma)$, $\chi_x(\sigma)$, and $\Psi_x(\sigma)$ are to be taken from figure 22 for a particular value of σ. Similarly, the values of $\eta_y(\sigma)$, $\upsilon_y(\sigma)$, $\chi_y(\sigma)$, $\Psi_y(\sigma)$ are to be taken from figure 23. (The expressions for $\eta(\sigma)$, $\upsilon(\sigma)$, $\chi(\sigma)$, and $\Psi(\sigma)$ are so lengthy it is not worthwhile to give explicit expressions for them.) Equation 68 can also be used to

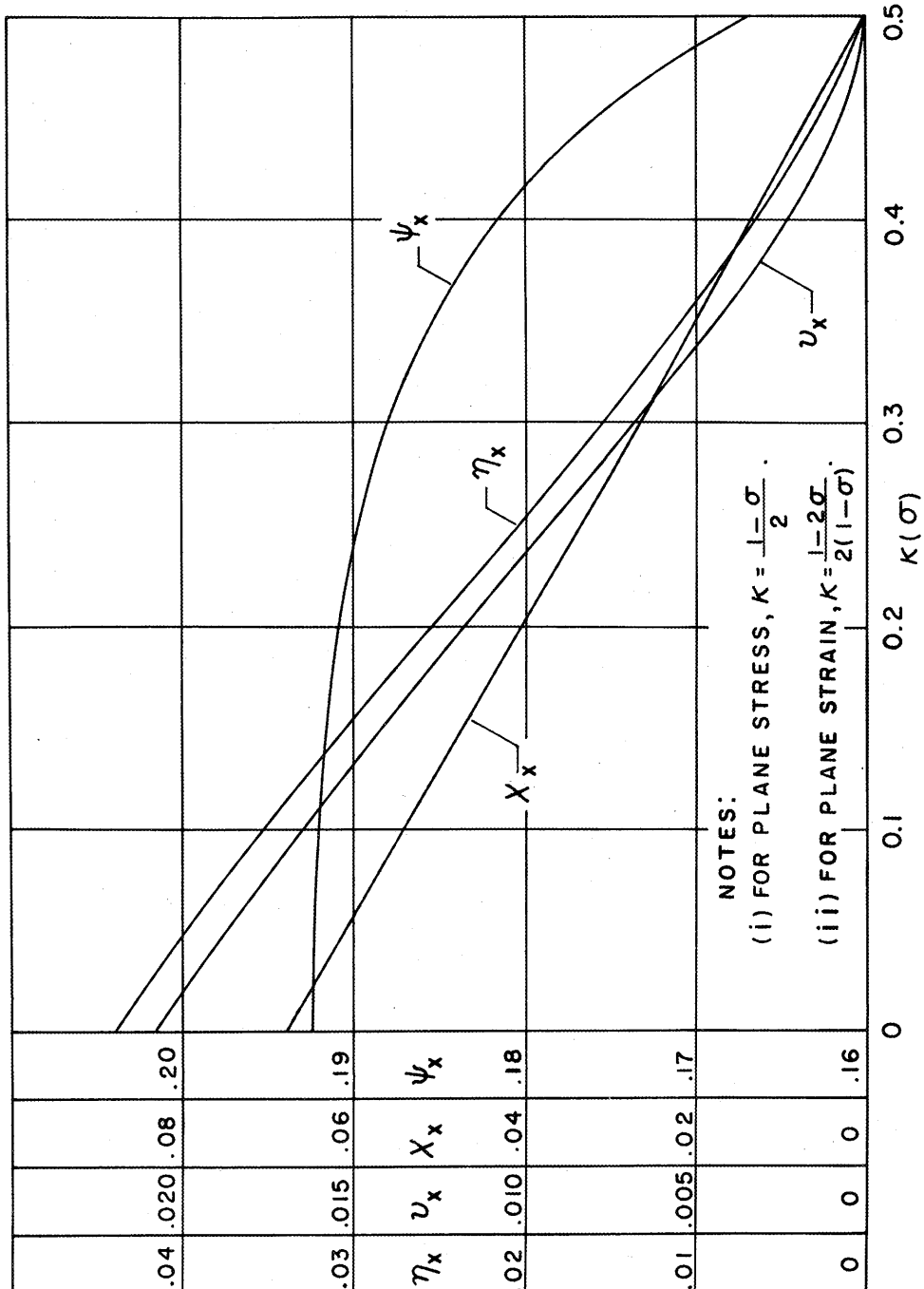

Figure 22. The coefficients η_x, υ_x, χ_x, and ψ_x in equations 116 and 120 as functions of $\kappa(\sigma)$.

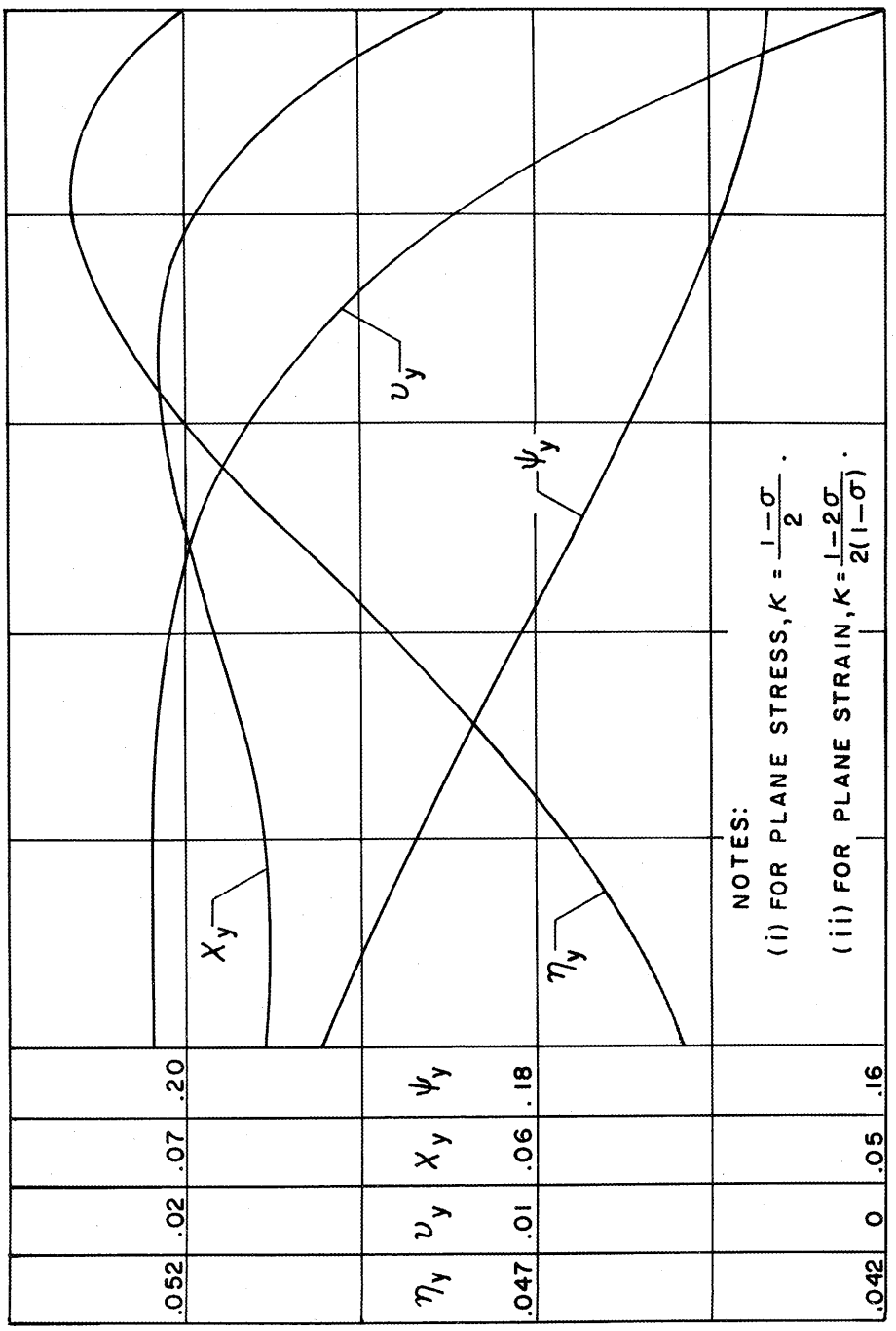

Figure 23. The coefficients η_y, υ_y, χ_y, and ψ_y in equations 117 and 121 as functions of $\kappa(\sigma)$.

evaluate $\bar{a}^{\prime\prime\prime\prime}_{1,1}$ at the origin,

$$\bar{a}^{\prime\prime\prime\prime}_{1,1} = \left.\frac{d^3 a_{1,1}}{d\beta^3}\right|_{\beta = 0} = \frac{\sigma^2}{(2+2\sigma)^{3/2}} . \tag{119}$$

The first few terms of $(I_{xx})_{1,1}$, $(I_{yy})_{1,1}$, and $(I_{xy})_{1,1}$ can now be evaluated by the e.s.p. method using equations 106, 108, 109, and 110:

$$(I_{xx})_{1,1} \cong -\frac{P_o}{E}\left\{\left[\frac{1}{3} + \int_0^B Ai(-\xi)d\xi\right] - \left[\frac{\sigma}{2}(1-Y^2) - \frac{\sigma(1-\sigma)}{3}\right]\left[\frac{2}{\sigma^2 X}\right]^{2/3}\frac{dAi(-B)}{dB} + 4(1+\sigma)^2\left[\eta_x(\sigma) - \upsilon_x(\sigma)(1-Y^2) - \chi_x(\sigma)Y^2(1-\Psi_x(\sigma)Y^2)\right]\left[\frac{2}{\sigma^2 X}\right]^{4/3}\frac{d^3Ai(-B)}{dB^3}\right\}, \tag{120}$$

$$(I_{yy})_{1,1} \cong \frac{\sigma P_o}{E}\left\{\left[\frac{1}{3} + \int_0^B Ai(-\xi)d\xi\right] - \left[\frac{(1+\sigma-\sigma^2)}{2}(1-Y^2) - \frac{\sigma(1-\sigma)}{3}\right]\left[\frac{2}{\sigma^2 X}\right]^{2/3}\frac{dAi(-B)}{dB} + 4(1+\sigma)^2\left[\eta_y(\sigma) - \upsilon_y(\sigma)(1-Y^2) - \chi_y(\sigma)Y^2(1-\Psi_y(\sigma)Y^2)\right]\cdot\left[\frac{2}{\sigma^2 X}\right]^{4/3}\frac{d^3Ai(-B)}{dB^3}\right\}, \tag{121}$$

$$(I_{xy})_{1,1} \cong -\frac{P_o}{E}\,\frac{2}{3}\,\frac{(1+\sigma)}{X}\,Y(1-Y^2)\,\frac{d^2Ai(-B)}{dB^2}, \tag{122}$$

where $B = (2+2\sigma)^{1/2}\left[\frac{2}{\sigma^2 X}\right]^{1/3}\left(T - \frac{X}{(2+2\sigma)^{1/2}}\right)$. (123)

The number of terms retained in the above expressions is dictated by the following considerations: (i) Since the purpose of this analysis is to gain some insight into the strain distribution across the width of the strip, the expressions should include the first term in which Y

appears. (ii) The final term of an expression should have a small value relative to that of the initial term. (iii) It is not feasible to retain β^n terms for $n > 3$ because of the prodigious amount of algebra required to determine the coefficients. In particular, more terms are not retained in equation 122 because of (iii).

It should be noted in passing that the only terms in the expressions for $(I_{xx})_{1,1}$, $(I_{yy})_{1,1}$ and $(I_{xy})_{1,1}$ which do not decrease as X increases are the initial terms in $(I_{xx})_{1,1}$ and $(I_{yy})_{1,1}$. In the limit as X becomes very large $(I_{yy})_{1,1} = -\sigma (I_{xx})_{1,1}$, independent of Y, and $(I_{xy})_{1,1}$ vanishes. This result is expected on physical grounds.

Oscillations following the head of the pulse: When the saddle-points have become sufficiently separated, $(I_{xx})_{1,1}$, $(I_{yy})_{1,1}$, and $(I_{xy})_{1,1}$ can be approximately evaluated using the o.s.p. method. The path of integration is deformed into the paths of steepest descent corresponding to the solid path in figure 21c. By applying equation 98, the contribution in the neighborhoods of the two saddlepoints at $\pm \bar{\beta}$ can be estimated. If the contour is deformed across any poles of the integrand, the contributions of these poles are $2\pi i$ times their residues.

The evaluation of $(I_{xx})_{1,1}$ will be carried out in detail to illustrate the procedure. From equation 116, it is clear that $\theta_{xx}(\alpha_{1,1}, Y, \beta)$ has a simple pole at the origin. The corresponding residue of the integrand of equation 111 is -1. The value of $(I_{xx})_{1,1}$ is the sum of the contributions of the two saddlepoints minus $2\pi i$ times the residue of the pole at the origin. Thus,

$$(I_{xx})_{1,1} \cong -\frac{P_o}{E}\left[\frac{\theta_{xx}(\bar{\alpha}_{1,1},Y,\bar{\beta})e^{i(\bar{\alpha}_{1,1}X-\bar{\beta}T+\frac{\pi}{4})}}{i\sqrt{2\pi X|\bar{\alpha}''_{1,1}|}} + \frac{\theta_{xx}(-\bar{\alpha}_{1,1},Y,-\bar{\beta})e^{i(-\bar{\alpha}_{1,1}X+\bar{\beta}T-\frac{\pi}{4})}}{i\sqrt{2\pi X|\bar{\alpha}''_{1,1}|}} - \frac{2\pi i(-1)}{2\pi i}\right],$$

$$= -\frac{P_o}{E}\left[1+\frac{1}{i}\frac{\theta_{xx}(\bar{\alpha}_{1,1},Y,\bar{\beta})}{\sqrt{2\pi X|\bar{\alpha}''_{1,1}|}}\, e^{i(\bar{\alpha}_{1,1}X-\bar{\beta}T+\frac{\pi}{4}} - e^{-i(\bar{\alpha}_{1,1}X-\bar{\beta}T+\frac{\pi}{4})}\right],$$

$$= -\frac{P_o}{E}\left[1+\frac{2\theta_{xx}(\bar{\alpha}_{1,1},Y,\bar{\beta})}{\sqrt{2\pi X|\bar{\alpha}''_{1,1}|}}\sin(\bar{\alpha}_{1,1}X-\bar{\beta}T+\frac{\pi}{4})\right], \qquad (124)$$

since $\theta_{xx}(-\bar{\alpha}_{1,1},Y,-\bar{\beta}) = -\theta_{xx}(\bar{\alpha}_{1,1},Y,\bar{\beta})$ and $\left.\frac{d^2\alpha_{1,1}}{d\beta^2}\right|_{\beta=\bar{\beta}} = -\left.\frac{d^2\alpha_{1,1}}{d\beta^2}\right|_{\beta=-\bar{\beta}}$. Since the same comments apply to $(I_{yy})_{1,1}$, its evaluation is

$$(I_{yy})_{1,1} \cong \frac{\sigma P_o}{E}\left[1+\frac{2\theta_{yy}(\bar{\alpha}_{1,1},Y,\bar{\beta})}{\sqrt{2\pi X|\bar{\alpha}''_{1,1}|}}\sin(\bar{\alpha}_{1,1}X-\bar{\beta}T+\frac{\pi}{4})\right]. \qquad (125)$$

The evaluation of $(I_{xy})_{1,1}$ gives

$$(I_{xy})_{1,1} \cong \frac{2P_o}{E}\,\frac{\theta_{xy}(\bar{\alpha}_{1,1},Y,\bar{\beta})}{\sqrt{2\pi X|\bar{\alpha}''_{1,1}|}}\cos(\bar{\alpha}_{1,1}X-\bar{\beta}T+\frac{\pi}{4}), \qquad (126)$$

since there are no poles and $\theta_{xy}(-\bar{\alpha}_{1,1},Y,-\bar{\beta}) = \theta_{xy}(\bar{\alpha}_{1,1},Y,\bar{\beta})$.

These expressions predict that at a time $T = X\bar{\alpha}'_{1,1}$ there will be

oscillations having an instantaneous period $(2\pi a)/(c_s \bar{\bar{\beta}})$, a wavelength $2\pi a/\bar{\alpha}_{1,1}$, and an amplitude that decreases with increasing X as $X^{-1/2}$. The amplitudes of the oscillations are easily computed for given values of σ and Y by using the values of $\theta_{xx}(\bar{\alpha}_{1,1}, Y, \bar{\bar{\beta}})$, $\theta_{yy}(\bar{\alpha}_{1,1}, Y, \bar{\bar{\beta}})$, and $\theta_{xy}(\bar{\alpha}_{1,1}, Y, \bar{\bar{\beta}})$ obtained from figures 18, 19, and 20; and the value of $\bar{\alpha}''_{1,1}$ obtained from figure 11. In the expressions for $(I_{xx})_{1,1}$ and $(I_{yy})_{1,1}$ the oscillations are superimposed on the static strain values.

At a time essentially corresponding to the arrival of the Rayleigh surface waves, $\frac{T}{X} = \frac{1}{m_1}$, two saddlepoints appear at $\pm\infty$ and move toward the origin. The path of integration is now taken as the solid path in figure 21d. This adds the contributions of the two new saddlepoints to the expressions for $(I_{xx})_{1,1}$, $(I_{yy})_{1,1}$ and $(I_{xy})_{1,1}$ given by equations 124, 125, and 126. The net contribution to $(I_{xx})_{1,1}$, $(I_{yy})_{1,1}$ and $(I_{xy})_{1,1}$ is, in each case, the addition of an oscillatory term identical to the existing one except that the value of $\bar{\bar{\beta}}$ in this term is that of the new saddlepoint on the positive β axis and the phase factor is $-\frac{\pi}{4}$ instead of $\frac{\pi}{4}$.

During the time interval when there are two pairs of saddlepoints, each of the strain expressions contains two oscillatory terms of different and changing frequencies. In order to obtain the sum of these two terms it would be necessary to carry out accurate calculations of $(\bar{\alpha}X - \bar{\bar{\beta}}T)$ for small increments of time.

End of the first mode oscillations: As the two pairs of saddlepoints approach each other and finally collide, the o.s.p. method breaks down and the e.s.p. method must be used. The path of integration is taken as the dotted path in figures 21d, e, and f. The functions $(\theta_{xx})_{1,1}$,

$(\theta_{yy})_{1,1}$, $(\theta_{xy})_{1,1}$ are analytic in the neighborhood of $\bar{\beta}$ corresponding to $T/X = (\alpha'_{1,1})_{max.}$; hence, the first non-zero term in the respective Laurent series of these functions about $\bar{\beta}$ is the value of the function itself for $\beta = \bar{\beta}$. For this approximation, only these first terms will be used. Using equation 107 instead of equation 98, the contributions from the saddlepoints at $\beta = \pm\bar{\beta}$ are combined as in the preceding approximation:

$$(I_{xx})_{1,1} \cong -\frac{P_o}{E}\left\{1 + 2\theta_{xx}(\bar{\alpha}_{1,1}, Y, \bar{\beta})\left(\frac{2}{X|\bar{\alpha}'''_{1,1}|}\right)^{1/3} \cdot \mathrm{Ai}\left[(T-\bar{\alpha}'_{1,1}X)\left(\frac{2}{X|\bar{\alpha}'''_{1,1}|}\right)^{1/3}\right]\sin(\bar{\alpha}_{1,1}X - \bar{\beta}T)\right\}, \qquad (127)$$

$$(I_{yy})_{1,1} \cong \frac{\sigma P_o}{E}\left\{1 + 2\theta_{yy}(\bar{\alpha}_{1,1}, Y, \bar{\beta})\left(\frac{2}{X|\bar{\alpha}'''_{1,1}|}\right)^{1/3} \cdot \mathrm{Ai}\left[(T-\bar{\alpha}'_{1,1}X)\left(\frac{2}{X|\bar{\alpha}'''_{1,1}|}\right)^{1/3}\right]\sin(\bar{\alpha}_{1,1}X - \bar{\beta}T)\right\}, \qquad (128)$$

$$(I_{xy})_{1,1} \cong \frac{2P_o}{E}\theta_{xy}(\bar{\alpha}_{1,1}, Y, \bar{\beta})\left(\frac{2}{X|\bar{\alpha}'''_{1,1}|}\right)^{1/3} \cdot \mathrm{Ai}\left[(T-\bar{\alpha}'_{1,1}X)\left(\frac{2}{X|\bar{\alpha}'''_{1,1}|}\right)^{1/3}\right]\cos(\bar{\alpha}_{1,1}X - \bar{\beta}T). \qquad (129)$$

As time progresses the saddlepoints separate and move into the complex plane as shown in figure 21f. The oscillatory terms will be multiplied by an exponential factor having a negative exponent which increases as time increases.

3. Higher mode strain contributions

As mentioned above, the higher mode terms ($r > 1$, $s > 1$) in the respective series for e_{xx} and e_{yy} will be relatively much smaller than the initial terms because they are integrals of the product of two functions which are not simultaneously large for the same values of β. However, the first term for e_{xy} is small and the higher mode terms can be expected to be relatively more important in this case.

As β increases the roots $\alpha_{1,2}$ and $\alpha_{2,2}$ are the first roots to become real; hence the corresponding terms in the expressions for e_{xx}, e_{yy}, and e_{xy} are expected to be next in importance to the initial terms. The remaining higher modes are expected to contribute oscillations which are smaller than those of the second mode and occur at a later time.

The integrals $(I_{xx})_{2,1}$ and $(I_{xx})_{2,2}$ are complex conjugates which combine to give a real contribution to the strain signal; this is also true of $(I_{yy})_{2,1} + (I_{yy})_{2,2}$ and $(I_{xy})_{2,1} + (I_{xy})_{2,2}$.* The second mode contributions will be approximately evaluated for a short time interval which includes the first and largest signals arising from the $\alpha_{2,1}$ and $\alpha_{2,2}$ roots. The saddlepoints for $\alpha_{2,1}$ and $\alpha_{2,2}$ are at complex values of β for $T/X < (\alpha'_{2,1})_{min.} = (\alpha'_{2,2})_{min.}$, and so signals approach zero exponentially for large X until an interval just prior to this time. Figure 24 illustrates the time-dependent behavior of the

---

* These sums, for all time, correspond to the contributions from what is classically called the second and third modes.

first real saddlepoints for $\alpha_{2,1}$ and $\alpha_{2,2}$.* There are other real saddlepoints that become real at a later time and for larger values of $|\beta|$; consequently, these saddlepoints contribute smaller oscillations at a later time.

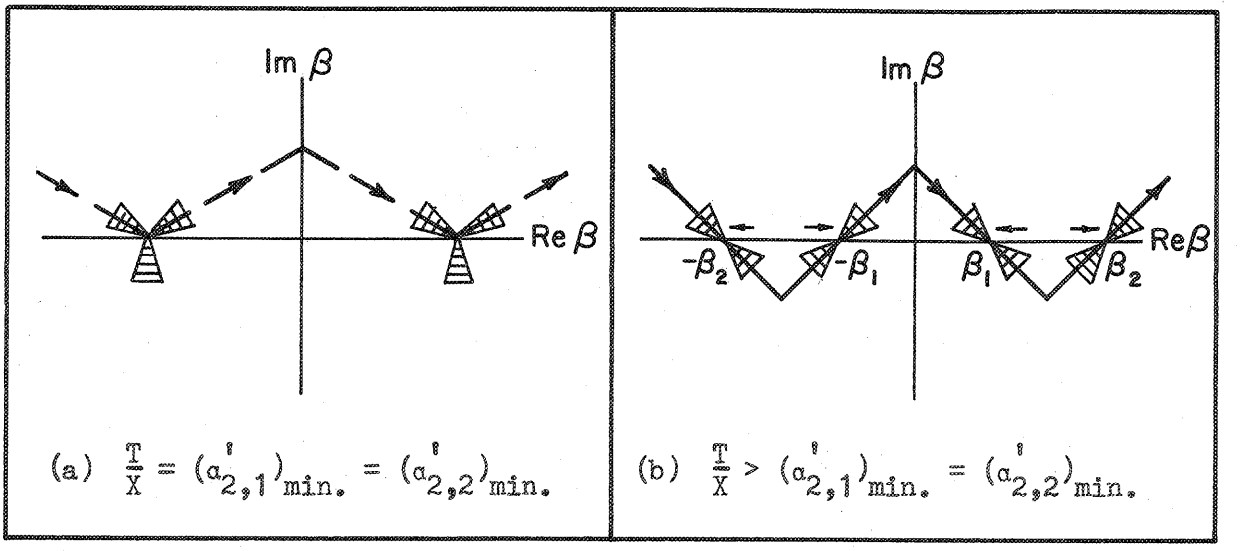

Figure 24. Time-dependent behavior of initial $\alpha_{2,1}$ and $\alpha_{2,2}$ saddlepoints.

When the saddlepoints are close together the e.s.p. method is used with the path of integration shown in figure 24a. For this case $\bar{\alpha}'''_{2,1}$ and $\bar{\alpha}'''_{2,2}$ are equal and positive. The strain expressions are evaluated in the same manner as they were for the last of the first mode oscillations except that the integrands have no poles:

---

* The strains from these initial saddlepoints correspond to contributions from what is classically called the second mode.

$$(I_{xx})_{2,1} + (I_{xx})_{2,2} = -\frac{2P_o}{E}\ \theta_{xx}(\bar{a}_{2,1}, Y, \bar{\beta})\left(\frac{2}{X|\bar{a}'''_{2,1}|}\right)^{1/3}$$

$$\cdot\ \mathrm{Ai}\left[(\bar{a}'_{2,1}X - T)\left(\frac{2}{X|\bar{a}'''_{2,1}|}\right)^{1/3}\right]\sin(\bar{a}_{2,1}X - \bar{\beta}T), \quad (130)$$

$$(I_{yy})_{2,1} + (I_{yy})_{2,2} = \frac{2\sigma P_o}{E}\ \theta_{yy}(\bar{a}_{2,1}, Y, \bar{\beta})\left(\frac{2}{X|\bar{a}'''_{2,1}|}\right)^{1/3}$$

$$\cdot\ \mathrm{Ai}\left[(\bar{a}'_{2,1}X - T)\left(\frac{2}{X|\bar{a}'''_{2,1}|}\right)^{1/3}\right]\sin(\bar{a}_{2,1}X - \bar{\beta}T), \quad (131)$$

and

$$(I_{xy})_{2,1} + (I_{xy})_{2,2} = \frac{2P_o}{E}\ \theta_{xy}(\bar{a}_{2,1}, Y, \bar{\beta})\left(\frac{2}{X|\bar{a}'''_{2,1}|}\right)^{1/3}$$

$$\cdot\ \mathrm{Ai}\left[(\bar{a}'_{2,1}X - T)\left(\frac{2}{X|\bar{a}'''_{2,1}|}\right)^{1/3}\right]\cos(\bar{a}_{2,1}X - \bar{\beta}T). \quad (132)$$

During the time interval when there are four sufficiently separated ordinary saddlepoints, the expressions become

$$(I_{xx})_{2,1} + (I_{xx})_{2,2} = -\frac{2P_o}{E}\sum_{i=1}^{2}\frac{\theta_{xx}(\bar{a}_{2,1}, Y, \bar{\beta}_i)}{\sqrt{2\pi X|\bar{a}'''_{2,1}|}}$$

$$\cdot\ \sin(\bar{a}_{2,1}X - \bar{\beta}_i T \pm \tfrac{\pi}{4}), \quad (133)$$

$$(I_{yy})_{2,1} + (I_{yy})_{2,2} = \frac{2\sigma P_o}{E} \sum_{i=1}^{2} \frac{\theta_{yy}(\bar{\alpha}_{2,1}, Y, \bar{\beta}_i)}{\sqrt{2\pi X |\bar{\alpha}''_{2,1}|}}$$

$$\cdot \sin(\bar{\alpha}_{2,1} X - \bar{\beta}_i T \pm \tfrac{\pi}{4}) , \qquad (134)$$

and

$$(I_{xy})_{2,1} + (I_{xy})_{2,2} = \frac{2P_o}{E} \sum_{i=1}^{2} \frac{\theta_{xy}(\bar{\alpha}_{2,1}, Y, \bar{\beta}_i)}{\sqrt{2\pi X |\bar{\alpha}''_{2,1}|}}$$

$$\cdot \cos(\bar{\alpha}_{2,1} X - \bar{\beta}_i T \pm \tfrac{\pi}{4}) , \qquad (135)$$

where $-\frac{\pi}{4}$ is used for the $i = 1$ terms, and $+\frac{\pi}{4}$ is used when $i = 2$. During this time interval, the signal consists of two oscillations of different and changing frequencies which cannot be easily combined. Values for $\theta_{xx}(\bar{\alpha}_{2,1}, Y, \bar{\beta})$, $\theta_{yy}(\bar{\alpha}_{2,1}, Y, \bar{\beta})$, and $\theta_{xy}(\bar{\alpha}_{2,1}, Y, \bar{\beta})$ are given for several values of σ and Y in figures 25, 26, and 27.

The total strains e_{xx}, e_{yy}, e_{xy} include the contributions from all modes. From the sketch given by Mindlin (86), it can be seen that the minimum value of $d\alpha/d\beta$ is larger for the next few roots above $\alpha_{1,1}$ and $\alpha_{2,1}$ and it occurs for larger values of $|\beta|$. Thus, these higher modes will contribute smaller oscillations at later times. However, Folk (67) points out that some of the roots $\alpha_{r,s}$ for r large can have minimum values of $d\alpha/d\beta$ corresponding to signals travelling at dilatation velocity. Mindlin's sketch corroborates this observation. These minimums occur, however, for very large values of $|\beta|$ and result in oscillations of negligible amplitude for the present problem.

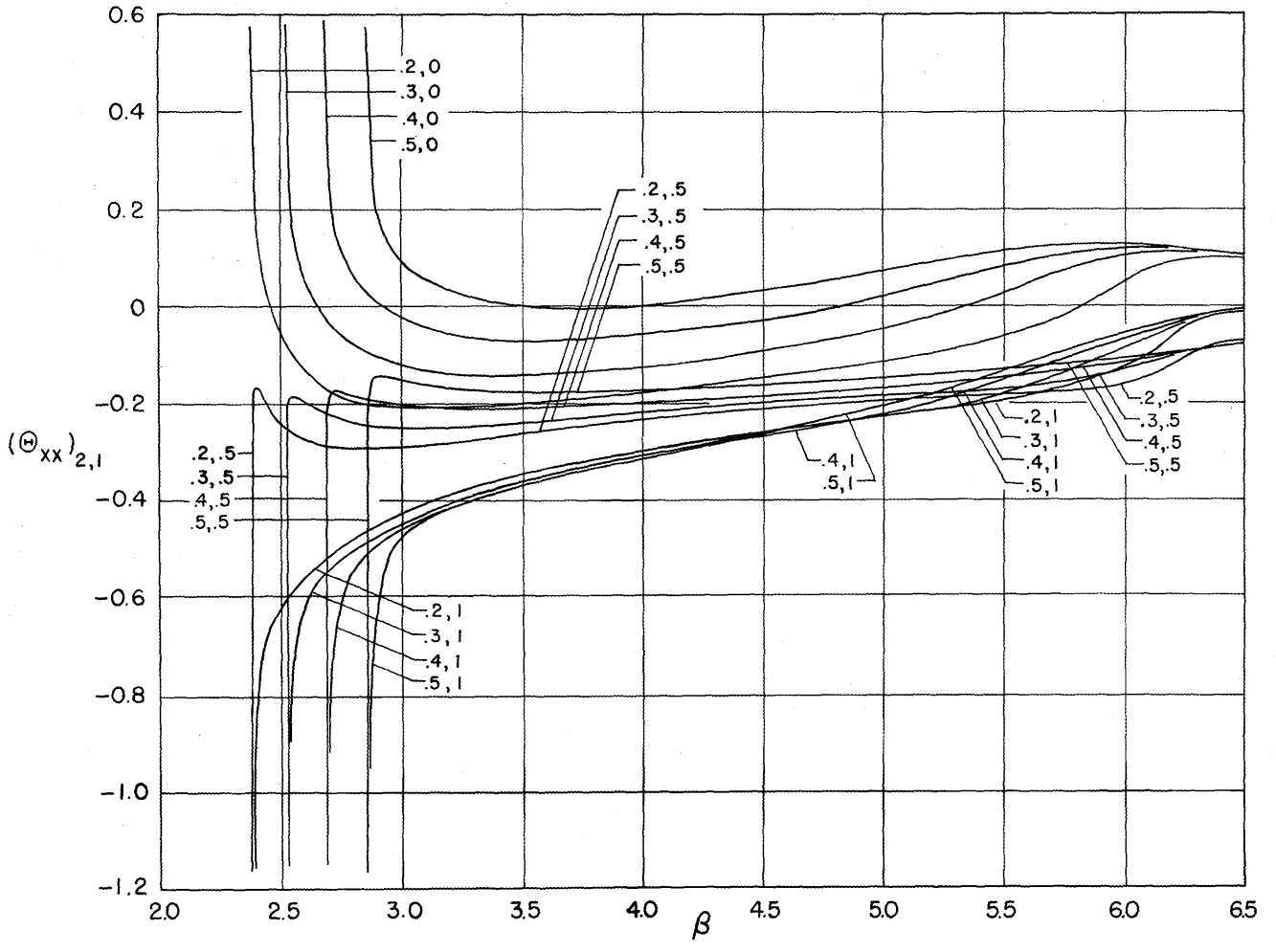

Figure 25. The functions $\theta_{xx}(\alpha_{2,1},0,\beta)$, $\theta_{xx}(\alpha_{2,1},0.5,\beta)$, and $\theta_{xx}(\alpha_{2,1},1.0,\beta)$ in the region of real positive β corresponding to real $\alpha_{2,1}$ for $\sigma = 0.2$, 0.3, 0.4, and 0.5.

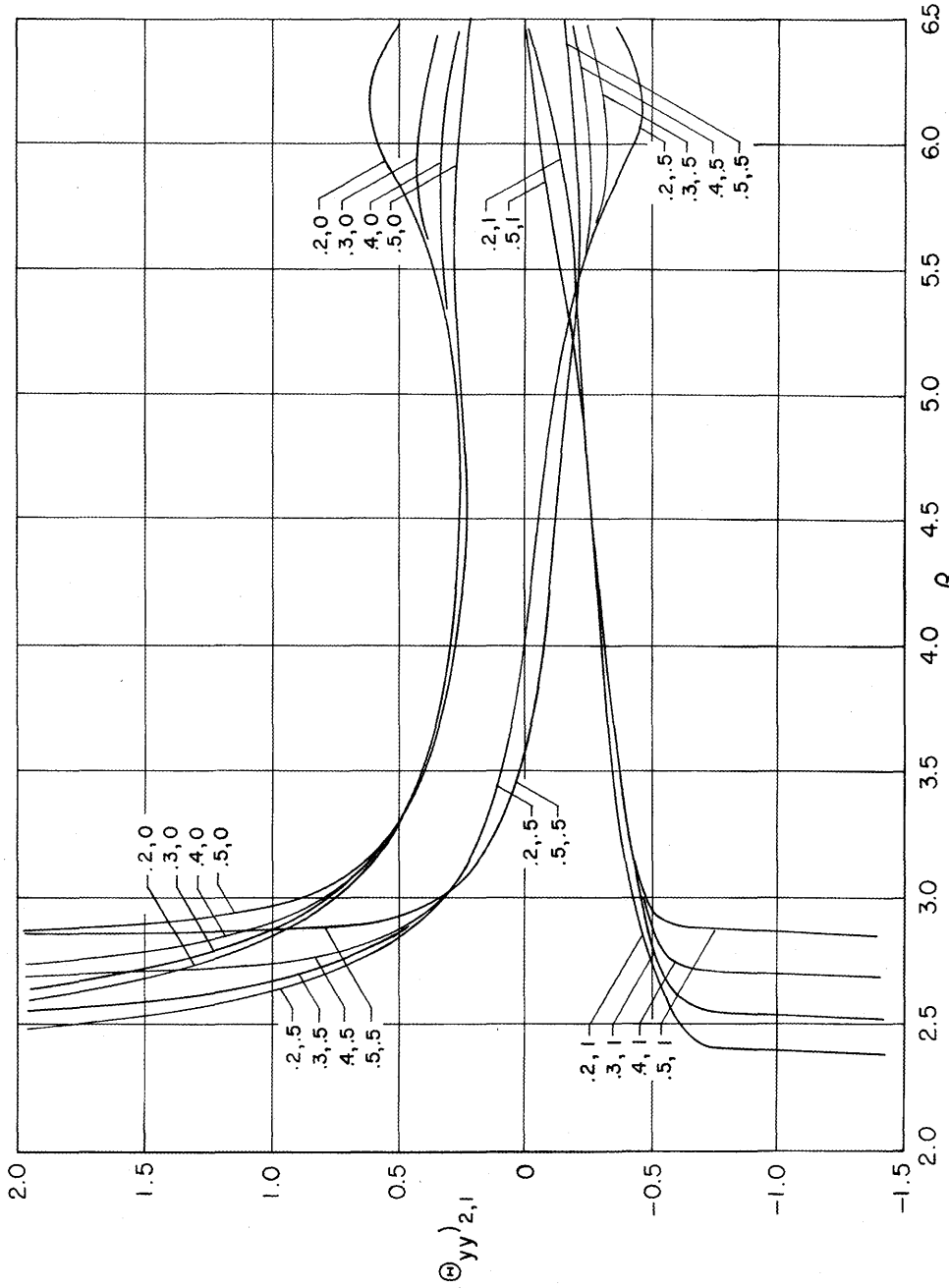

Figure 26. The functions $\theta_{yy}(a_{2,1},0,\beta)$, $\theta_{yy}(a_{2,1},0.5,\beta)$, and $\theta_{yy}(a_{2,1},1.0,\beta)$ in the region of real positive β corresponding to real $a_{2,1}$ for $\sigma = 0.2$, 0.3, 0.4, and 0.5.

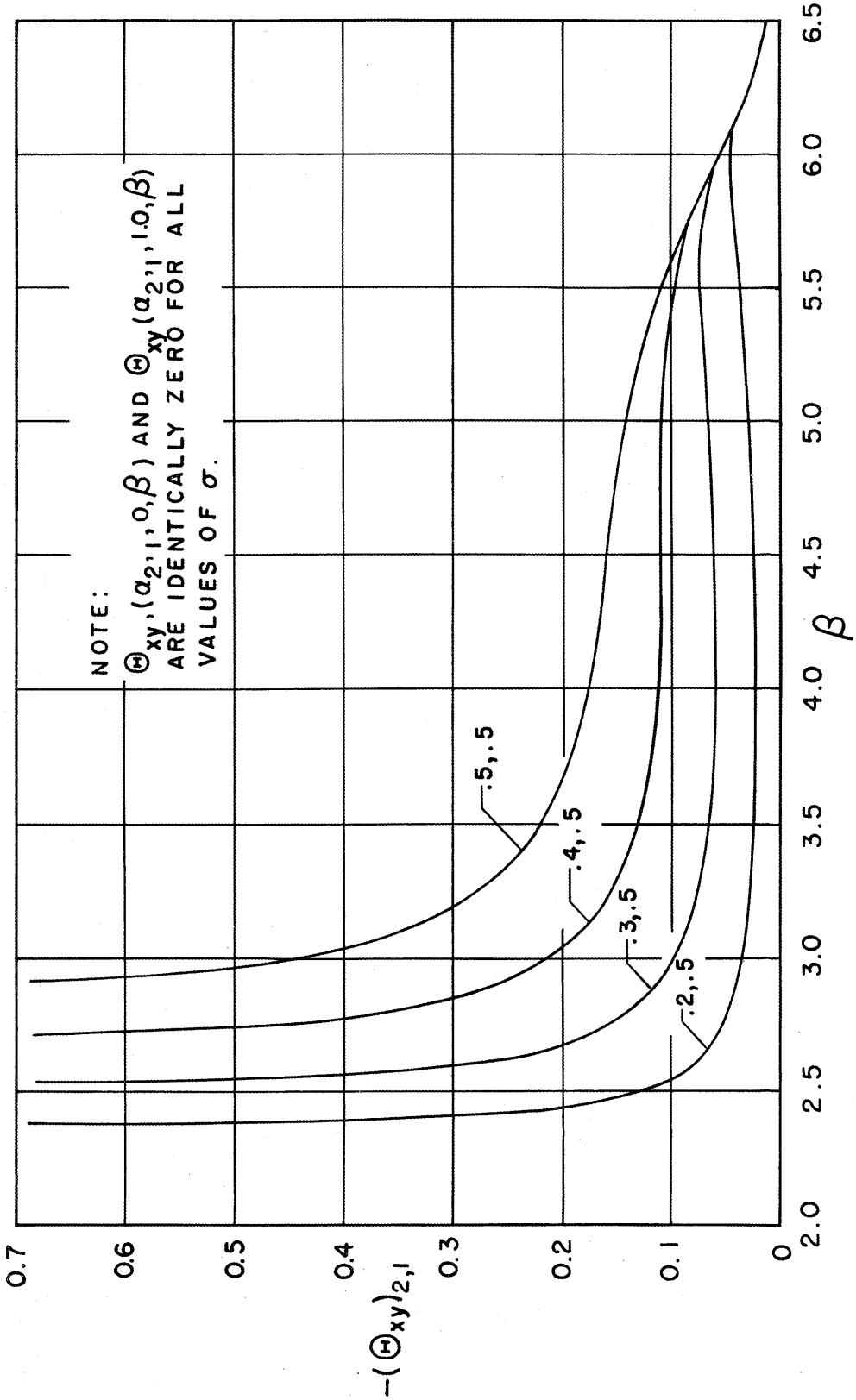

Figure 27. The functions $\Theta_{xy}'(\alpha_{2,1}',0,\beta)$, $\Theta_{xy}'(\alpha_{2,1}',0.5,\beta)$, and $\Theta_{xy}'(\alpha_{2,1}',1.0,\beta)$ in the region of real positive β corresponding to real $\alpha_{2,1}$ for $\sigma = 0.2$, 0.3, 0.4, and 0.5.

In problems where the Fourier transform of the end input is large for these large values of β (e.g. a delta function input), the higher modes may contribute a finite signal travelling at the dilatation velocity.

4. Remarks

The physical significance of the strain expressions which have been derived above will be examined in connection with experimental results in Part IV. Several general points will now be discussed briefly.

Concerning accuracy: A major drawback of saddlepoint methods of integration is the difficulty in accurately estimating the error. For the cases where $G(\beta)$ in equation 94 can be taken as a quasi-constant factor $G(\bar{\beta})$, Newlands (100) has given criteria for estimating the accuracies of both the o.s.p. and the e.s.p. methods in a semi-quantitative way. In the most important application of the e.s.p. method in the present problem, however, $G(\beta)$ is not quasi-constant; and in this case there is no scheme available for estimating the error. Consequently, experiments are required to answer the following questions which have not been considered: (i) Approximately how large must X be in order that the strain expressions be valid. (ii) How do the accuracies of two saddlepoint methods used in evaluating the expressions vary with time.

On pressure loading with known but arbitrary time dependence: It is worth noting that since the strain expressions derived above give the strain response of a given bar at position (x,y) and time t due to

a step function uniform normal stress applied to the end of the bar, the strains due to a known uniform normal stress loading having a known but arbitrary time dependence can be calculated using the superposition integral. The linearity of the governing differential equations makes this possible.

Let $A(x,y,t)$ be the known strain response at position (x,y) and time t due to a unit step-function input. If the actual input is $P(0)$ at $t = 0$, $P(\tau_1)$ at $t = \tau_1$, $P(\tau_2)$ at $t = \tau_2$, etc. then, by superposition, a strain component $e(x,y,t)$ is

$$e(x,y,t) = P(0)A(x,y,t) + [P(\tau_1) - P(0)]A(x,y,t - \tau_1) + [P(\tau_2) - P(\tau_1)]A(x,y,t - \tau_2) + \ldots \quad . \tag{136}$$

Letting $\Delta P(\tau_j) = P(\tau_j) - P(\tau_{j-1})$ and $\Delta \tau_j = \tau_j - \tau_{j-1}$, equation 136 becomes

$$e(x,y,t) = P(0)A(x,y,t) + \sum_{j=1}^{n} A(x,y,t - \tau_j) \left(\frac{\Delta P}{\Delta \tau} \right)_j \Delta \tau_j \quad . \tag{137}$$

For tabulated values of $A(x,y,t)$, $e(x,y,t)$ can be evaluated by numerically summing the series in equation 137. Curtis (101) has reported the results of such calculations for a round bar.

On the longitudinal impact problem: The normal displacement u at $x = 0$ can be specified instead of the normal stress τ_{xx}. The transform method is still applicable if "mixed end conditions" are considered. In this case, the normal displacement u and the shear stress τ_{xy} would be given for $x = 0$. To introduce this information the sine and cosine transforms of equations 3 through 6 must be interchanged;

otherwise, the solution procedure is analogous to that used in the pressure step problem.

Concerning the related plane strain problem: It has been repeatedly pointed out that by using transformation 2 all of the results obtained here are applicable to the corresponding plane strain problem of a semi-infinite slab with stress free lateral surfaces subject to the edge conditions that the stress τ_{xx} applied normally is uniform with a step function time dependence and that the lateral edge displacement v is zero.

The solutions given here to the plane stress problem should approximately describe the behavior of a wide rectangular bar when the wavelength is greater than the bar width. However, for the plane strain problem the solutions are not subject to such a restriction since they arise from the exact equations of motion for the slab. This is one reason why the solutions have been given in such detail.

IV. LONGITUDINAL ELASTIC STRAIN WAVE PROPAGATION IN WIDE RECTANGULAR BARS: EXPERIMENTAL OBSERVATIONS AND COMPARISON WITH THEORY

Introduction

In Part III, asymptotic expressions were obtained which, for large distances of travel, describe the longitudinal elastic strain wave propagation in a semi-infinite plane-stress elastic strip with stress free lateral edges, subject to the conditions that a uniform normal pressure with a step-function time dependence is applied to the end and that the end undergoes no lateral extension. These expressions were derived from the plane stress equations of motion, the lowest order approximate equations of motion that might be capable of describing the warping of plane sections, as observed in the fringe sequences of Part II, in a wide rectangular bar during the passage of a strain pulse. The purpose of the present part, Part IV, is to determine the usefulness of these expressions by comparing them with experimental observations.

Due to different methods of loading and to the problems associated with birefringent coatings and dynamic photoelasticity, only qualitative comparisons can be made between predicted and observed fringe patterns. An extensive experimental investigation using conventional strain measuring techniques was undertaken for the purpose of providing more critical tests of the theory.

Qualitative Comparison of Predicted and Observed Fringe Patterns

The fringe patterns in Part II were obtained for a longitudinal impact type of input whereas the expressions developed in Part III are for a pressure shock type of input. For large distances from the source

it is reasonable to expect that the solutions for the longitudinal impact and the pressure shock type problems would be essentially equivalent. Due to the mathematical similarity between the symmetrical vibrations of a plane-stress elastic strip and the corresponding vibrations of a cylindrical elastic bar, this supposition is supported by the observations of Miklowitz (55) on the equivalence of long-time pressure shock and longitudinal impact solutions for a cylindrical elastic bar. Although the fringe curvatures noted in figures 7 and 8 were observed relatively near the impacted end, it is expected that similar, but less pronounced, curvatures of the leading fringes would be observed at stations more distant from the end. This is the case in the pictures obtained by Durelli, et al. (26,102). On the basis of the foregoing discussion, the observed fringe curvatures at the head of the pulse will be qualitatively compared with the theoretically predicted curvatures.

For purposes of qualitative comparison it will be assumed that the isochromatic fringe order N observed at a point is proportional to the absolute value of the difference of the principal strains e_1 and e_2 at the point. In terms of the strain components e_{xx}, e_{yy}, and e_{xy}, the absolute value of the principal strain difference is (cf. (2))

$$|e_1 - e_2| = + \sqrt{(e_{xx} - e_{yy})^2 + (e_{xy})^2} \quad . \tag{138}$$

Considering only first mode contributions to the head of the pulse, the expressions for e_{xx}, e_{yy}, and e_{xy} are given by equations 120, 121, and 122, respectively. Figure 28 shows some calculated first mode contours of constant principal strain difference $\frac{E}{P_o}|e_1 - e_2|$ at time $t = 183.9$ microseconds for the head of the pulse in a 2024 T4 aluminum strip, for

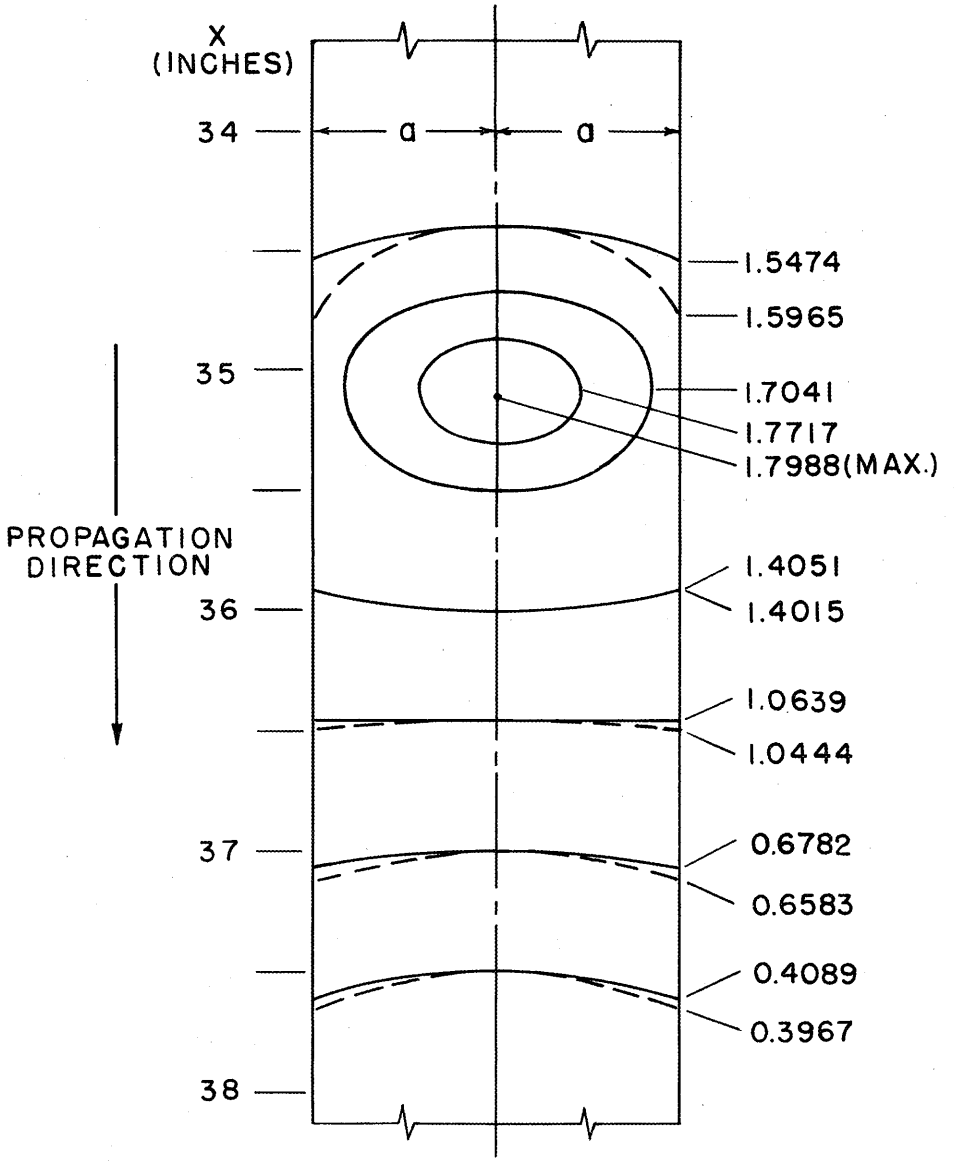

Figure 28. Predicted first mode contours of constant principal strain difference $(E/P_o)|e_1-e_2|$ at the head of the pulse. Time $t = 183.9$ microseconds, shear wave velocity $c_s = 0.1248$ inch per microsecond, Poisson's ratio $\sigma = 0.335$, and strip half-width $a = 0.75$ inch. Solid lines identify contours obtained using only the first two terms in each of equations 120 and 121 for e_{xx} and e_{yy}; dashed lines correspond to three terms.

which Poisson's ratio $\sigma = 0.335$, the shear wave velocity $c_s = 0.1248$ inch per microsecond, and the strip half-width $a = 0.75$ inch. The solid lines identify contours obtained using only the first two terms in each of equations 120 and 121 for e_{xx} and e_{yy}. For comparison several contours, indicated by dashed lines, are shown for which all three terms are included. In general, the additional terms serve to shift a particular contour and increase its curvature; otherwise, the general contour pattern is the same in both cases.

Figure 28 will be taken as qualitatively representing the predicted first mode fringe pattern at the head of the pulse. The leading fringes have concave curvatures with respect to the direction of wave propagation. As the fringe order increases, the curvature continuously changes from concave to convex. A fringe having essentially no curvature, indicating a uniaxial stress state, marks the transition from concave to convex curvatures. The fringe curvatures then become increasingly convex with the result that the fringes begin to close upon themselves, essentially appearing as ellipses of continuously decreasing size centered about a point. The point is a fringe source and it corresponds to the maximum fringe order at the head of the pulse. Continuing along the strip centerline, the fringe order decreases and the closed fringes give way to fringes having convex curvatures with respect to the direction of wave propagation.

The theory predicts that this general pattern is repeated for the first mode. This can readily be demonstrated from figures 17 and 28 if only the first two terms of each of the expressions for e_{xx} and e_{yy} are retained. First, it must be pointed out that the calculations for figure 28 show

$(e_{xy})^2 << (e_{xx} - e_{yy})^2$ so that $|e_1 - e_2| \cong |e_{xx} - e_{yy}|$, and that the first term in the expression for $|e_{xx} - e_{yy}|$ is at least an order of magnitude larger than the second term. At a particular time t, the first term of $|e_{xx} - e_{yy}|$ varies along the strip essentially as the Airy integral shown in figure 17 and the second term as the Airy derivative. Now, referring to figures 17 and 28 it is noted that the concave curvatures of the leading fringes occur when the derivative is positive. When the derivative passes through zero, only the first term remains and the resulting fringe has no curvature. The derivative then becomes negative, and the curvatures are increasingly convex until the first peak of the integral is reached, corresponding to the fringe source described above. This behavior occurs while the value of the first term is increasing much more rapidly, due to the order property, than the second term. Following the first peak the first term decreases much more rapidly than the second term and, since the derivative is still negative in the second term, the effect is now to give decreasingly concave curvatures. The derivative again passes through zero giving increasingly convex curvatures. In the neighborhood of the first dip of the integral a fringe sink is formed in the same manner as the preceding source. Referring to figure 17 it is seen that this general behavior continues, a second fringe source (of lesser order than the first) being formed at the second peak of the integral, a second fringe sink being formed at the second dip, etc.

The predicted first mode fringe pattern of figure 28 cannot be compared with the observed fringe pattern of figure 7 without first examining the influence of the higher modes. For relatively short distances from the loaded end the initial arrivals of the second mode

disturbances very closely follow the leading first mode disturbances (cf. figures 43 and 44); consequently, the beginning second mode disturbances, given by equations 127, 128, and 129, are expected to influence the leading edge of the pulse. Rough calculations for stations ahead of the fringe source in figure 28 indicate that the second mode contributions modify individual contours considerably, but that the general contour pattern of the leading fringes is unchanged. Qualitatively, then, the theory predicts the concave curvature of the leading fringe which was observed in figure 7.

It has already been pointed out in Part II that dynamic photoelasticity can give qualitative indications of elastic wave propagation phenomena. It was also noted that in the usual photoelastic materials, which exhibit viscoelastic behavior, the high-frequency components of a pulse are much more severely attenuated than those of lower frequency. Consequently, it is assumed that dynamic photoelastic fringe patterns obtained for the longitudinal impact of wide rectangular bars primarily reflect the behavior of the first mode and are best compared to the predicted first mode fringe pattern of figure 28. This supposition is supported by the present theory and the CR-39 attenuation measurements of Sutton (21) which indicate that the amplitudes of the first and initial second mode disturbances would be reduced after travelling 5 inches in a 1.5 inch wide rectangular bar of CR-39 by roughly 15 and 70 percent, respectively. For Hysol 8705 the relative attenuation of the higher modes is expected to be even more severe.

The predicted concave curvatures of the leading fringes are observed in the dynamic photoelastic pictures of Sutton (21) and Feder, et. al. (23) for the longitudinal impact of rectangular bars of CR-39. Further

comparisons between their pictures and figure 28 are not justified because of varying combinations of low fringe orders, poor resolution, and loading problems.

Dynamic fringe patterns obtained by Durelli, et al. (26,27,102) for longitudinally impacted rectangular bars of Hysol 8705, a low-modulus photoelastic material, are very interesting in terms of the predicted first mode fringe patterns. Using this material, maximum fringe orders of ten are easily attained and the transient fringe patterns can be photographed using relatively conventional techniques. A representative sequence of fringe patterns, reproduced from a report by Durelli and Riley (102), is shown in figure 29 for a rectangular bar 1.3 inches by 0.4 inch by 10 inches long. Impact loading was accomplished by dropping a 108-gram weight through a distance of 12 inches. A thin steel plate, lubricated to minimize frictional constraint, was used to distribute the load over the end of the bar. The fringe patterns were recorded with a Fastax camera operating at 12,500 frames per second. As a result of attenuation due to the viscoelastic behavior of the material, the maximum fringe order is observed to decay by roughly 50 percent as the wave propagates 5 inches down the bar.

A comparison of the fringe behavior observed in the frames at the right of the top row and at the left of the bottom row in figure 29 with the predicted first mode fringe behavior described above and shown in part in figure 28 indicates that there is good qualitative agreement between the observed and predicted fringe patterns at the head of the pulse. The theory properly predicts the observed concave curvatures of the leading fringes, the observed transition from concave to convex

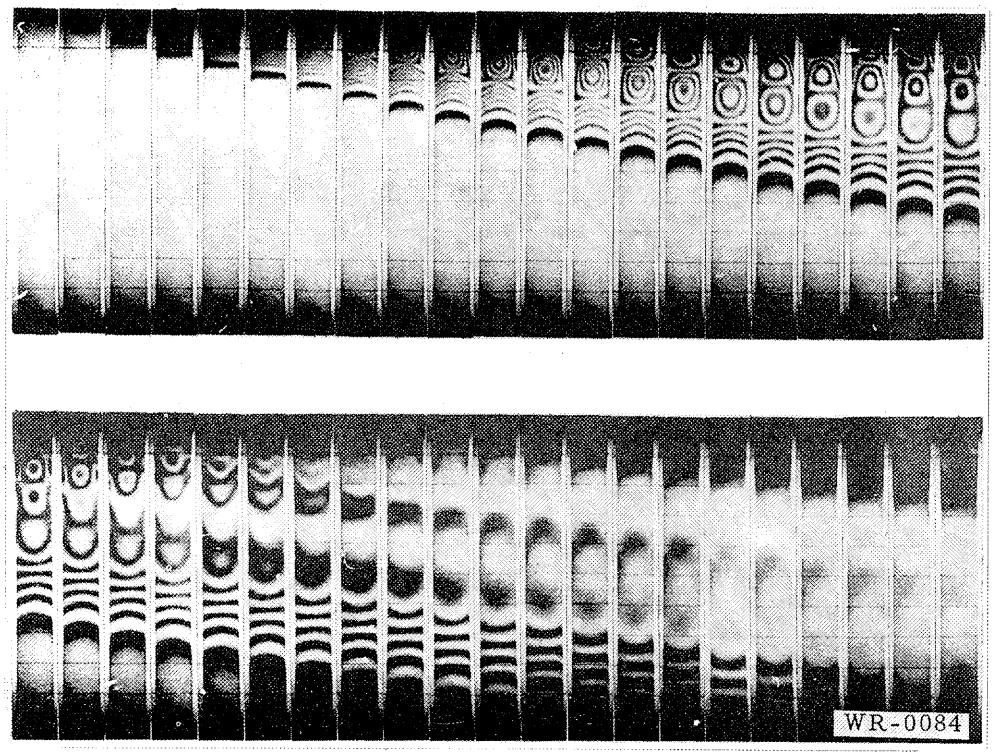

Figure 29. Dynamic fringe patterns associated with the propagation of a compressive stress wave along a rectangular bar of Hysol 8705 (After Durelli and Riley (102), p. 108).

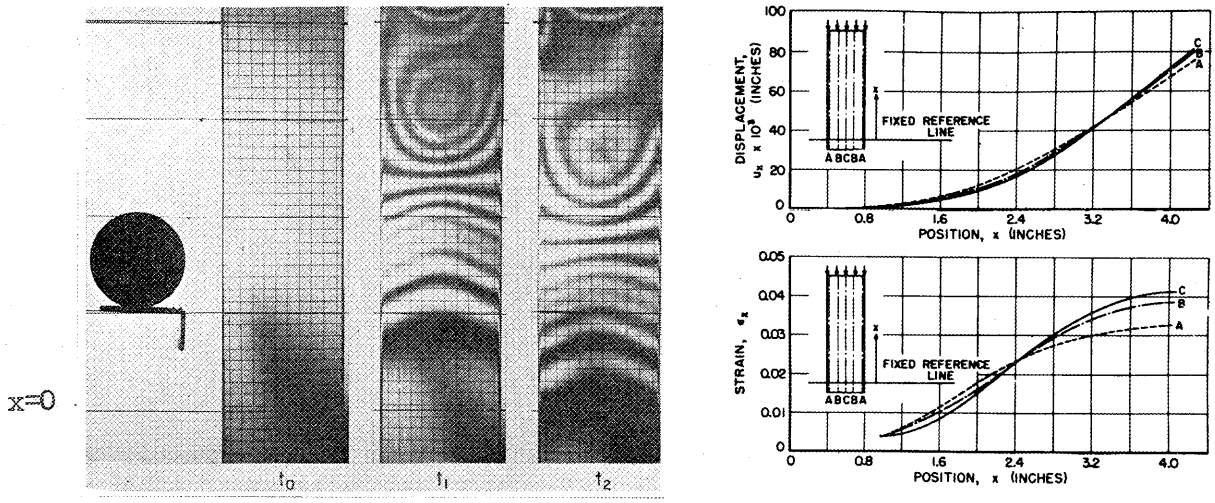

Figure 30. Microflash photographs taken before and during impact of a rectangular bar of Hysol 8705, and the results of subsequent grid measurements for the photograph labelled t_1 (After Durelli, Dally, and Riley (27), p. 631).

curvatures with increasing fringe order, the observed fringe source at the maximum fringe order, and the subsequently observed succession of increasingly closely spaced fringe sinks and sources.

Durelli, Dally, and Riley (27) have also used grid measurements in conjunction with dynamic photoelasticity to determine the stress distribution at a particular time in a longitudinally impacted rectangular bar of Hysol 8705. The grid measurements, however, are actually independent of the photoelastic measurements and they provide further qualitative support for the theory. Since Hysol 8705 is a low modulus material which exhibits relatively large displacements under small loads, it was possible to photographically record and accurately measure the dynamic displacements of a rubber-thread grid network embedded in the specimen. Figure 30, reproduced from the paper by Durelli, Dally, and Riley (27), shows microflash photographs taken before and during the impact of a rectangular bar, and the results of grid measurements for the photograph labelled t_1. The bar, 0.385 inch thick, 1.25 inches wide, and 7.375 inches long, was loaded by dropping a 216 gram weight through a distance of 16 inches. The displacement-versus-position curves shown in figure 30 for time t_1 were differentiated graphically to obtain the longitudinal strains e_{xx} for $y = 0$, $y = \pm a/2$, and $y = \pm a$ as functions of position.

The predicted first mode longitudinal strains $\frac{E}{P_o} e_{xx}$ for $y = 0$, $y = \pm a/2$, and $y = \pm a$ at time $t = 183.9$ microseconds are shown in figure 31 for the head of the pulse in a 2024 T4 aluminum strip, for which Poisson's ratio $\sigma = 0.335$, the shear wave velocity $c_s = 0.1248$ inch per microsecond, and the strip half-width $a = 0.75$ inch. Only

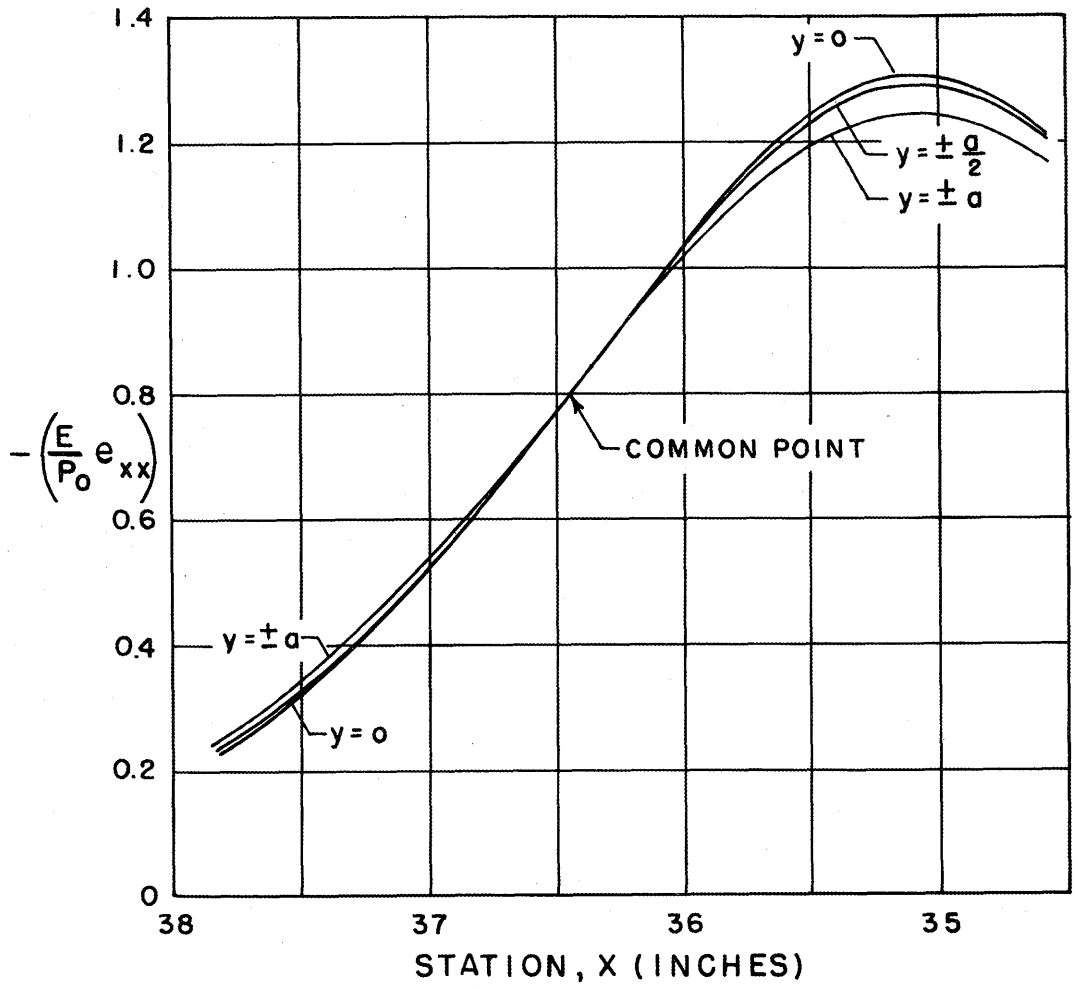

Figure 31. Predicted first mode longitudinal strains $(E/P_o)e_{xx}$ for $y = 0$, $y = \pm a/2$, and $y = \pm a$ at the head of the pulse, according to the first two terms of equation 120. Time $t = 183.9$ microseconds, Poisson's ratio $\sigma = 0.335$, shear wave velocity $c_s = 0.1248$ inch per microsecond, and strip half-width $a = 0.75$ inch.

the first two terms in equation 120 were used in the calculations. A comparison of figures 30 and 31 shows that the observed behavior of the longitudinal strain e_{xx} for $y = 0$, $y = \pm a/2$, and $y = \pm a$ at the head of the pulse is qualitatively predicted by the theory.

On the basis of the above comparisons, it is apparent that the theoretical expressions developed in Part III provide a good qualitative description, at least for the first mode, of the observed warping of plane sections during the propagation of a strain pulse along a wide rectangular bar.

Further Experiments: More Critical Tests of the Theory

1. Experimental Requirements

In view of the good qualitative agreement between observed and predicted fringe patterns, an experimental program was undertaken for the purpose of providing more critical tests of the theory. The experimental results of this program should be of general interest since very little experimental information is presently available in the literature for the propagation of longitudinal strain pulses in rectangular bars.

To provide meaningful results, an experimental study of a longitudinal elastic strain pulse during propagation in a wide rectangular bar should satisfy the following requirements:

(i) The stress which is applied to the bar to produce the strain pulse must be known as a function of both position and time. It is desirable that this applied stress be of such a nature as to allow convenient mathematical treatment. In order to correlate experimental results, it must also be reproducible.

(ii) The bar must be sufficiently long to allow adequate observation times at several widely separated stations along the bar.

(iii) There must be suitable means of detecting and recording the strain pulse. In particular, a detector should be used which is capable of measuring the non-uniform strain distributions across the width of the bar as predicted by the theory.

(iv) The influence of thickness on the strain pulse propagation in a bar of given width must be investigated to adequately assess the usefulness of the two-dimensional theory.

In the following section the way in which each of these requirements has been met will be discussed.

2. Experimental Equipment and Procedure

Loading arrangement: The general experimental arrangement is shown in figure 32. Stress is applied to one end of a long rectangular aluminum bar by the reflection of a shock wave in air from the end face. The shock wave is produced in a conventional shock tube by bursting a diaphragm between a high pressure chamber and a channel originally at atmospheric pressure.

The shock tube, fabricated from seamless steel tubing and high-pressure steam piping flanges, has an inside diameter of 1 3/4 inches, a chamber length of 1 1/2 feet, and a channel length of 4 1/4 feet. Initially the chamber and channel are separated by a diaphragm consisting of three layers of 0.0075 inch thick Mylar film. To produce a shock wave, the diaphragm is ruptured by filling the chamber with helium to a gage pressure of approximately 600 psi. In bursting, the Mylar film produces no fragments which can travel down the shock tube and damage the face of the bar.

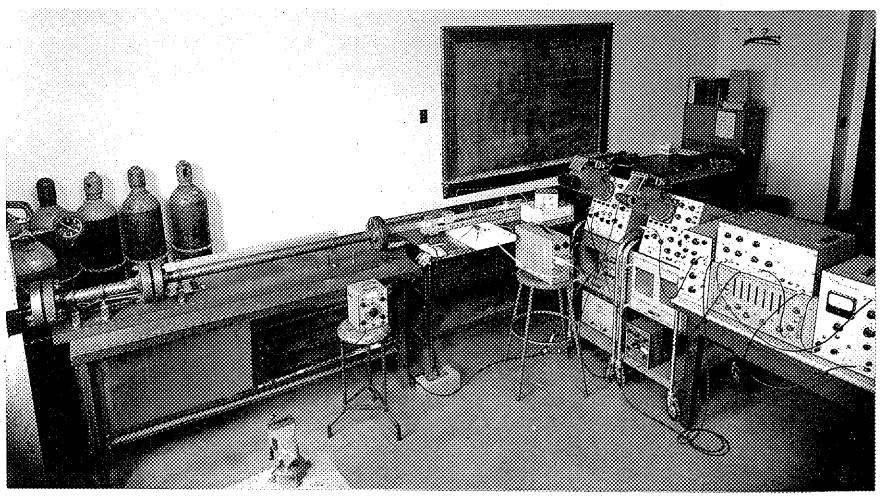

Figure 32. Apparatus for producing and detecting transient strains in rectangular bars.

(Left, shock tube; center, aluminum bar and strain detection devices; right center, oscilloscopes and time delay generator; right, time mark generating equipment.)

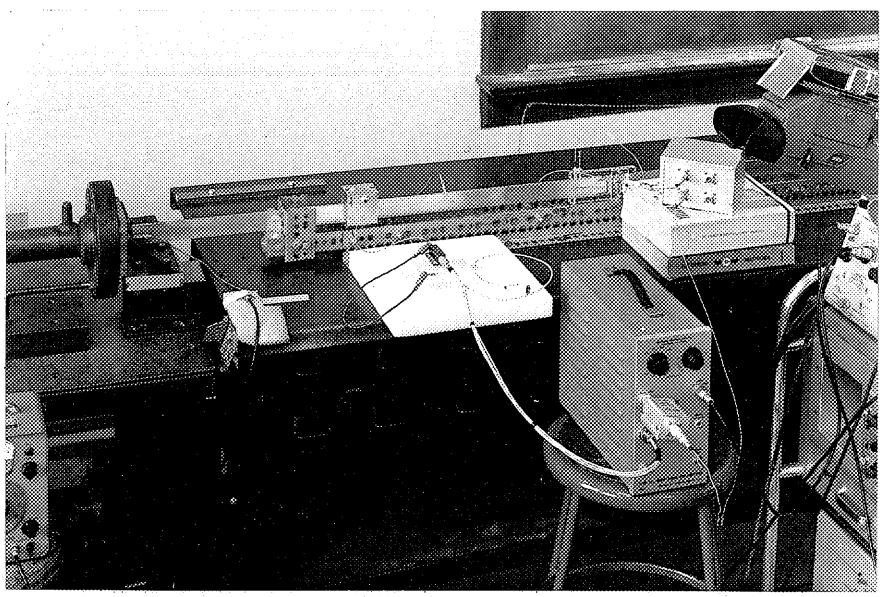

Figure 33. Close-up showing strain detection equipment and details of loading arrargement at the end of the bar.

(Left, lucite plate, bracket, and pressure pickup; left center, bar support; center, shielded strain gage and cathode follower; right, condenser microphone pickup unit, feed unit, and preamplifier.)

The end of the shock tube is essentially closed by a 1/2 inch thick lucite plate backed up by a heavy steel bracket as shown in figure 33. The end of the aluminum bar fits into a carefully machined rectangular hole in the lucite plate so that its end face is flush with the surface of the plate. The hole is approximately 0.003 inch oversize in both dimensions. The lucite plate is adjusted relative to the bar until the clearances between the sides of the bar and the hole are equal. A pressure pickup is also mounted in the plate. An air gap of approximately 0.025 inch between the end of the shock tube and the lucite plate insures against mechanical coupling.

The aluminum bar is supported and constrained laterally by slotted holders at four points along its length, with its centerline aligned with that of the shock tube. To minimize interactions between the supports and the bar, the holders are made of lucite which is a poor impedance match with aluminum, and the length of the contact area at a support is made small compared to the wavelengths to be observed. The unloaded end of the bar is clamped to prevent rigid body motion. As shown in figure 32, the entire bar support assembly is mounted on a table separate from the table on which the shock tube assembly is mounted. In this way the bar is effectively isolated from the shock tube assembly until the shock wave reflects from its end face. No disturbances due to mechanical coupling between the bar and the shock tube could be detected experimentally during the times of interest.

Theoretical calculations based on idealized one-dimensional flow (cf. (103)) predicted that for a chamber pressure of 600 psi helium the reflected shock should produce a step pressure on the end of the bar of

roughly 700 psi which remains constant for about 800 microseconds. Experimental measurements using a Kistler PZ6 quartz pressure pickup in conjunction with a Kistler PT6 impedance matching amplifier-calibrator indicated that the pressure actually remains constant at about 650 psi for approximately 400 microseconds.

During the course of the experiments, no attempt was made to measure the absolute magnitude of either the applied pressure or the resultant strains in the bar. Instead it was assumed that the applied pressure is proportional to the final value of the strain and the amplitudes of the strain pulse oscillations were measured relative to this value.

The stress applied to the end of the bar has a component only in the normal direction and is uniform over the entire end face. Since all measurements are made during the time the pressure remains constant, the time dependence of the applied stress may be considered as a step function. This method of loading, then, experimentally provides the step function pressure load considered in the mathematical treatment of Part III, but does not duplicate the other mathematical end condition of zero lateral extension, since the bar is subjected to no lateral constraint. It was pointed out in Part III that failure to satisfy the second end condition is expected to be relatively unimportant for strains at large distances from the end.

To investigate the influence of bar thickness, strain measurements were made for three rolled 2024 T4 aluminum bars having essentially the same widths but different thicknesses. The respective cross-sectional dimensions of the three bars are 0.064 inch by 1.484 inches,

0.126 inch by 1.501 inches, and 0.252 inch by 1.501 inches. Each of the bars is 130 inches long. With bars of this length it is possible to observe most of the interesting features of the strain pulse for distances of travel up to about 115 inches.

Detection and recording of strains: The maximum strain produced in the aluminum bars in the present experiments is of the order 10^{-4}, and it is necessary to observe strain differences at least two orders of magnitude smaller than this if strain contributions corresponding, for example, to the last two terms in equations 120 and 121 are to be distinguishable. This immediately rules out the use of wire resistance strain gages for which the noise-to-signal ratio is too great for the measurement of such small strains.

A major feature of the present theory is the prediction of non-uniform strain distributions across the width of the bar; consequently, it is desirable that a detector be used which is capable of either directly or indirectly making measurements which will test this aspect of the theory. In particular, considering first mode contributions to the head of the pulse, it would be desirable to be able to determine from such measurements whether all three or only the first two terms are required in equations 120 and 121 for e_{xx} and e_{yy}, respectively.

Disregarding the third terms, an inspection of equations 120 and 121 for a particular value of σ reveals that the second term is generally much larger for e_{yy} than for e_{xx}. It is found that integrating equation 121 across the strip to obtain the first mode contribution to the change in strip width greatly magnifies the importance of the second term relative to the first term. A similar result follows for the third term. For example, for the aluminum bars described above the calculated values

of the second and third terms at the first peak for $x = 37.5$ inches are, respectively, about 9 and 5 percent of the first term. Second mode contributions at the head of the pulse are obtained by integrating equation 131 across the strip and evaluating the resulting expression for the two initial second mode arrivals. The calculations show that changes in the strip width at the head of the pulse due to the second mode are negligible. Thus, by measuring changes in strip width at the head of the pulse, the effects of the second and third terms in equation 121 can be examined. Provided the theory is applicable, these effects should be experimentally observable.

The experimental setup for recording changes in bar width is shown schematically in figure 34. Two condenser microphone pickups mounted directly opposite each other detect the displacements of the edges of the bar. This type of pickup has been successfully used by other investigators (41,44,104) to measure displacements associated with strain pulses in cylindrical bars and thin sheets. Davies (41) presents a very thorough and general analysis of their operation.

An edge surface of the grounded bar serves as one plate of a parallel-plate condenser. The pickup contains the other plate which is charged up to 600 volts through a battery feed unit. The feed unit consists of a 600 volt battery and a condenser resistance arrangement of long time constant so that the charge on the parallel-plate condenser is essentially constant for the duration of the elastic disturbance. When a strain pulse passes the observation station the capacity of the parallel-plate condenser changes which consequently results in corresponding changes in the potential difference across it. When the relative change in capacity is small this potential difference is directly proportional to the displacement of the edge of the bar. The sensitivity is increased by mounting two pickups

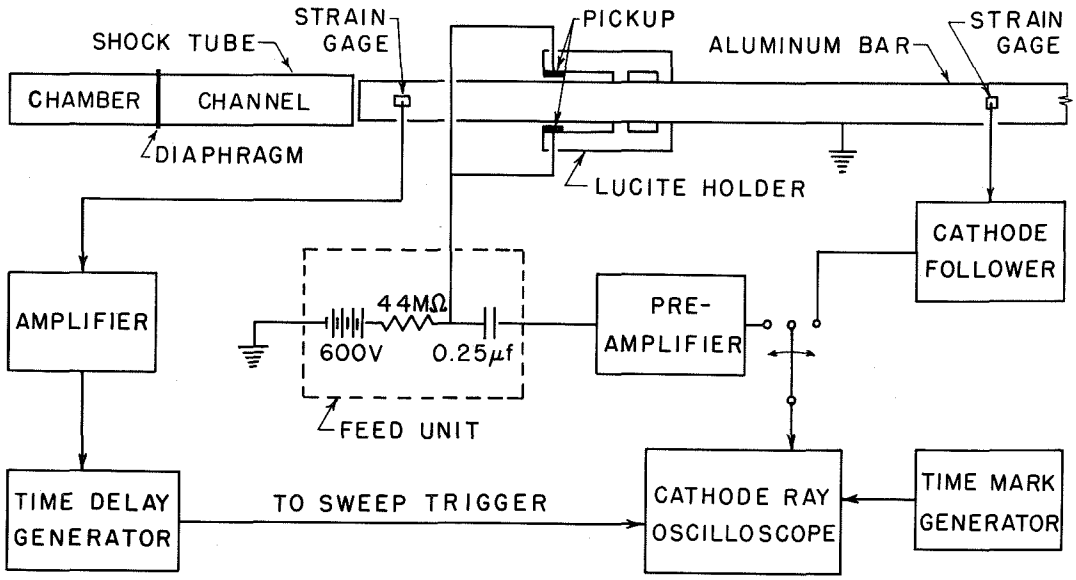

Figure 34. Schematic diagram of apparatus for producing and detecting transient strains in rectangular bars.

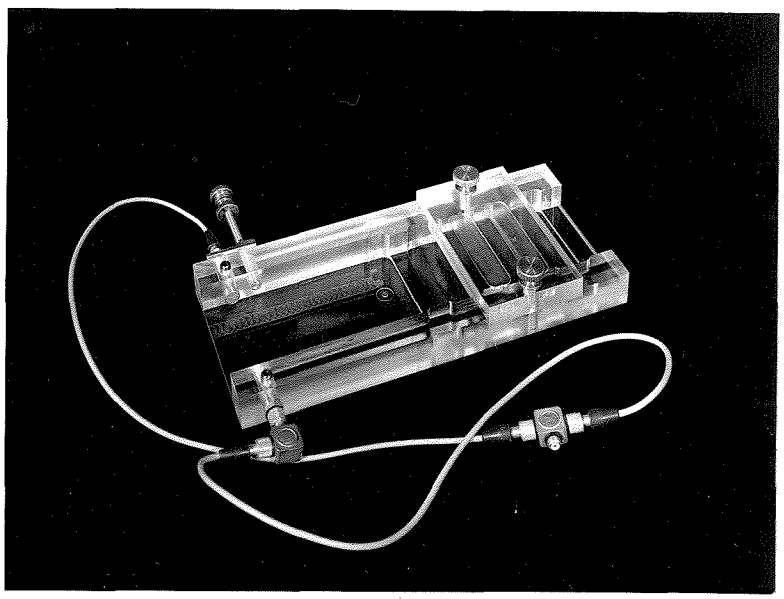

Figure 35. Condenser microphone pickup unit.

directly opposite each other and connecting them in parallel. This arrangement also minimizes pickup of any extraneous lateral rigid body displacements of the bar.

The combined signal from the two pickups is amplified and displayed by a wide-band system (5 cycles per second to 12 megacycles) consisting of a Tektronix 121 wide-band preamplifier followed by a Tektronix 551 dual-beam oscilloscope having Type L fast-rise plug-in preamplifiers, and photographically recorded on Polaroid 3000 film using a DuMont 302 oscillograph camera. Simultaneously, the other beam of the oscilloscope provides a base line and time markers. The time markers are generated by an Electro-Pulse 3450A megacycle pulse generator synchronized with a Tektronix 105 square-wave generator which in turn is synchronized with the one megacycle frequency standard of a Beckman-Berkeley 7360 counter. The square-wave generator is used to meet the 25 volt synchronization requirement of the pulse generator.

The oscilloscope is used in a single-sweep mode of operation. For the 0.064 and 0.126 inch thick bars, sweep triggering is provided by means of a barium titanate piezoelectric strain gage mounted 2.00 inches from the loaded end of each bar. The signal from this gage, resulting from the passage of the strain wave, is amplified by a Tektronix 112 preamplifier and used to start a DuMont Type 326 adjustable time delay generator which then produces a sweep triggering pulse of about 50 volts at the desired instant. For the 0.252 inch thick bar, sweep triggering is provided by similarly amplifying and delaying the pressure signal generated by the aforementioned Kistler pressure pickup mounted flush with the face of the lucite plate closing the shock tube.

The condenser microphone pickup unit used in the present experiments

is shown in figure 35. Since the capacity between the pickups and the bar was very small (being of the order of a picofarad), particular care was taken to design the pickups for minimum electrical pickup. A pickup is made by soldering a 0.200 inch diameter brass cylinder to the terminal of a Microdot 31-50 receptacle. An aluminum sleeve screws onto the receptable to provide a continuous coaxial ground shield. The end of the sleeve is flush with the plane end surface of the brass cylinder. Microdot "Mininoise" coaxial cable and fittings were used to connect the pickups to the feed unit, and the feed unit to the preamplifier. This minature cable is specially treated so that cable movement does not generate a signal. For an overall oscilloscope deflection sensitivity of 200 microvolts per centimeter, a.c. pickup could not be detected.

The pickups are held in position by an accurately machined lucite holder which fits on the bar as shown in figure 33. Using shims and lubricant, the holder is adjusted to have a sliding fit on the bar with negligible sloppiness. To isolate the pickups from any disturbance transmitted to the holder during the recording of a signal, the pickups are cantilevered with respect to the holder supports. Any disturbance in the bar being sensed by the pickups has to travel to the holder supports and back along the lucite holder before it can disturb the pickups. Thus a delay of at least 70 microseconds is obtained permitting recording of the early part of the strain pulse without possible extraneous signals.

The spacing between the pickups and the bar was set using a 0.0025 inch feeler gage. This is approximately 130 times the expected maximum displacement of the edge of the bar; therefore, the maximum error in assuming the pickup output is directly proportional to the displacement is roughly 0.75 percent.

In addition to the condenser microphone arrangement for recording edge displacements of the bar, barium titanate piezoelectric strain gages, which have a sensitivity several hundred times that of commercial wire resistance strain gages, were used to obtain records of the strains at localized points along the bar. It was expected that these gages would be sensitive to disturbances associated with the higher modes of transmission.

Barium titanate strain gages, in the form of thin wafers which can be mounted on a surface, have been used before by several investigators (105,106,45,107,108) to record dynamic strains. Except for (108), the wafers used in these investigations have been rectangular, the length being considerably greater than the width. Some critical remarks on the use of such gages is in order.

Since the wafers are polarized in the direction normal to the plane of strain, their cross sensitivity factors are inherently equal to unity. Ideally, then, the response of a gage should be proportional to the sum of the principal strains acting at the surface in question. Mark and Goldsmith (109) carried out a series of tests to determine whether wafers of piezoelectric barium titanate bonded to dynamically stressed members could serve as practical strain transducing elements. For wafers bonded with Duco cement, they found experimentally that the measured cross sensitivity factors for bonded gages depended on the wafer geometries. For example, for a 1/16 inch wide by 5/8 inch long wafer, the cross sensitivity factor was about 0.3. The shear stress distribution in the cement bond gives rise to these effects. Intuitively, for a long narrow gage the shear stress in the bond builds up to a constant value over a large percentage of the length, whereas

it builds up and then falls to zero almost immediately across the gage width. Thus, the gage response is predominantly due to strains in the direction of the larger dimension.

Apparently unaware of Mark and Goldsmith's work, both Fox (45) and DeVault (107) used long narrow gages and erroneously assumed that the gage response was proportional to the sum of the principal strains in their experimental studies of elastic strain pulse propagation in cylindrical bars. Yet, they found excellent quantitative agreement between theory and experiment. This is due to the fact that in their experiments the principal strains at the bar surface are proportional to each other; consequently, cross sensitivity effects appear only as amplitude factors in their experimental measurements. Since no absolute strain measurements were attempted, their experimental results are independent of cross sensitivity effects.

Considering Fox's work, for example and recalling the mathematical similarity between the propagation of a longitudinal strain pulse in a cylindrical bar and a strip, it can be seen from equations 120 and 121 that $e_{yy} = -\sigma e_{xx}$ at the strip edges, which correspond to the surface of the bar. Using only the first two terms, the same equations indicate that the error in assuming $e_{yy} = -\sigma e_{xx}$ at the bar centerline would be about 15 percent. It must be concluded that Fox's conclusions would have been different had it been possible to measure strains in the interior of a cylindrical bar.

In general, then, to avoid bond cross sensitivity effects the gages should be circular. Square gages can be used without introducing cross sensitivity effects if they are oriented parallel to the directions

of the principal strains. Goodier, Jahsman, and Ripperger (108) used circular gages in their investigations.

In the present experiments, 1/8 inch square by 0.01 inch thick Glennite barium titanate strain gages were mounted with Duco cement midway between the bar edges at several stations along one side of the bar. Flexible lead wires were soldered to the exposed electrode faces of the gages using Cerrolow No. 174 solder and Superior No. 30 flux. Soldering was accomplished at about 200^{o}F which was well below the Curie point of the gages. The bar, held at ground potential, served as the other electrode connection.

Electrically a gage can be considered as a zero impedance generator in series with a capacitance numerically equal to the capacitance of the gage (cf. (109)). The gage is paralleled by the load capacitance and resistance. The load capacitance does not reduce the high frequency response, but acts as a voltage divider. To extend the low frequency response, the load impedance should be as large as possible to give a long time constant; ideally the load resistance should be infinite. However, the finite resistance of the gage (about 10^{12} ohms) precludes d.c. operation.

The experimental setup for recording the strain gage output is shown schematically in figure 34. The signal from the strain gage is fed into a Glennite KAHT-310 cathode follower, which has an input impedance of about 100 megohms, and then into the oscilloscope. As shown in figure 33, the gage is shielded by a metal can and Microdot "Mininoise" cable is used to connect the gage to the cathode follower. Tests showed that the frequency response of the cathode follower was

essentially flat between 3 cycles per second and 300 kilocycles. The remainder of the instrumentation has already been discussed in connection with the condenser microphone pickups.

3. Elastic Constants of the Bars

In order to evaluate any of the equations developed in Part III to predict the nature of the strain pulse, a knowledge of the elastic constants of the three rolled 2024 T4 aluminum bars used in the present experiments is required.

No dynamic measurements of the elastic constants of 2024 aluminum alloy could be found during a brief literature survey; however, measurements for several other alloys were found. Depending on the alloy, the available values exhibit substantial variations. A major criticism of the available results is that the conditions describing the state of the specimen, such as heat treatment, cold-working, and orientation, are usually not mentioned in reporting the work. Because of the uncertainty in assigning the elastic constants of the aluminum bars from available information, an experimental study was undertaken for the purpose of accurately measuring them.

Method of measurement: The measurements were made using the pulse method described by Hughes, Pondrom, and Mims (110). The general technique seems to have been first used by Firestone (75). Experimentally it is observed that a sharp compressional (or dilatational) pulse applied to one end of a solid cylindrical specimen appears at the other end not as a single pulse but as a series of pulses equally spaced in time. The initial signal travels the length of the bar with the dilatational velocity and the trailing pulses arrive separated by an interval which depends on the diameter of the bar and on the ratio of the shear to

dilatational wave velocities.

These effects have been interpreted using the theory for the reflection of plane unending wave trains at a stress-free surface. This theory indicates that in general a dilatational wave incident on a stress-free surface generates a shear wave as well as a reflected dilatational wave. It has been suggested that the delayed pulses are due to incident dilatational waves, which travel at grazing incidence to the rod surface, being reflected from the surface and breaking up into dilatational waves at grazing reflection and generated shear waves which travel at an angle θ relative to the surface normal. The angle θ is defined by the limiting relation $\sin\theta = c_s/c_d$, c_s and c_d denoting the shear and dilatational wave velocities, respectively, in the unbounded medium. These shear waves strike the opposite side of the rod and are partially converted back into dilatational waves at grazing reflection which proceed with dilatational velocity.

From experimental measurements of the travel time, t_d, of the undelayed dilatational wave and the shear delay time, Δt, the elastic constants of the bar can be determined on the basis of this theory (cf. (110)). The shear wave velocity c_s and Poisson's ratio σ are given by

$$c_s = \frac{D}{\Delta t}\left[1 + \left(\frac{Dt_d}{L\Delta t}\right)^2\right]^{-1/2} \tag{139}$$

and

$$\sigma = \frac{1}{2}\left[1 - \left(\frac{Dt_d}{L\Delta t}\right)^2\right], \tag{140}$$

where D is the diameter and L is the length of the cylindrical specimen.

The theory presented above adequately accounts for the delayed dilatational pulses. However, there is an apparent defect in this simple theory which points to the need for a more detailed interpretation. The difficulty is that for the limiting case of grazing incidence this theory requires that the amplitudes of the incident and reflected dilatational waves cancel out completely and the amplitude of the shear wave be zero, so that there is neither motion nor stress anywhere. Meitzler (111) and Roesler (112) have studied this situation and point out that the delayed dilatational pulses arise through a process more like diffraction than reflection. Redwood (92) has developed a modification of the Pochhammer frequency equation which predicts the delayed pulses.

Experimental arrangement: The elastic constants were measured for a cylindrical specimen machined from a scrap piece of the 0.252 inch thick 2024 T4 rolled aluminum bar used in the present experiments. The specimen is 0.2500 $\pm$.0002 inch in diameter and 1.9960 $\pm$.0005 inches long. Its axis corresponds to the direction of rolling which was along the length of the original bar. It is assumed that the elastic constants obtained for this specimen are also applicable to the 0.064 and 0.126 inch thick bars.

The experimental arrangement is shown schematically in figure 36. The cylindrical specimen is driven at one end by an X-cut quartz crystal cemented between it and a lead bar which is about 1/4 inch in diameter

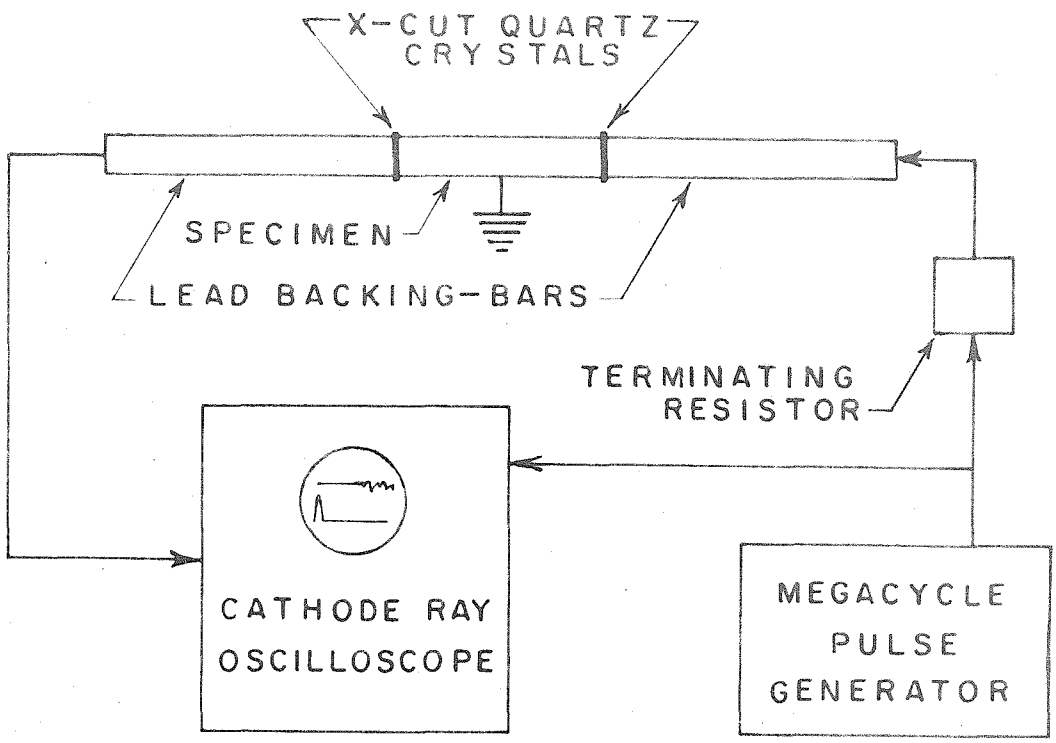

Figure 36. Schematic diagram of apparatus for measuring elastic constants of an aluminum specimen.

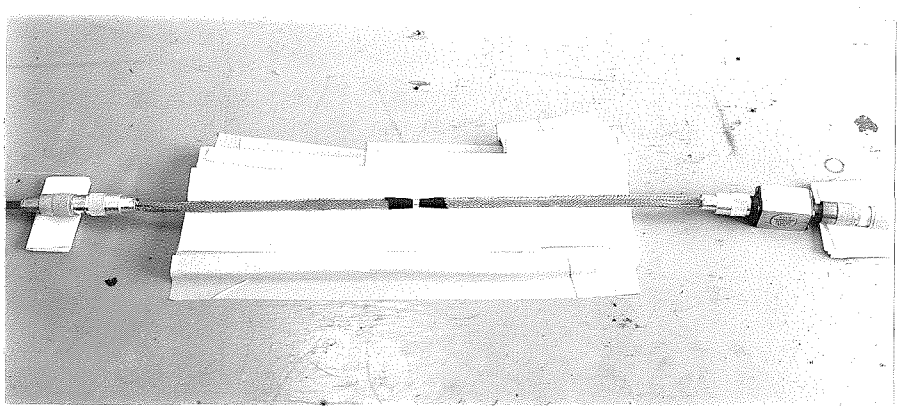

Figure 37. Specimen assembly for elastic constant measurements.

and 6 inches long. A similar arrangement at the other end of the specimen serves as the detector. The quartz crystals are 0.250 inch in diameter and have a fundamental frequency of 25 megacycles for free longitudinal vibration in the thickness direction. The purpose of the lead backing-bars is to minimize reflections.

Phenyl salicylate, a normally crystalline compound which turns into a low viscosity liquid at temperatures above 110°F, was used as the cement because of its good transmission characteristics and convenience. Bonding was accomplished by heating the members to be joined, introducing liquefied phenyl salicylate into the joints, and then allowing the assembly to cool causing the phenyl salicylate to crystallize.

Electrically, the specimen is held at ground potential and the lead backing-bars serve as the lead connections to the crystals. To minimize pickup between the crystals, the lead bars are covered with vinyl and braided wire ground sheaths and connected to UHF fittings as shown in figure 37.

Pulses having a risetime of about 0.02 microsecond, a duration of about 0.06 microsecond, and an amplitude of approximately +30 volts are applied through a 93 ohm terminating resistor to the driving crystal at 60 microsecond intervals by an Electro-Pulse 3450A megacycle pulse generator. The resulting signals from the detecting crystal are displayed on one beam of a Tektronix 551 dual-beam oscilloscope having Type L fast-rise plug-in amplifiers. The driving pulse can be displayed on the other beam. The pulse frequency spectrum extends to roughly 15-75 megacycles, which corresponds to a dilatational wave-length of

0.025 inch to 0.005 inch in aluminum. The transmitted pulses are so short that it is impossible for the first delayed wave train to interfere with the undelayed wave train, etc.

To measure the times t_d and Δt, one cycle of the square-wave output from a Tektronix 105 square-wave generator was visually matched on the oscilloscope screen against the transmitted pulse display by adjusting the square-wave frequency. The period was determined from the square-wave frequency which was accurately measured using a Beckman-Berkeley 7360 counter.

Results: Typical photographic records of the display are shown in figures 38a, b, and c. The initial undelayed dilatation pulse and the trailing delayed dilatational pulses are shown in the upper trace of figure 38a. Details of the driving pulse can be seen in the lower trace of figure 38b. Figure 38c shows the initial undelayed dilatational pulse and the first two trailing pulses in detail.

The measured times for t_d and Δt are 7.94 $\pm$0.03 microseconds and 1.736 $\pm$.006 microseconds, respectively. From these values, the shear wave velocity c_s and Poisson's ratio σ for 2024 T4 aluminum are calculated from equations 139 and 140 to be

$$c_s = (3.17 \pm 0.02) \times 10^3 \text{ meters per second,}$$

and

$$\sigma = 0.336 \pm 0.002.$$

For 17S duraluminum Mason (39) gives values of 3,130 meters per second and 0.335 for the shear wave velocity and Poisson's ratio, respectively. Since the compositions of 2024 and 17S alloys are quite similar the agreement is not too surprising.

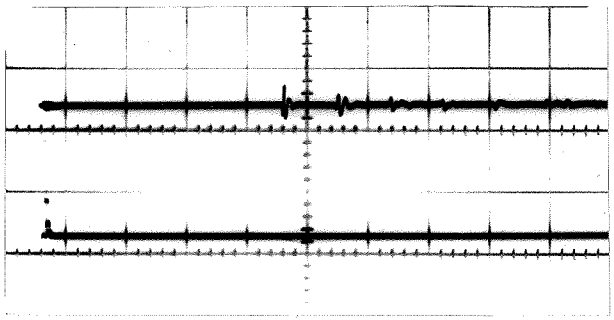

a) Upper beam, transmitted dilatational pulses; lower beam, driving pulse. Sweep time 2 microseconds per grid division.

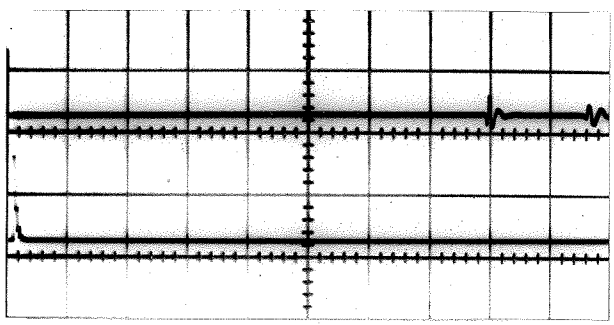

b) Same as (a) except sweep time 1 microsecond per grid division.

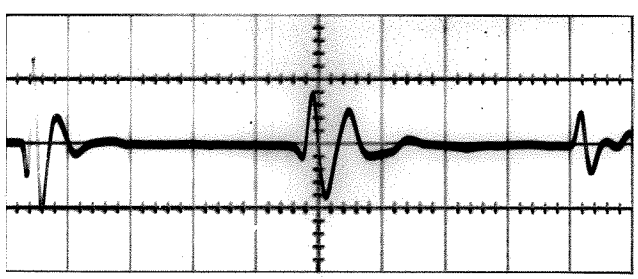

c) Details of first three transmitted pulses. Sweep time 0.4 microsecond per grid division.

Figure 38. Typical records showing pulse transmission through a 0.2500 inch diameter 2024 T4 aluminum rod in the direction of rolling. Rod length is 1.996 inches.

For evaluating expressions developed in Part III the shear wave velocity and Poisson's ratio are taken as 0.1248 inch per microsecond and 0.335, respectively.

4. Comparison of Experimental Records with Theory

General discussion of experimental records: The experimental records are shown in figures 39, 40, 41, and 42 for stations $x = 18.75$, 37.5, 75.0, and 112.5 inches, respectively. For each station, condenser microphone and barium titanate strain gage records are shown for the three wide rectangular 2024 T4 aluminum bars described previously, which have cross-sectional dimensions of 0.064 inch by 1.484 inches, 0.126 inch by 1.501 inches, and 0.252 inch by 1.501 inches, respectively. For a condenser microphone record, the output is proportional to the change in bar width; for a strain gage record, the output is proportional to the sum of the principal strains midway between the edges of one side of the bar. For stations $x = 75$ and 112.5 inches, long time records are shown which have twice the duration of the corresponding short time records. The long time records show the overall behavior of the strain pulse whereas the short time records show details of the head of the pulse. Measuring from the instant of load application, the starting time and estimated limits of error are given for each record by $t = t_o$. In arriving at the starting times for the 0.064 and 0.126 inch thick bars it was assumed that the disturbance producing the triggering pulse travels with the dilatational wave velocity.

All of the records were found to be highly reproducible with respect to time. For a particular record, only the relative amplitudes of the oscillations are important since no attempt was made to measure absolute

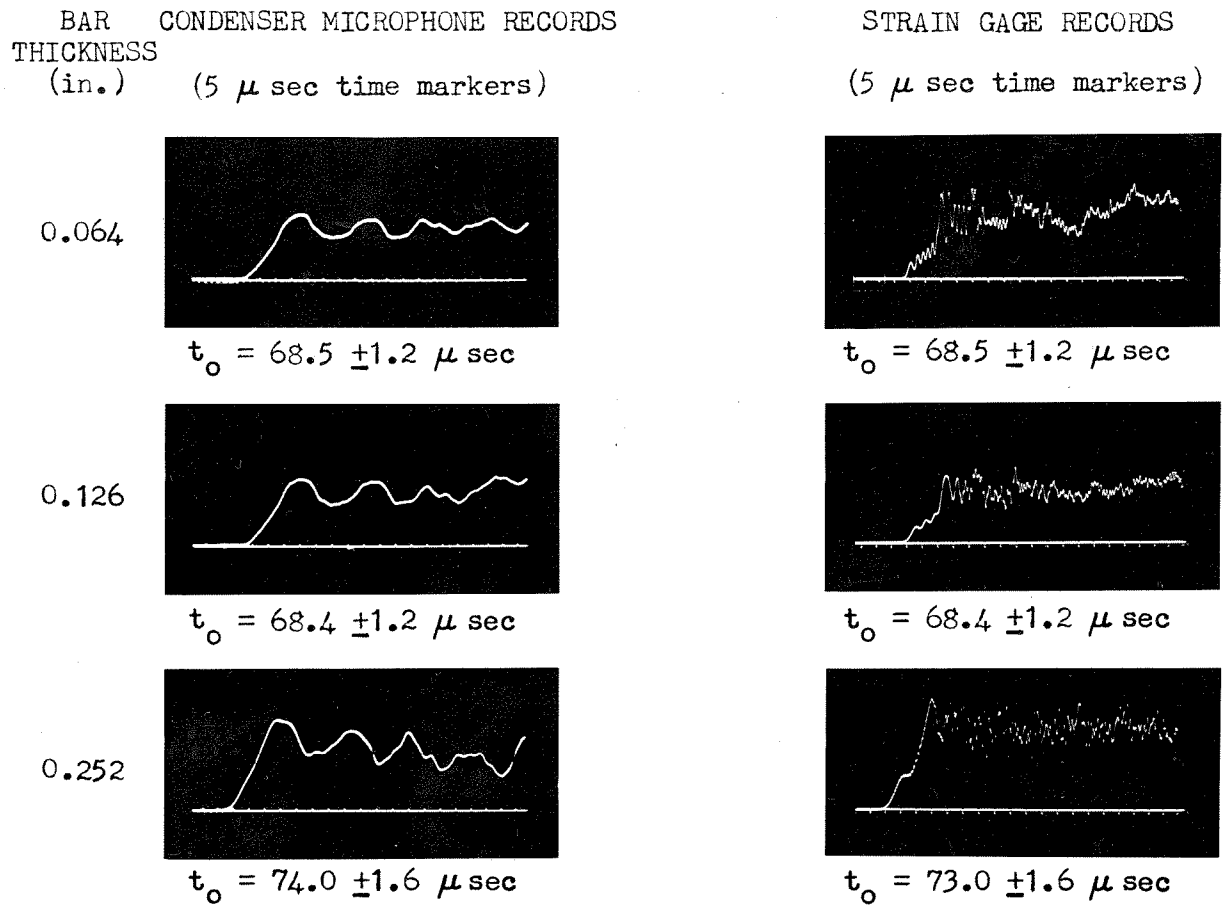

Figure 39. Condenser microphone and barium titanate strain gage records of the strain pulse at station x = 18.75 inches resulting from the application of a step-function pressure to the ends of three rectangular 2024 T4 aluminum bars of different thicknesses. The respective cross-sectional dimensions of the three bars are 0.064 in. by 1.484 in., 0.126 in. by 1.501 in. and 0.252 in. by 1.501 in. Taking $t = 0$ to be the time of pressure application, $t = t_o$ is the starting time for a record.

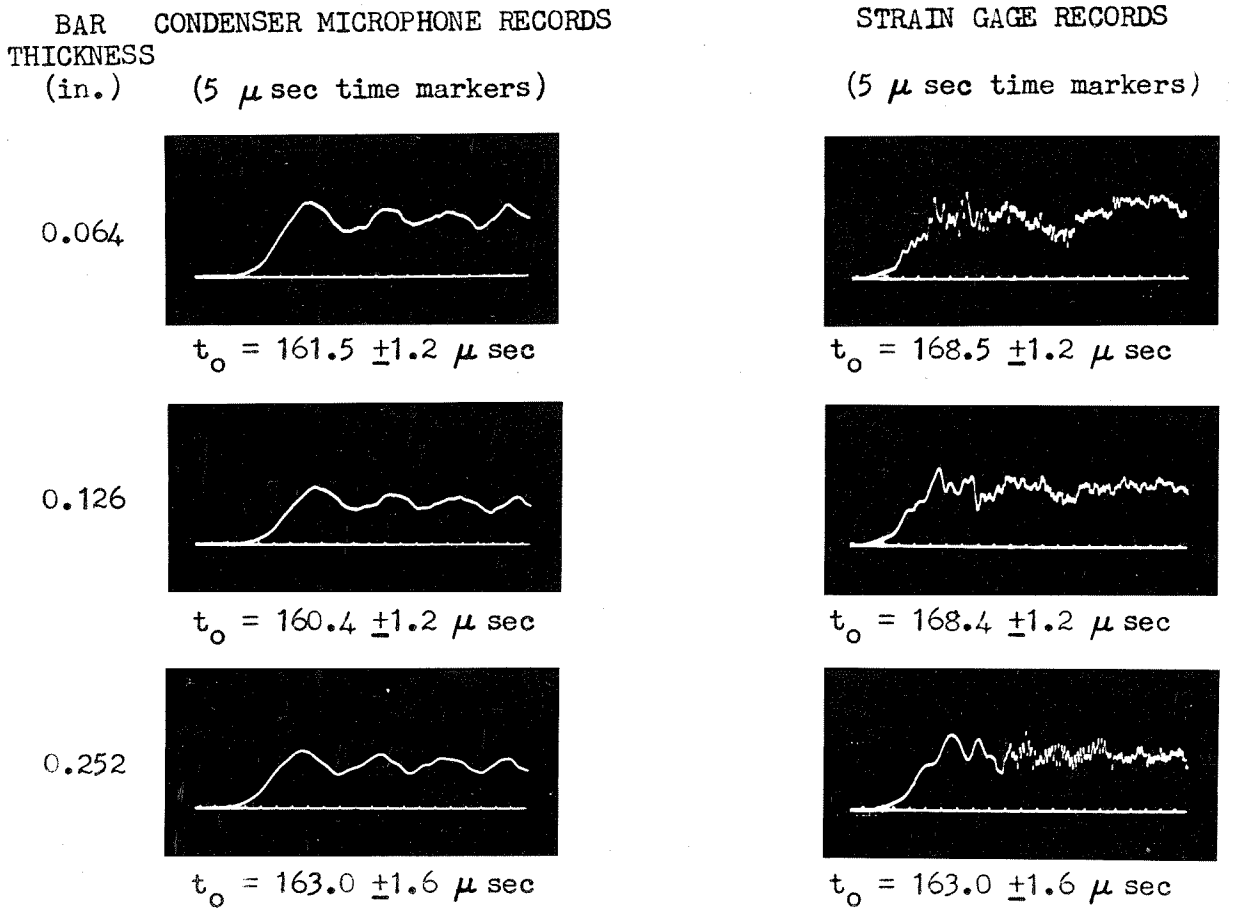

Figure 40. Condenser microphone and barium titanate strain gage records of the strain pulse at station x = 37.5 inches resulting from the application of a step-function pressure to the ends of three rectangular 2024 T4 aluminum bars of different thicknesses. The respective cross-sectional dimensions of the three bars are 0.064 in. by 1.484 in., 0.126 in. by 1.501 in. and 0.252 in. by 1.501 in. Taking $t = 0$ to be the time of pressure application, $t = t_o$ is the starting time for a record.

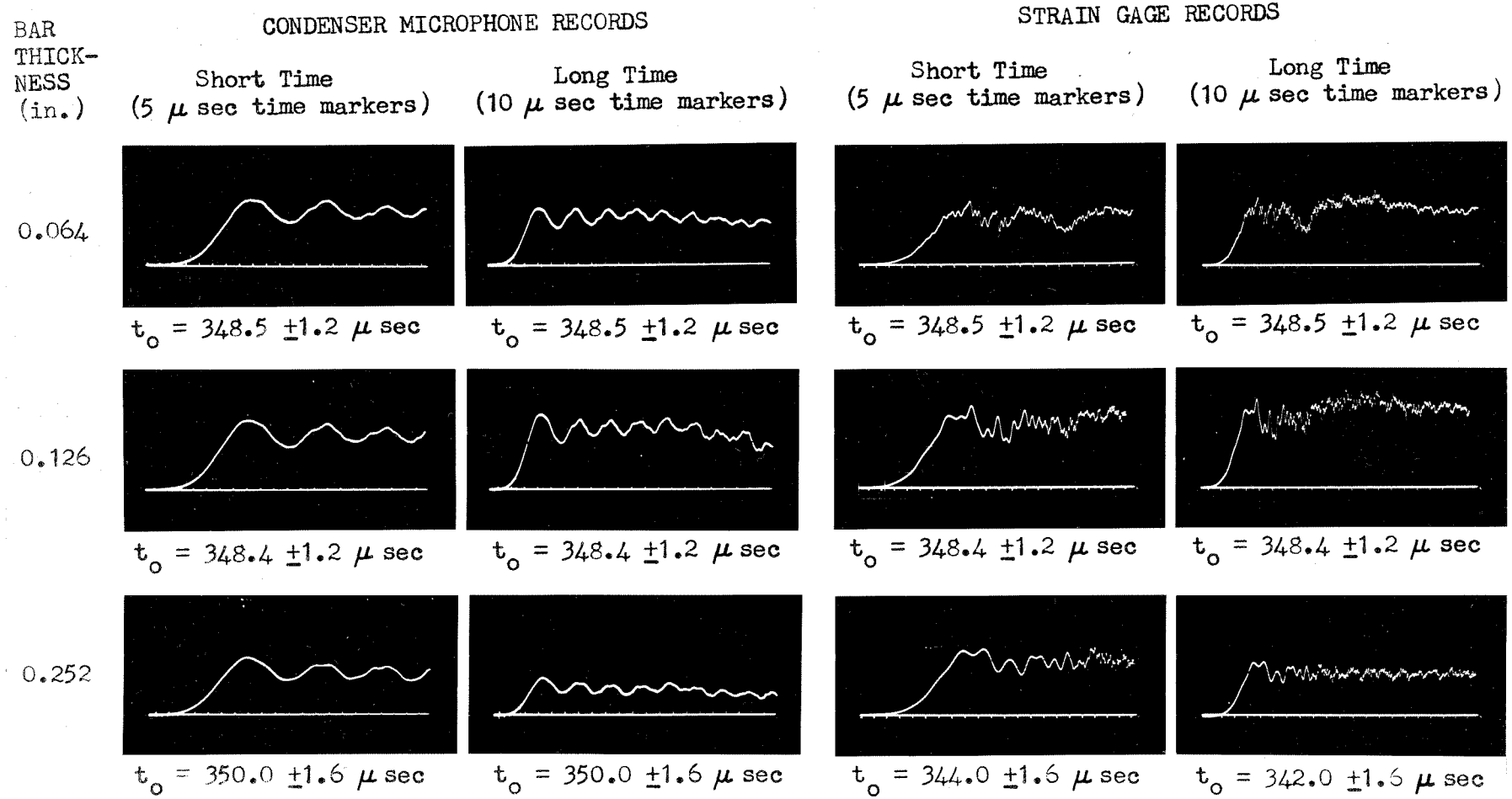

Figure 41. Condenser microphone and barium titanate strain gage records of the strain pulse at station x = 75.0 inches resulting from the application of a step-function pressure to the ends of three rectangular 2024 T4 aluminum bars of different thicknesses. The respective cross-sectional dimensions of the three bars are 0.064 in. by 1.484 in., 0.126 in. by 1.501 in. and 0.252 in. by 1.501 in. Taking $t = 0$ to be the time of pressure application, $t = t_o$ is the starting time for a record.

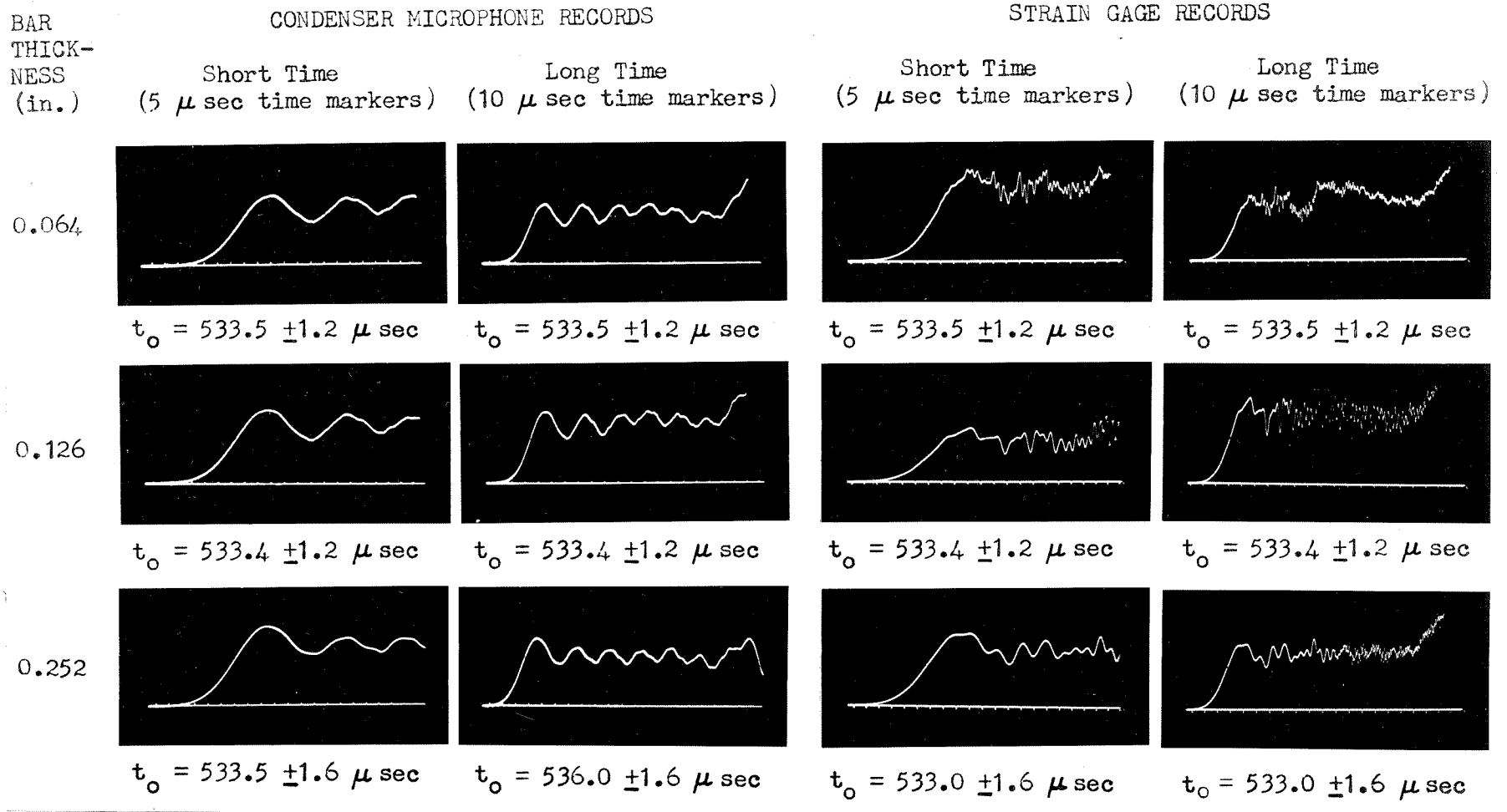

Figure 42. Condenser microphone and barium titanate strain gage records of the strain pulse at station x = 112.5 inches resulting from the application of a step-function pressure to the ends of three rectangular 2024 T4 aluminum bars of different thicknesses. The respective cross-sectional dimensions of the three bars are 0.064 in. by 1.484 in., 0.126 in. by 1.501 in. and 0.252 in. by 1.501 in. Taking $t = 0$ to be the time of pressure application, $t = t_o$ is the starting time for a record.

magnitudes. Unfortunately, the relative amplitudes at a given station for a particular bar and detector were not as reproducible as the time variations. Differences ranging up to 8 percent were observed for the 0.126 and 0.252 inch thick bars, and up to 15 percent for the 0.064 inch thick bar. The cause of these differences is not known. However, the extreme flexibility of the 0.064 inch thick bar may be worth noting.

If there was no dispersion, the experimental records would have the simple form of a step function. Clearly, they bear only a rough resemblance to a step. The strain gage records, in particular, exhibit complicated behavior very shortly after the initial arrival of the pulse. This is in agreement with the arrival time predictions of the approximate ordinary saddlepoint analysis of the theory. According to this analysis, saddlepoints corresponding to the real $\alpha_{2,1}$ branch of the second mode for positive β become real very shortly after the first mode saddlepoints become real. The analysis also indicates that saddlepoints associated with the real $\alpha_{2,2}$ branch of the second mode for positive β become real almost immediately after the initial second mode arrivals. For convenience, these groups of saddlepoints and their contributions will be labelled [1,1], [2,1], and [2,2], respectively. For $\sigma = 0.335$, figures 43 and 44 show, respectively, the dominant period $\bar{\tau}$ and wavelength $\bar{\lambda}$ associated with the real [1,1], [2,1], and [2,2] saddlepoints as a function of time t for a particular station x. The minimum values of t/x for which the saddlepoints first become real (corresponding to the formation of third order saddlepoints) are given on these figures. For moderate distances of travel x, it is clear from these values that second mode contributions to the strain pulse should be present at the head of the pulse.

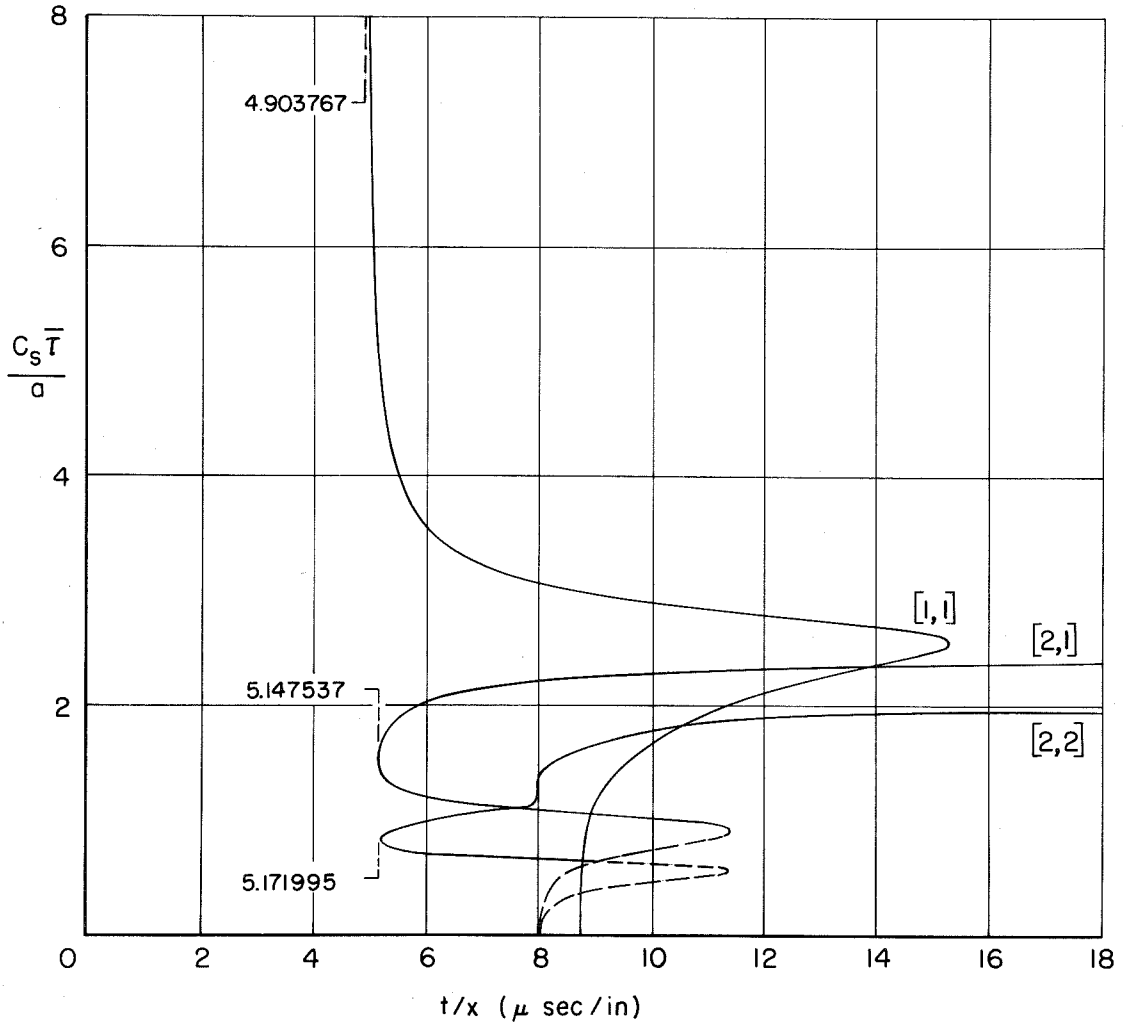

Figure 43. Dominant periods $c_s \bar{\tau}/a$ associated with real [1,1], [2,1], [2,2] saddlepoints as a function of time t for a particular station x. Poisson's ratio $\sigma = 0.335$. Solid lines correspond to calculated values; dashed lines correspond to values obtained from interpolation between values for $\sigma = 0.3$ and 0.4, from individual hand-calculations, and from asymptotic expansions.

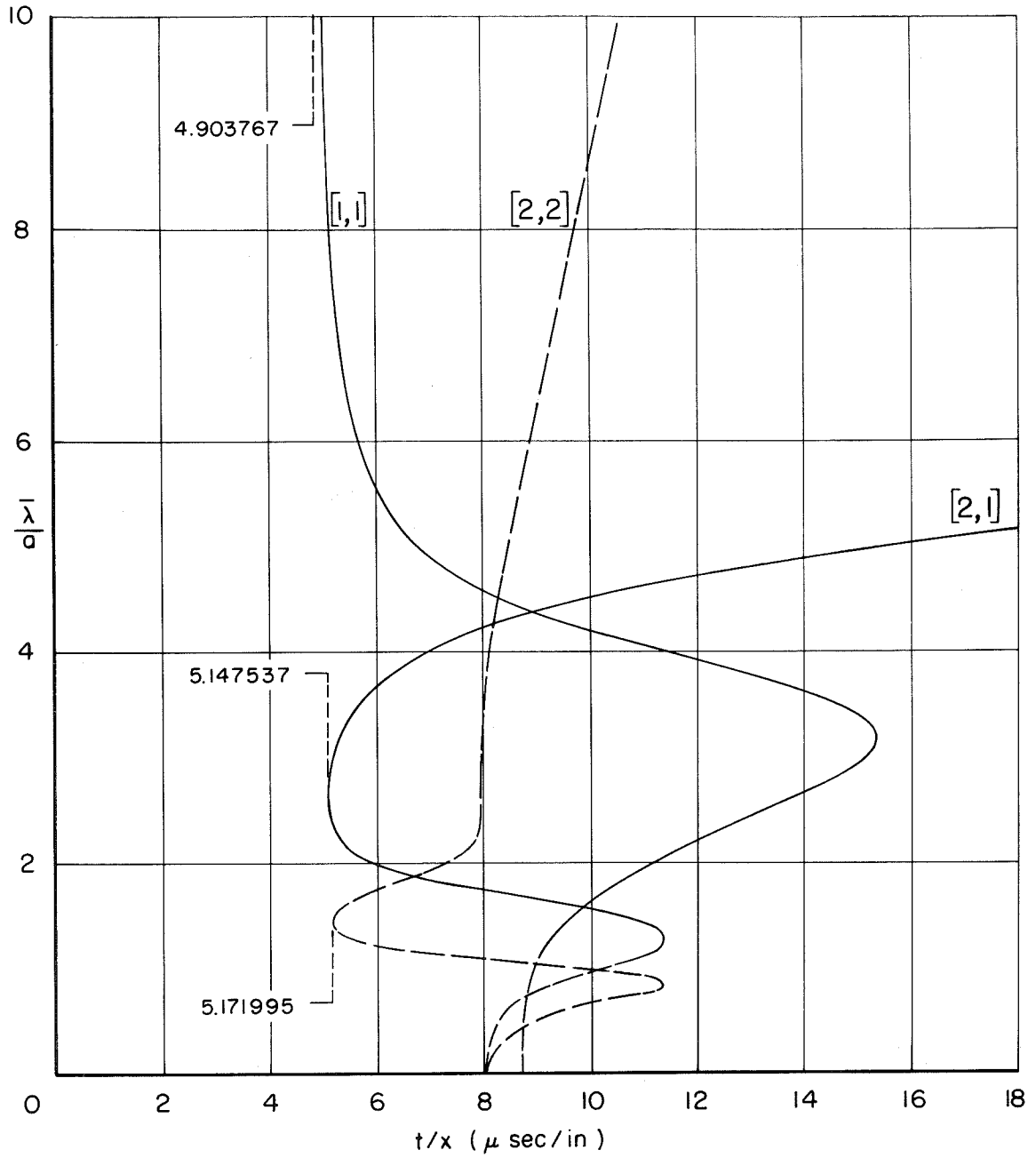

Figure 44. Dominant wavelengths $\bar{\lambda}/a$ associated with real [1,1], [2,1], and [2,2] saddlepoints as a function of time t for a particular station x. Poisson's ratio $\sigma = 0.335$. Solid lines correspond to calculated values; dashed lines correspond to values obtained from interpolation between values for $\sigma = 0.3$ and $\sigma = 0.4$, from individual hand-calculations, and from asymptotic expansions.

Morse's experimental work (57) for wide rectangular bars, which was discussed in Part III, indicates that no propagation takes place in the lowest thickness mode below a cut-off frequency which occurs when $\bar{\lambda}/a = 4$, i.e., when the half wavelength is equal to the bar width. From figure 44 it is observed that both of the initial second mode arrivals violate this condition; thus, it is expected that thickness effects should be observable in the experimental records. Indeed, oscillations associated with the bar thickness are clearly observed in the leading portions of the strain gage records of figures 39 and 40 for stations $x = 18.75$ and 37.5 inches.

The extremely early arrivals of non-negligible second mode disturbances for relatively large distances of travel were not anticipated in the original development of the theory. It was originally hoped that higher mode disturbances would either be negligible or arrive late enough so that the first mode of the two-dimensional plane-stress theory would be adequate for describing the head of the pulse. This is clearly not the case in the strain gage records and it remains to determine whether the plane-stress theory will predict even the gross features of these records.

The condenser microphone records, on the other hand, exhibit relatively much less complicated behavior than the corresponding strain gage records. In general agreement with these records, it will be shown in the next section that the theory predicts that the initial second mode contributions to the change in width of the bar are negligible at the head of the pulse.

In the following sections the theoretical predictions for the head of the pulse will be compared in detail with the observed experimental behavior. Only first and second mode contributions will be considered in the theoretical predictions. All theoretical calculations will be based

on a Poisson's ratio σ of 0.335, a shear wave velocity c_s of 0.1248 inch per microsecond, and a bar half-width a of 0.75 inch.

Comparison of condenser microphone records with theory: The predicted condenser microphone response, which is proportional to the transverse displacement v at the edge $y = a$ of the strip, is shown in figures 45 and 46 for the head of the pulse at stations $x = 37.5$ and 112.5 inches, respectively. The first mode contribution is obtained by integrating equation 121 across the strip half-width. The second mode contributions are obtained by integrating equation 131 across the strip half-width and evaluating the resulting expression separately for each of the two initial second mode arrivals.

It is clear that the first mode correction terms, which describe the non-uniform strain distribution across the strip for the first mode, serve to magnify the changes in the strip width. As shown in the figures, the magnitude of these correction terms decreases with the distance of travel. The second mode contributions, as shown in figures 45 and 46, are relatively small. They consist primarily of the [2,1] contribution, the [2,2] contribution being essentially zero. For the initial [2,1] contribution, roughly the center half of the bar width is in tension (compression), while the outside quarter widths of the bar are in compression (tension), as indicated in figure 26. The effects do not entirely cancel and thus give rise to the small [2,1] contribution. For the initial [2,2] contribution, roughly the portion of the bar width from $y = -a/4$ to $y = +a/4$ is in tension (compression), the portions from $y = a/4$ to $3a/4$ and from $y = -a/4$ to $-3a/4$ are in compression (tension), and the remaining portions are in tension (compression). The effects cancel almost exactly so that the [2,2] contribution is negligible. Although the

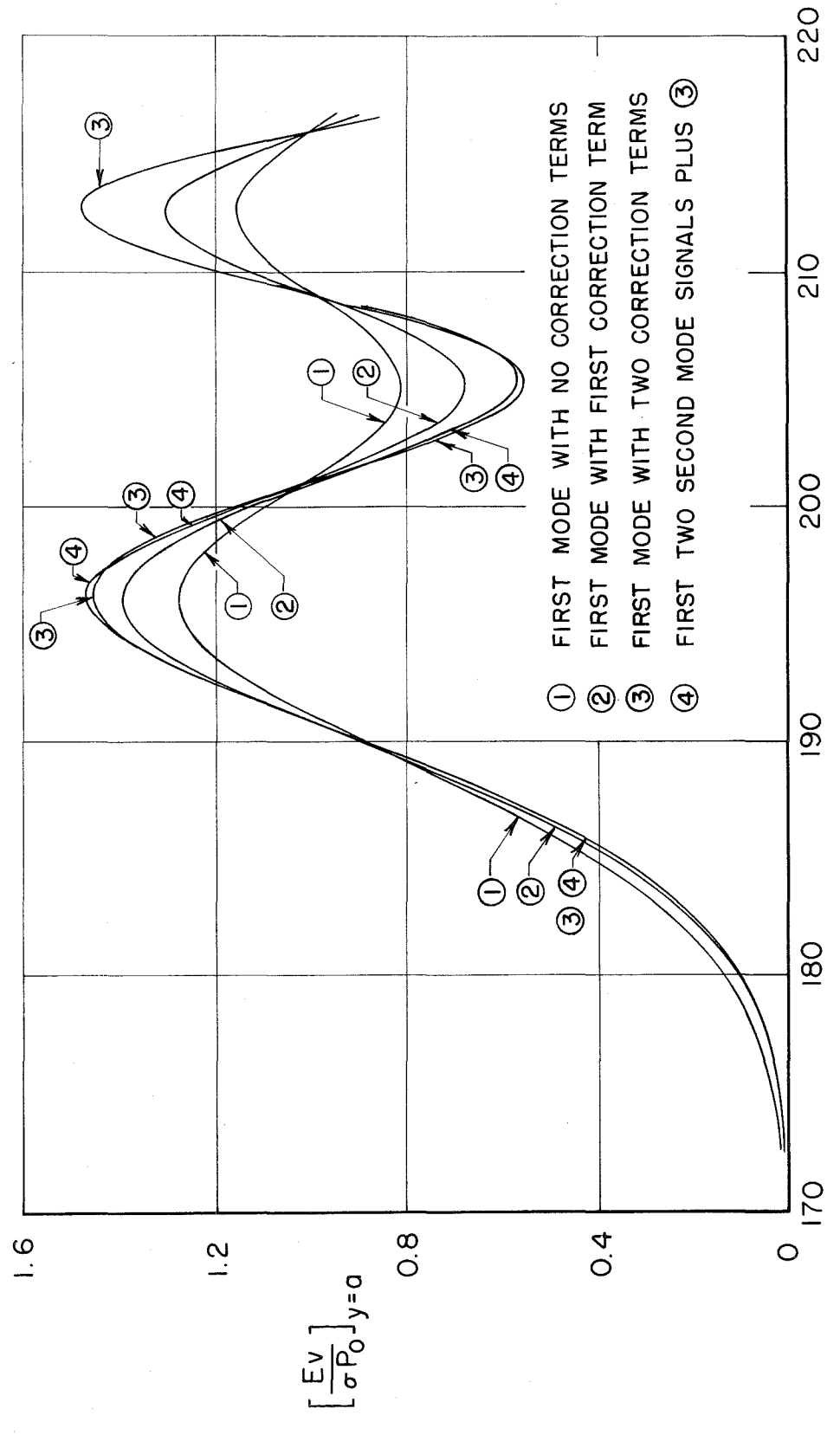

Figure 45. Predicted displacement $(Ev)/(\sigma P_o)$ at strip edge $y = a$ for the head of the pulse at station $x = 37.5$ in. Shear wave velocity $c_s = 0.1248$ in./μ sec, Poisson's ratio $\sigma = 0.335$, and strip half-width $a = 0.75$ in.

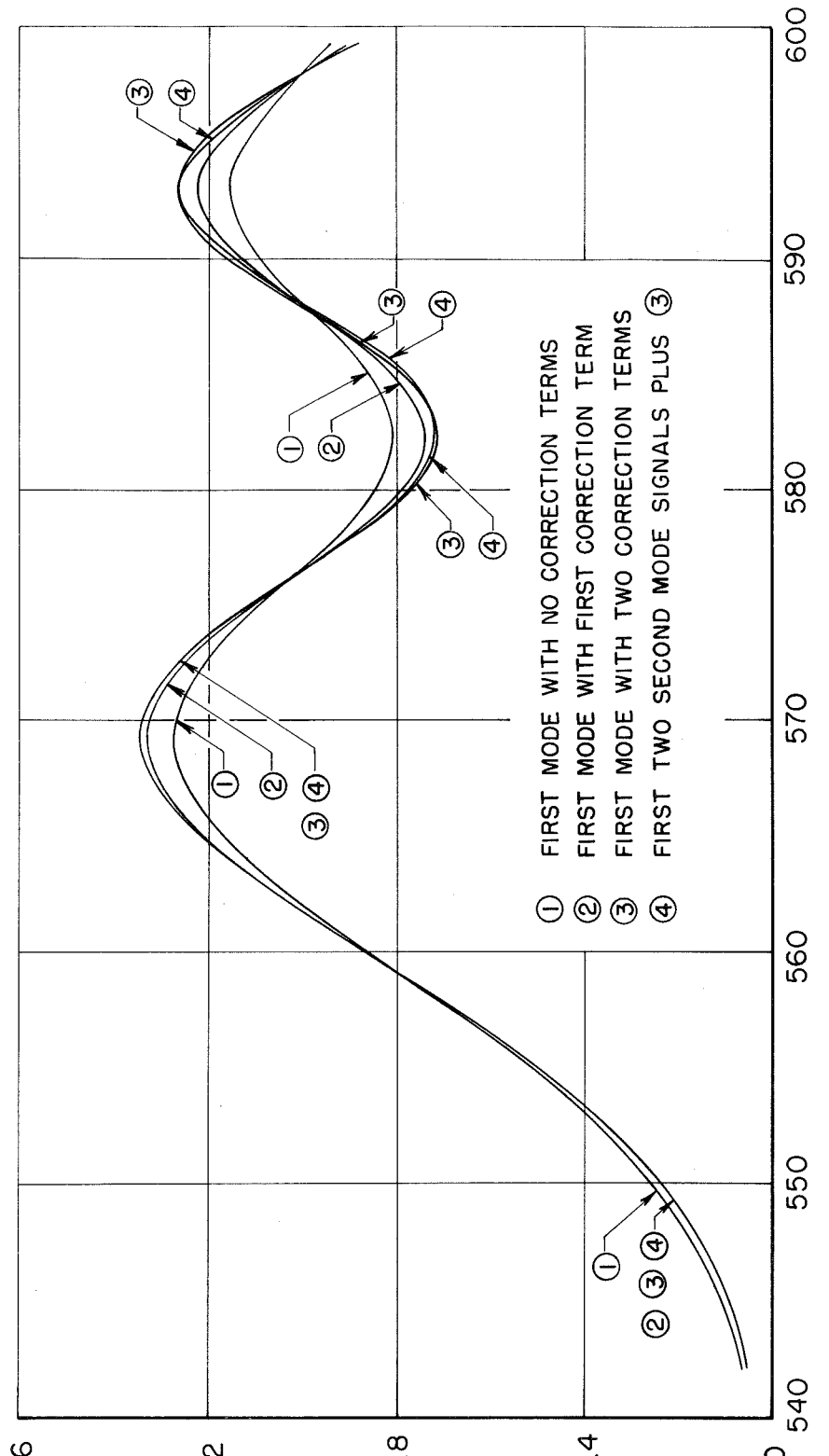

Figure 46. Predicted displacement $(Ev)/(\sigma P_o)$ at strip edge $y = a$ for the head of the pulse at station $x = 112.5$ in. Shear wave velocity $c_s = 0.1248$ in./μsec, Poisson's ratio $\sigma = 0.335$, and strip half-width $a = 0.75$ in.

condenser microphone records show some evidence of thickness mode activity at the head of the pulse, the records for $x = 37.5$, 75, and 112.5 inches are qualitatively very similar to the theoretical predictions.

Measured values for the dominant period $\bar{\tau}$ of the observed oscillations as a function of time are compared with predictions of the ordinary saddlepoint analysis in figures 47 and 48 for the four stations. The experimental points appearing on these figures were determined from measurements made on the magnified records of figures 39, 40, 41, and 42. The half-period was measured from a peak (dip) to a dip (peak) and the full period was then assumed to occur at the mean of the time determining the half-period.

In agreement with the predictions discussed above, the condenser microphone measurements are clearly associated with the first mode. There seems to be reasonably good general agreement between the measured and predicted values; however, a trend seems to be present indicating that the observed periods of the leading low-frequency oscillations become increasingly larger than the predicted periods as the distance of travel increases. This tends to indicate that the low-frequency components of the pulse are travelling at a lower velocity than predicted by the plane-stress theory.

To study this possibility, the arrival times of the first peak and the intervals between the first peak and the first dip were carefully measured. The results of these measurements, along with the estimated limits of error, are compared in Tables I and II with the predicted first mode values.

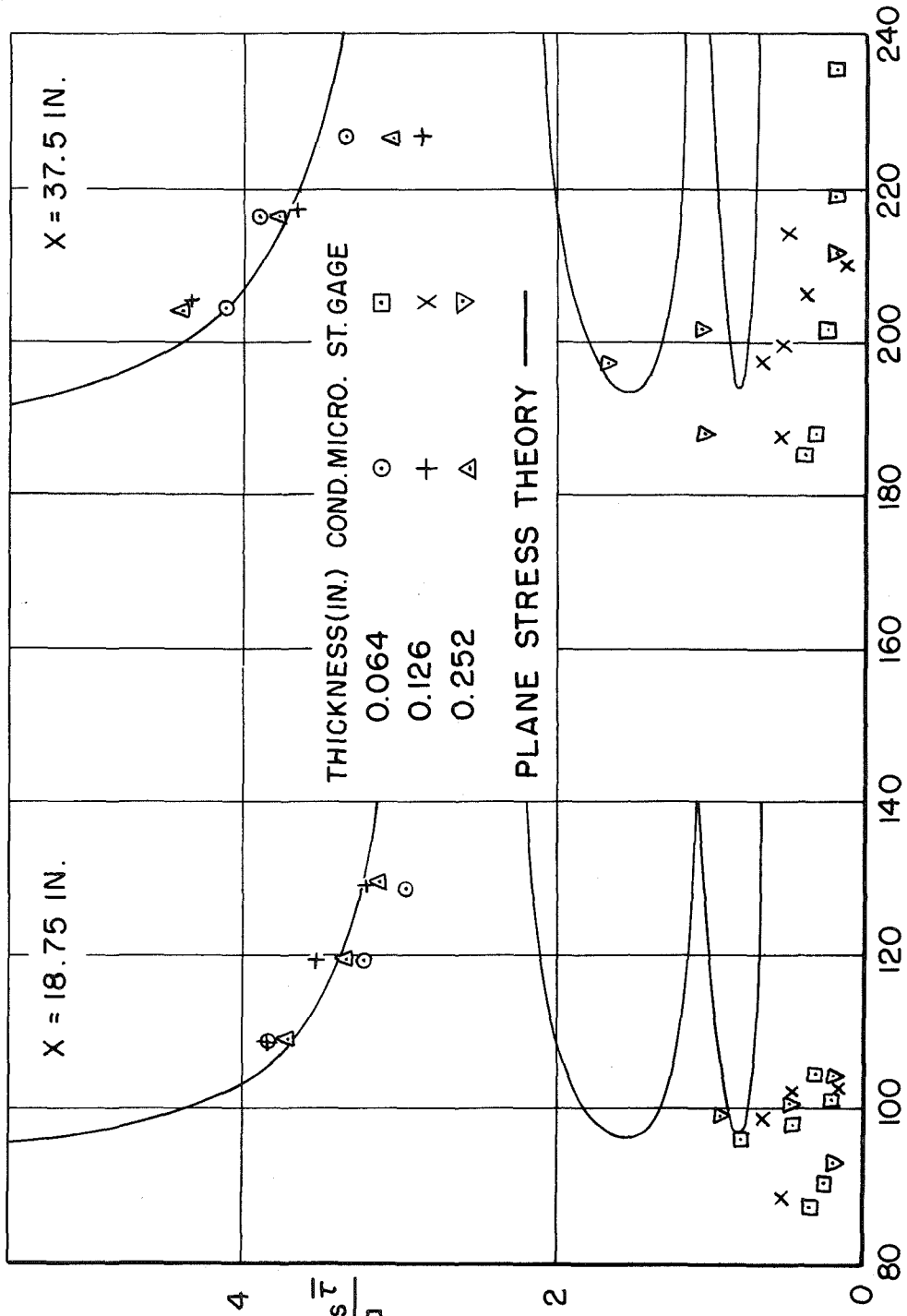

Figure 47. Comparison of measured values for the dominant period $\frac{c_s \bar{\tau}}{a}$ of observed oscillations at stations x = 18.75 in. and 37.5 in. with predictions of ordinary saddlepoint analysis.

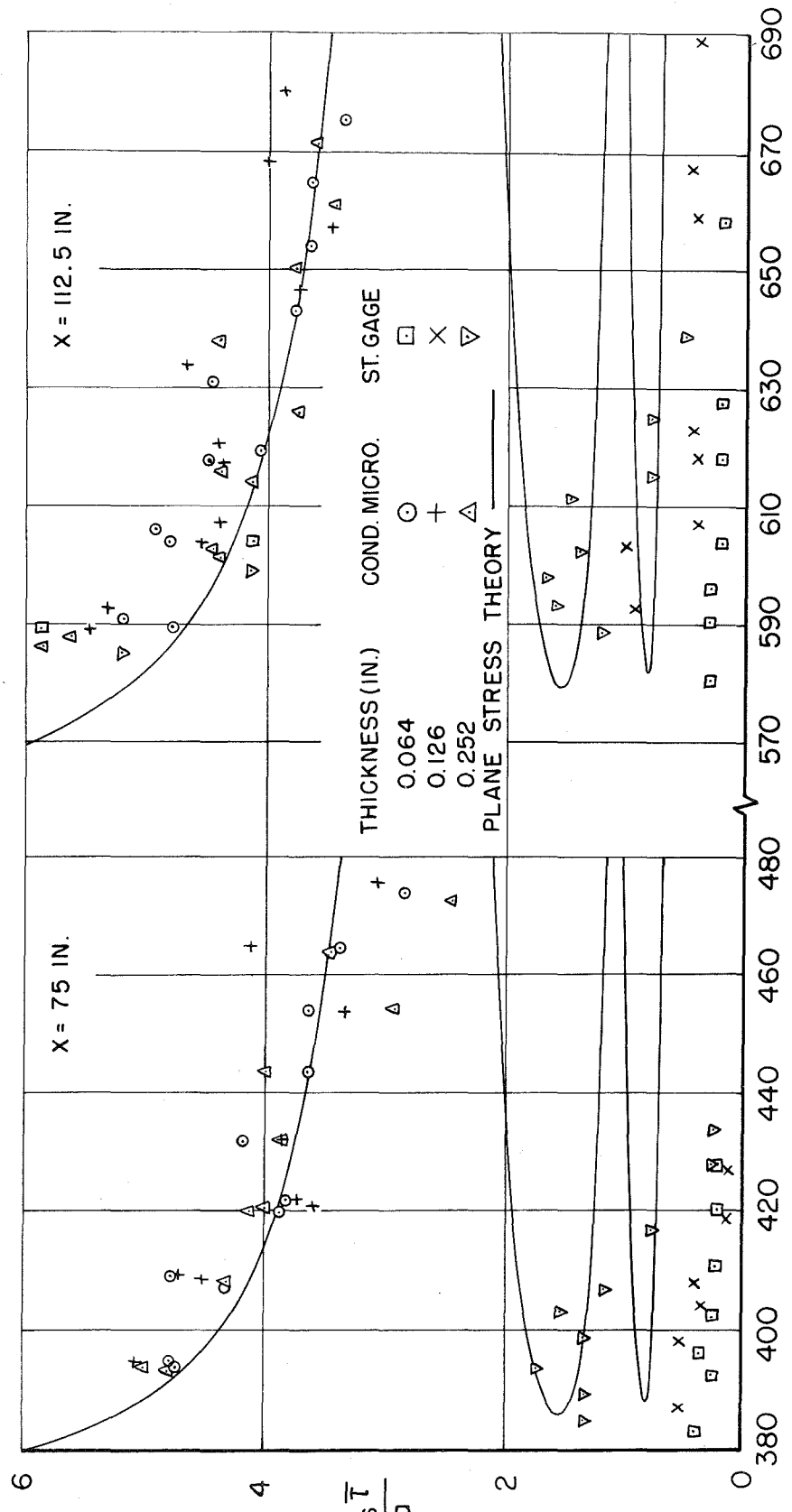

Figure 48. Comparison of measured values for the dominant period $\frac{c_s \bar{t}}{a}$ of observed oscillations at station x = 75 in. and 112.5 in. with predictions of ordinary saddlepoint analysis.

TABLE I

Predicted and Measured Arrival Times for the First Peak in the Condenser Microphone Records

Station x (inches)	Predicted First Mode Arrival Time (microseconds)		Measured Arrival Times (microseconds)		
			Bar Thickness (inches)		
	two terms	three terms	0.064	0.126	0.252
37.5	195.82	196.34	197.9 ±2.0	198.6 ±2.0	197.5 ±2.5
75.0	382.80	383.46	387.9 ±2.1	387.2 ±2.1	386.9 ±2.6
112.5	568.87	569.62	583.1 ±2.2	580.6 ±2.2	579.3 ±2.7

TABLE II

Predicted and Measured Time Intervals between the First Peak and the First Dip in the Condenser Microphone Records

Station x (inches)	Predicted First Mode Time Interval (microseconds)		Measured Arrival Times (microseconds)		
			Bar Thickness (inches)		
	two terms	three terms	0.064	0.126	0.252
75.0	11.763	11.110	14.2 ±1.0	15.2 ±1.0	15.0 ±1.0
112.5	13.466	12.718	15.4 ±1.0	16.4 ±1.0	16.9 ±1.0

From Tables I and II, it is apparent that the observed arrival times of the first peak and the time intervals between the first peak and the first dip are definitely larger than those predicted by the plane-stress theory and that the difference increases with increasing distance of travel. The implication, then, is that the low-frequency long-wavelength components of the pulse are travelling at a lower velocity than predicted

by the theory.

This is in agreement with the theoretical results of Gazis and Mindlin (64). Gazis and Mindlin studied the higher order approximate Kane-Mindlin equations of motion (66) which take into account the first symmetric extensional mode across the thickness. They showed that this thickness mode causes the low-frequency long-wavelength velocities of the first mode to be decreased from their corresponding plane-stress values. In terms of the notation of Part III, they found the first mode relation between α and β, for small β, to be

$$\alpha = \frac{\beta}{[2(1+\sigma)]^{1/2}} + \left[\frac{\sigma^2}{6[2(1+\sigma)]^{3/2}} + \frac{2\sigma^2(1-2\sigma)}{\pi^2[2(1+\sigma)]^{5/2}}\left(\frac{b}{a}\right)^2\right]\beta^3 + \ldots, \quad (141)$$

where b is the half-thickness of the bar. The corresponding plane-stress relation is given by equation 68 as

$$\alpha = \frac{\beta}{[2(1+\sigma)]^{1/2}} + \frac{\sigma^2\beta^3}{6[2(1+\sigma)]^{3/2}} + \ldots \quad . \quad (142)$$

According to the ordinary saddlepoint analysis, then, oscillations of frequency $\bar{\beta}$ should arrive at a particular station x at a time t given by

$$\frac{t}{x} = \frac{1}{[2(1+\sigma)]^{1/2}c_s} + \frac{1}{c_s}\left[\frac{\sigma^2}{2[2(1+\sigma)]^{3/2}} + H\right]\bar{\beta}^2 + \ldots, \quad (143)$$

where

$H = 0$ for the plane-stress theory,

and

$$H = \frac{6\sigma^2(1-2\sigma)}{\pi^2[2(1+\sigma)]^{5/2}}\left(\frac{b}{a}\right)^2 \quad \text{for the Kane-Mindlin theory.}$$

Clearly, the effect of including the thickness mode is to cause low-frequency oscillations of frequency $\tilde{\beta}$ to arrive at a given station at a time later than that predicted by the plane-stress theory. The observed and predicted values given in Tables I and II are in qualitative agreement with this conclusion. Also, equation 143 indicates that the effect will be accentuated for the larger ratios of thickness-to-width. The observed values given in Table II appear to confirm this observation.

The predicted and measured amplitude ratios of the first dip to the first peak in the condenser microphone records are compared in Table III.*

TABLE III

Predicted and Measured Amplitude Ratios of the First Dip to the First Peak in the Condenser Microphone Records

Station x (inches)[a]	Predicted First Mode Amplitude Ratio		Measured Amplitude Ratios		
			Bar Thickness (inches)		
	two terms	three terms	0.064	0.126	0.252
37.5	0.4843	0.3790	0.608	0.61	0.584
75S	{0.5369}	{0.4919}	0.662	0.616	0.609
75L			0.657	0.621	0.608
112.5S	{0.5590}	{0.5322}	0.612	0.589	0.645
112.5L			0.629	0.622	0.626

[a] S and L refer to short and long time records, respectively.

* Correction factors for the finite gage length of the condenser microphone pickup are negligible since the dominant wavelengths at the first peak and first dip, as estimated from figure 44, are at least 25 times the pickup diameter. Expressions for finite gage length correction factors as a function of wavelength are given in Appendix C for a circular detector and a detector of uniform width.

Table III shows that there is essentially no quantitative agreement between the predicted and observed amplitude ratios. The poor reproducibility of the records, which was discussed above, is reflected in the lack of any systematic order to the observed values. Since at least three records were obtained at each station for each bar, it should be pointed out that the spread in the amplitude ratios did not include the predicted values given in Table III.

Summarizing, the plane-stress theory provides a good qualitative description of the head of the pulse for the condenser microphone records. However, in view of the early arrivals of the higher modes and the consequent violation of the assumptions on which the theory is based, it is not surprising that the theory does not quantitatively describe the records.

Comparison of strain gage records with theory: The predicted barium titanate strain gage response, which is proportional to the sum of the principal strains $(e_{xx} + e_{yy})$ at the centerline $y = 0$ of the strip, is shown in figures 49 and 50 for the head of the pulse at stations $x = 37.5$ and 112.5 inches, respectively. The first mode contribution is obtained by evaluating equations 120 and 121 for $y = 0$ and summing the resulting expressions. The initial second mode contributions are obtained by summing equations 130 and 131 and evaluating the resulting expression separately for each of the two initial second mode arrivals. Similarly, second mode contributions following the initial arrivals are obtained by summing and evaluating equations 133 and 134.

Figures 49 and 50 show that the first mode correction terms reduce the magnitude of the oscillations; however, their overall effect is much less important than it was for the predicted condenser microphone response. The

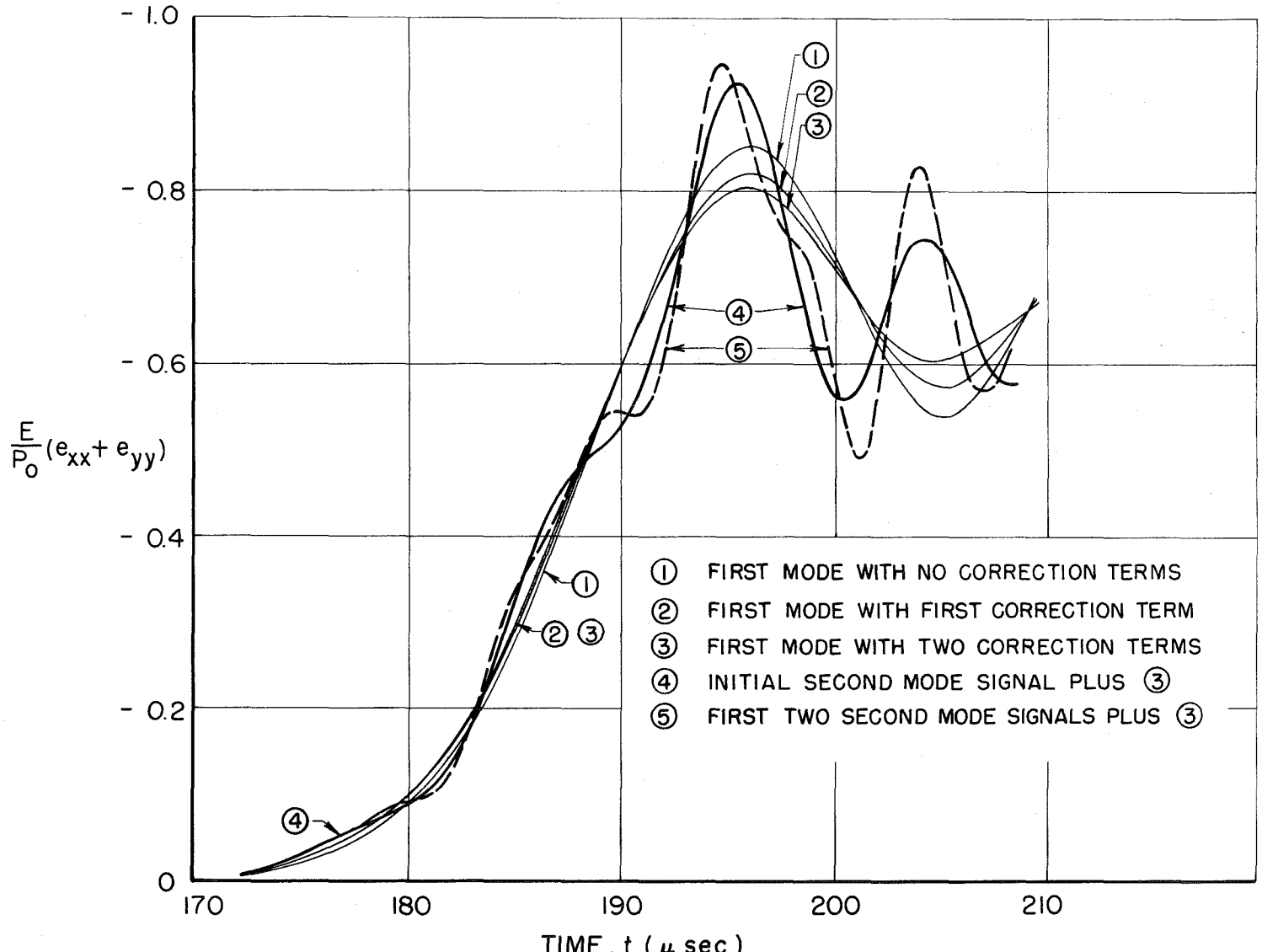

Figure 49. Predicted principal strain sum $E(e_{xx}+e_{yy})/P_o$ at $y = 0$ for the head of the pulse at station $x = 37.5$ in. Shear wave velocity $c_s = 0.1248$ in./μsec, Poisson's ratio = 0.335, and strip half-width $a = 0.75$ in.

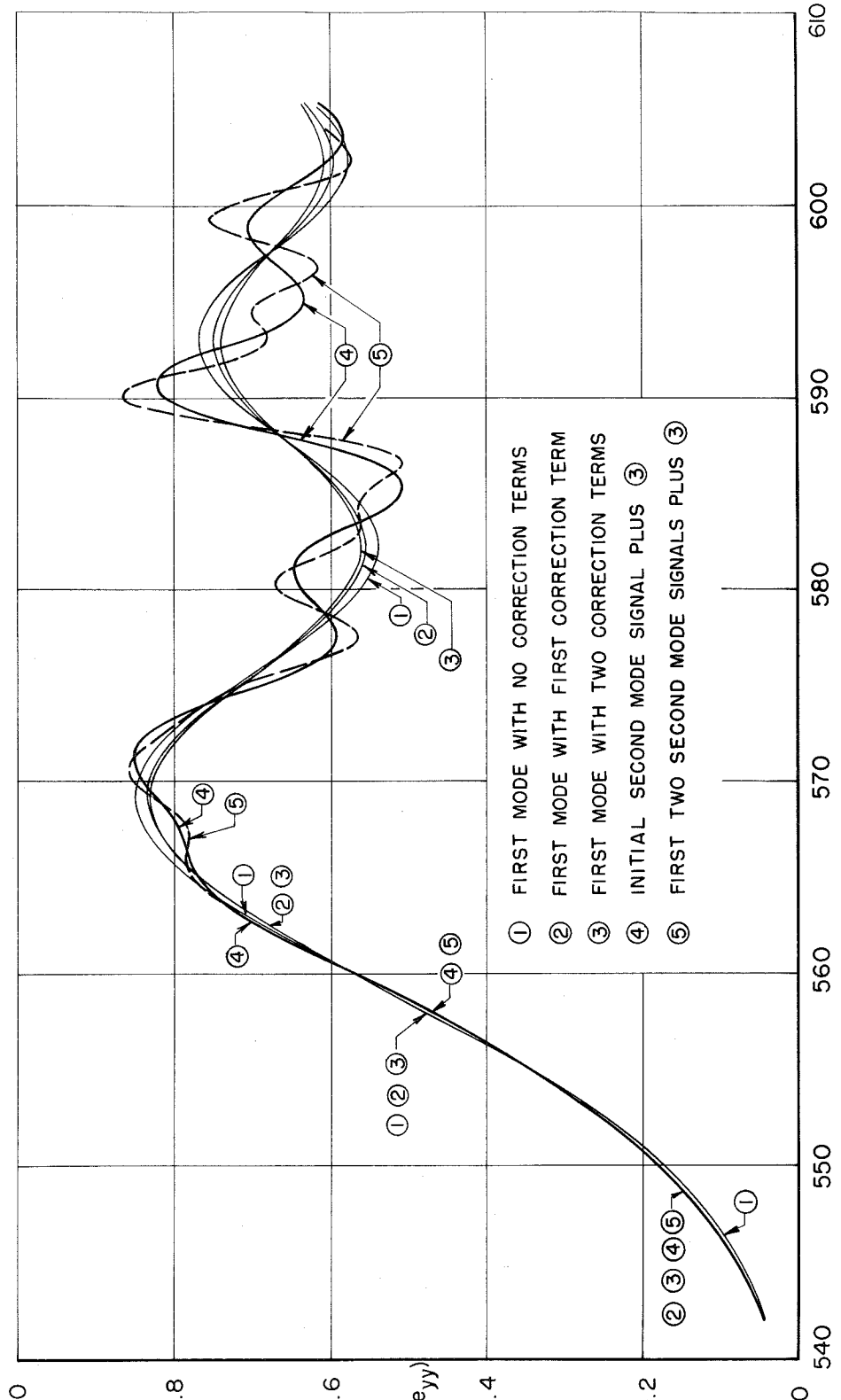

Figure 50. Predicted principal strain sum $E(e_{xx} + e_{yy})/P_o$ at $y = 0$ for the head of the pulse at station $x = 112.5$ in. Shear wave velocity $c_s = 0.1248$ in./μ sec, Poisson's ratio $\sigma = 0.335$, and strip half-width $a = 0.75$ in.

second mode oscillations are actually present at a given station x for times preceding the arrival times given in figures 43 and 44. These oscillations, which have an approximately exponentially decreasing amplitude, are predicted by the extended saddlepoint analysis.

Comparing the predicted strain gage records of figures 49 and 50 with the corresponding experimental records in figures 40 and 42, it is evident, at least for the 0.064 and 0.126 inch thick bars, that the gross features of the observed behavior at the head of the pulse are qualitatively described by the theory if the [2,2] contributions of the second mode are not considered. For example, considering the 0.252 inch thick bar record in figure 40 for station $x = 37.5$ inches, it is seen that as time increases the amplitude gradually increases, undergoes a fairly abrupt increase in slope, continues to increase, levels off in a brief plateau, increases rapidly to a fairly sharp peak, falls off rapidly to a dip, and then rises sharply again. Without the [2,2] contribution, the predicted record shown in figure 49 by the heavy solid line qualitatively exhibits all of these features. Except for thickness mode effects, the gross behavior for the 0.126 and 0.064 inch thick bars is generally similar. In the same manner, a comparison of figures 42 and 50 for station $x = 112.5$ inches shows that the theory qualitatively exhibits the gross features of the observed records. It is interesting to note that the qualitative agreement is best at both stations for the 0.252 inch thick bar.

Retaining the [2,2] contribution gives oscillations in the predicted strain gage records which do not appear to have counterparts in the experimental records. Rejecting this contribution is not particularly disturbing since it strongly violates the assumptions on which the plane-stress theory is based.

Summarizing, if only the [1,1] and [2,1] contributions are retained, the plane-stress theory provides a fairly good qualitative description of the gross behavior of the head of the pulse for the barium titanate strain gage records. It does not, however, provide valid quantitative predictions.

Conclusions and Recommendations

The propagation of a longitudinal elastic strain pulse in a wide rectangular bar has been considered on the basis of the approximate plane-stress equations of motion. Asymptotic expressions have been developed which, for large distances of travel, describe the propagation in a semi-infinite strip with stress-free lateral edges, subject to the end conditions that a uniform normal stress with a step-function time dependence is applied to the end and that the end undergoes no lateral extension.

Theoretical predictions based on these expressions have been compared in detail with experimental observations. The fringe curvatures, which result from the warping of plane sections, observed in the pictures obtained using birefringent coatings and in the dynamic photoelastic pictures of other investigators are qualitatively explained on the basis of this theory.

To provide more critical tests of the theory, an extensive experimental investigation using conventional measuring techniques was undertaken in which wide rectangular aluminum bars were subjected to a pressure-step produced by a shock tube. A condenser microphone pickup was used to record changes in the width of the bars, and barium titanate strain gages were used to record the sum of the principal strains midway between the

edges of the bars. It has been shown that the gross features of the experimental records obtained with these detectors are qualitatively predicted on the basis of the plane-stress theory.

For reasonable distances of travel it has been shown that the plane-stress theory predicts that second mode disturbances, which are generally not negligible, arrive very shortly after the first mode disturbance. This type of activity is strongly exhibited in the strain gage records. Furthermore, the theory predicts that the short-wavelengths associated with these second mode disturbances violate the assumptions under which the plane-stress behavior should represent the actual bar behavior. Supporting this conclusion, the strain gage records exhibit oscillations at the head of the pulse which are definitely associated with the bar thickness.

Careful studies of the condenser microphone records reveal that low-frequency components of the first mode oscillations travel at lower velocities than predicted by the plane-stress theory. Also, the velocities appear to be lower for larger ratios of bar thickness-to-width. It has been pointed out that these observations are in agreement with the theoretical results of Gazis and Mindlin (64). Their results were derived from the higher order approximate Kane-Mindlin equations of motion (66) which take into account the first symmetric extensional mode across the thickness.

Quantitative comparisons of measured relative amplitudes from the experimental records do not agree with predicted plane-stress values. Even for the condenser microphone records, which are expected to be dominated by the first mode, the theory does not predict the observed values.

In general, then, the plane-stress theory appears to do a remarkably good job of predicting the qualitative behavior of the head of a strain pulse in a wide rectangular bar. However, it fails when quantitative tests are attempted. There are several possible reasons for this. First, thickness modes may cause the true lowest mode solution to be sufficiently shifted from the corresponding approximate plane-stress solution so that quantitative values differ substantially while general qualitative agreement is still good. This was the situation in the case of the arrival time differences. Secondly, for moderate distances of travel the very early arrivals of higher width modes, which have relatively high frequencies, may cause the different lateral end conditions between the theoretical and experimental problems to become important for the head of the pulse.

In future studies, it would be worthwhile to obtain solutions $\alpha(\beta)$ and $\alpha'(\beta)$ over an extended frequency range for the frequency equation resulting from the Kane-Mindlin equations of motion. By comparing these solutions with the experimental results presented here, it should be possible to determine whether the Kane-Mindlin theory can be expected to be significantly better than the plane-stress theory for describing the observed behavior. On a larger scale, it would be interesting to solve the problem considered here on the basis of the Kane-Mindlin equations of motion. However, it should be noted that these equations are appropriate for including thickness effects only for small values of Poisson's ratio inasmuch as, for $\sigma > 1/3$, there is at least one symmetric thickness-shear mode whose frequency is less than that of the lowest symmetric thickness-stretch mode (cf. (85)). Since for the present experiments $\sigma = 0.335$, this point must be carefully examined. If

symmetric thickness-shear modes are to be included, the approximate second order equations of motion developed by Mindlin and Medick (87) must be used. However, the complexity of these equations promises major mathematical difficulties in obtaining solutions for transient problems.

Finally, an interesting observation should be made. The mathematical similarity between the equations of motion for the symmetrical vibrations of an infinite elastic plane-stress strip and the corresponding vibrations of a cylindrical bar has already been noted. For the cylindrical bar these are the exact equations of motion; consequently, considering only the strains at the surface of a cylindrical bar, Folk, Fox, Shook, and Curtis (48) found that solutions similar to those presented in Part III quantitatively described their experimental results (113) for large distances of travel. In arriving at their solutions, they implicitly assumed that plane sections remain plane. Skalak (49) also made this implicit assumption. Miklowitz (55), on the other hand, arrived at similar results using the approximate Mindlin-Herrmann equations of motion in which it is explicitly assumed that plane sections remain plane. Thus, all of the important transient solutions for the step-loading of a circular bar are either implicitly or explicitly based on the assumption that there is no warping of plane sections during the passage of the strain pulse.

In contrast to the results discussed above for wide rectangular bars, theory and experimental results (cf. (48,113)) for cylindrical bars both indicate that for moderate distances of travel the higher mode contributions are either negligible or arrive late enough so that the first mode of the theory is adequate for quantitatively describing the

head of the pulse. For cylindrical bars subjected to a step-pressure loading, Miklowitz and Nisewanger (44) are the only investigators who have made experimental measurements which should exhibit effects due to the first mode warping of plane sections. Since they used a condenser microphone to measure changes in the bar diameter, the mathematical similarity noted above suggests that their experimental records for large distances of travel should exhibit warping contributions similar to those shown by the correction term curves in figures 45 and 46. Miklowitz (44) observed just such discrepancies between his experimental results and theories based on plane sections remaining plane.

Thus, by retaining the correction terms in a similar manner as for the related plane-stress problem, it should be possible to quantitatively describe effects resulting from the warping of plane sections in a cylindrical bar subjected to a step-loading. Such an analysis is currently underway.

APPENDIX A. TABLES OF SOLUTIONS FOR THE FIRST TWO MODES OF THE FREQUENCY EQUATION

Numerical values of the solutions $\alpha_{1,1}(\beta)$ and $\alpha_{2,1}(\beta)$ of frequency equation 63', given in Part III, and their first two derivatives are presented in the following tables for ranges of β in which the solutions are real, for $\kappa = 0.4$, 0.35, 0.30, and 0.25. The tables very briefly summarize the results of a numerical program for obtaining these solutions. The calculations were performed by an IBM 704 computer programmed to essentially apply Newton's iterative method. The solutions obtained converged to six or seven places. The derivatives were obtained by taking first and second differences of α and β.

The corresponding real $\alpha_{2,2}$, $\alpha_{2,3}$, and $\alpha_{2,4}$ solutions are given by

$$\alpha_{2,1}(\beta) = -\alpha_{2,2}(-\beta) = -\alpha_{2,3}(\beta) = \alpha_{2,4}(-\beta).$$

The qualitative behavior of the second mode solution spectrum is shown in figure 6 of Part III.

The frequency equation 63' is applicable to the plane stress problem of Part III and to the related plane strain problem. For a given σ the corresponding value of κ depends on which problem is being considered.

$$\kappa = \frac{1 - \sigma}{2} \qquad \text{for the plane stress problem,}$$

and

$$\kappa = \frac{1 - 2\sigma}{2(1 - \sigma)} \qquad \text{for the related plane strain problem.}$$

Thus, the values given in the following tables can be applied to either case.

$a_{1,1}(\beta)$ and its first two derivative for real, positive β

$a_{1,1}$	β	$\frac{da_{1,1}}{d\beta}$	$\frac{d^2a_{1,1}}{d\beta^2}$

$\kappa = 0.40$ ($\sigma = 0.20$, plane stress; $\sigma = 0.16667$, plane strain)

0.000000	0.000000	0.64550	0.00000
0.375000	0.580370	0.64751	0.00765
0.625000	0.965258	0.65229	0.01879
0.875000	1.345604	0.66435	0.05109
1.062500	1.623761	0.68770	0.13328
1.187500	1.801571	0.72356	0.29769
1.312500	1.966668	0.80473	0.78358
1.375000	2.041179	0.88126	1.33407
1.500000	2.166233	1.16570	3.63049
1.593750	2.237191	1.49872	5.73238
1.656250	2.275832	1.73155	6.10201
1.750000	2.325717	2.00536	4.41677
1.812500	2.355960	2.11233	2.57708
1.906250	2.399520	2.17077	0.21727
2.062500	2.472169	2.10774	-1.55743
2.187500	2.532937	2.00355	-1.77316
2.375000	2.630577	1.84167	-1.49801
2.625000	2.773711	1.66294	-1.02494
3.250000	3.188193	1.39484	-0.39894
4.000000	3.760260	1.24948	-0.15835
5.000000	4.592233	1.16786	-0.05853
6.000000	5.462923	1.13394	-0.02483

$\kappa = 0.35$ ($\sigma = 0.30$, plane stress; $\sigma = 0.23077$, plane strain)

0.000000	0.000000	0.62017	0.00000
0.375000	0.603322	0.62452	0.01591
0.625000	1.000856	0.63479	0.03905
0.875000	1.388250	0.66012	0.10476
1.062500	1.664146	0.70631	0.25959
1.187500	1.834429	0.76986	0.52635
1.312500	1.986627	0.88842	1.12475
1.375000	2.053770	0.97944	1.62655
1.500000	2.167915	1.23596	2.96851
1.562500	2.215527	1.39157	3.52569
1.625000	2.258019	1.54885	3.78715
1.750000	2.332151	1.80881	2.91064

$a_{1,1}$	β	$\frac{da_{1,1}}{d\beta}$	$\frac{d^2a_{1,1}}{d\beta^2}$
1.875000	2.398361	1.94362	1.10424
1.968750	2.446158	1.96818	-0.02210
2.062500	2.493943	1.94878	-0.72501
2.281250	2.609539	1.82710	-1.18333
2.437500	2.697514	1.72652	-1.08044
2.750000	2.888679	1.55417	-0.73277
3.250000	3.232672	1.37349	-0.36935
4.000000	3.812283	1.23499	-0.15078
5.000000	4.653397	1.15562	-0.05689
8.000000	7.338723	1.09910	-0.00578
30.000000	27.486427	1.09145	-0.00000

$\kappa = 0.30$ (σ = 0.40, plane stress; σ = 0.28571, plane strain)

0.000000	0.000000	0.59761	0.00000
0.375000	0.625021	0.60504	0.02624
0.625000	1.033249	0.62237	0.06408
0.875000	1.424065	0.66372	0.16752
1.062500	1.694384	0.73359	0.38830
1.187500	1.856311	0.81947	0.71362
1.312500	1.998144	0.95713	1.29397
1.375000	2.060561	1.04950	1.68539
1.500000	2.168756	1.27479	2.48075
1.593750	2.237424	1.45610	2.84807
1.718750	2.317243	1.66666	2.31813
1.875000	2.406401	1.81516	0.93139
2.000000	2.474500	1.84330	-0.05046
2.187500	2.577240	1.79376	-0.77270
2.343750	2.666187	1.71757	-0.89440
2.750000	2.918073	1.51955	-0.64023
3.250000	3.268195	1.35402	-0.34076
4.000000	3.854662	1.22255	-0.14359
5.000000	4.703536	1.14569	-0.05507
6.000000	5.590918	1.11259	-0.02438

$\kappa = 0.25$ (σ = 0.50, plane stress; σ = 0.33333, plane strain)

0.000000	0.000000	0.57735	0.00000
0.375000	0.645545	0.58850	0.03817
0.625000	1.062625	0.61410	0.09231
0.875000	1.453975	0.67267	0.23333

$a_{1,1}$	β	$\frac{da_{1,1}}{d\beta}$	$\frac{d^2a_{1,1}}{d\beta^2}$
1.062500	1.717182	0.76403	0.50414
1.187500	1.871451	0.86563	0.84929
1.312500	2.005480	1.01107	1.36164
1.375000	2.064755	1.10020	1.65356
1.468750	2.144739	1.24828	2.03857
1.593750	2.237471	1.44751	2.30260
1.718750	2.318888	1.61421	1.76424
1.875000	2.411762	1.73296	0.74632
2.000000	2.483153	1.75901	0.01644
2.187500	2.590488	1.72345	-0.58100
2.375000	2.701625	1.64793	-0.72617
2.750000	2.941239	1.48900	-0.56581
3.250000	3.297020	1.33658	-0.31596
4.000000	3.889656	1.21183	-0.13675
5.000000	4.745179	1.13748	-0.05345
6.000000	5.638770	1.10497	-0.02404

$a_{2,1}(\beta)$ and its first two derivatives in the regions of real β corresponding to real $a_{2,1}$

$a_{2,1}$	β	$\frac{da_{2,1}}{d\beta}$	$\frac{d^2a_{2,1}}{d\beta^2}$
$\kappa = 0.40$ ($\sigma = 0.20$, plane stress; $\sigma = 0.16667$, plane strain)			
-6.000000	-9.424758	0.69548	-0.12997
-5.625000	-8.867760	0.66009	-0.02707
-5.125000	-8.103581	0.65183	0.00020
-4.625000	-7.339696	0.66079	0.02929
-4.125000	-6.609731	0.73582	0.27549
-3.781250	-6.196614	0.97225	0.84141
-3.406250	-5.852563	1.16271	0.14688
-3.125000	-5.611160	1.15559	-0.14354
-2.937500	-5.447015	1.12787	-0.18180
-2.500000	-5.047240	1.06587	-0.11131
-2.062500	-4.630713	1.04261	-0.00035
-2.000000	-4.570774	1.04308	0.01579
-1.625000	-4.214274	1.06723	0.12509
-1.375000	-3.983899	1.10725	0.23034

$a_{2,1}$	β	$\frac{da_{2,1}}{d\beta}$	$\frac{d^2a_{2,1}}{d\beta^2}$
-1.000000	-3.659954	1.22548	0.56341
-0.750000	-3.466888	1.38508	1.22013
-0.500000	-3.303118	1.73439	3.8132
-0.312500	-3.209542	2.43334	15.176
-0.250000	-3.185970	2.92878	29.553
-0.187500	-3.166980	3.78140	70.112
-0.125000	-3.153020	5.53365	238.53
-0.062500	-3.144472	10.8957	2003.3
0	-3.141593	-	-
Positive imaginary loop			
0	-2.483647	-	-
0.031250	-2.483320	47.7973	-73701.2
0.062500	-2.482343	24.1163	-9115.14
0.125000	-2.478524	12.4944	-1134.25
0.187500	-2.472448	8.82447	-329.919
0.312500	-2.455137	6.30791	-59.8082
0.359375	-2.447477	5.96752	-31.2336
0.406250	-2.439491	5.79862	-11.9954
0.437500	-2.434080	5.76343	-1.12176
0.453125	-2.431369	5.76679	3.65207
0.468750	-2.428663	5.78365	8.69088
0.500000	-2.423289	5.85777	18.7457
0.625000	-2.403152	6.76134	82.1087
0.750000	-2.387114	9.45822	344.638
0.812500	-2.381345	12.7928	995.236
0.890625	-2.376775	26.574	10620.3
0.937500	-2.375652	102.32	714080
Complex loop having positive imaginary component			
0.960938	2.375597	190.17	-5941000
0.992188	2.376091	37.605	-38062.0
1.125000	2.386612	7.1952	-381.39
1.250000	2.413007	3.37675	-60.393
1.500000	2.552439	1.13977	-4.0745
1.750000	2.840780	0.74221	-0.39766
2.000000	3.197982	0.67533	-0.08075
2.250000	3.573997	0.65788	-0.02465
2.656250	4.195658	0.65155	-0.00017
3.000000	4.722292	0.65532	0.01596
3.312500	5.194869	0.67032	0.05596
3.500000	5.470379	0.69432	0.13055
3.625000	5.646824	0.72619	0.24422
3.750000	5.813199	0.78288	0.46103
4.000000	6.098273	1.00150	1.06783
4.093750	6.187492	1.09986	1.11098
4.375000	6.418702	1.31386	0.66255

$a_{2,1}$	β	$\frac{da_{2,1}}{d\beta}$	$\frac{d^2a_{2,1}}{d\beta^2}$
$\kappa = 0.35$ (σ = 0.30, plane stress; σ = 0.23077, plane strain)			
-5.925000	-9.609584	0.97974	-0.58828
-5.425000	-9.012137	0.73301	-0.22429
-5.112500	-8.563215	0.66996	-0.08050
-4.612500	-7.796289	0.64341	-0.00341
-4.175000	-7.120565	0.65765	0.05267
-3.788750	-6.554530	0.72100	0.20244
-3.382500	-6.044104	0.89322	0.43996
-3.257500	-5.908626	0.95073	0.39524
-2.976250	-5.626190	1.02803	0.13873
-2.750000	-5.408017	1.04047	-0.00749
-2.468750	-5.136523	1.02914	-0.05755
-2.375000	-5.045197	1.02400	-0.05420
-2.000000	-4.676327	1.01272	0.00063
-1.625000	-4.307860	1.02816	0.08816
-1.375000	-4.067864	1.05857	0.17043
-1.000000	-3.726270	1.15008	0.40436
-0.750000	-3.518399	1.26951	0.82031
-0.500000	-3.336243	1.51971	2.3608
-0.312500	-3.226726	2.01515	8.9765
-0.250000	-3.197946	2.37196	17.339
-0.187500	-3.174234	2.99608	40.948
-0.125000	-3.156437	4.30177	139.04
-0.062500	-3.145359	8.35968	1167.3
0.000000	-3.141593	-	-
Positive imaginary loop			
0	-2.655130	-	-
0.020000	-2.654917	46.8376	-108198
0.062500	-2.653061	15.2423	-3598.03
0.125000	-2.647075	8.04624	-444.666
0.202500	-2.635136	5.54472	-99.1690
0.282499	-2.619133	4.63050	-30.2994
0.3874998	-2.595367	4.32269	0.77028
0.5474997	-2.559896	4.91654	38.5355
0.6399996	-2.542681	6.00001	98.8785
0.7499995	-2.527469	9.33208	503.816
0.8024994	-2.522726	13.7237	1787.36
0.8549994	-2.519889	28.951	18643.6
0.8849994	-2.519207	93.727	681597

$a_{2,1}$	β	$\frac{da_{2,1}}{d\beta}$	$\frac{d^2a_{2,1}}{d\beta^2}$
Complex loop having positive imaginary component			
0.947500	2.520216	22.477	-11934
1.072500	2.533798	5.5527	-216.51
1.125000	2.545023	3.99875	-91.450
1.250000	2.588481	2.19177	-19.9448
1.500000	2.768065	1.01167	-2.12076
1.750000	3.067642	0.73634	-0.36733
2.000000	3.428239	0.666061	-0.09539
2.437500	4.102520	0.64164	-0.00048
2.750000	4.587433	0.65051	0.03973
3.000000	4.965581	0.67570	0.10215
3.312500	5.406261	0.75754	0.30763
3.625000	5.779924	0.938889	0.678568
3.812500	5.966189	1.07718	0.77791
4.125000	6.231821	1.26688	0.59511
$\kappa = 0.30$ (σ = 0.40, plane stress; σ = 0.28571, plane strain)			
-6.000000	-9.745869	1.21221	-0.37814
-5.593750	-9.389608	1.06512	-0.43102
-5.000000	-8.755568	0.82238	-0.29779
-4.500000	-8.085833	0.69237	-0.10672
-4.031250	-7.385150	0.65772	-0.00179
-3.500000	-6.593269	0.70020	0.12229
-3.031250	-5.970492	0.81784	0.23492
-2.750000	-5.641499	0.88853	0.17696
-2.343750	-5.198669	0.93669	0.05252
-2.093750	-4.933372	0.94709	0.03272
-1.625000	-4.443677	0.97133	0.08010
-1.375000	-4.189509	0.99830	0.13621
-1.000000	-3.825524	1.07117	0.28484
-0.750000	-3.600226	1.15626	0.50205
-0.500000	-3.395644	1.30893	1.14543
-0.312500	-3.263068	1.56988	3.55768
-0.250000	-3.225179	1.75178	6.5304
-0.187500	-3.192068	2.07599	14.909
-0.125000	-3.165492	2.78535	49.82
-0.062500	-3.147847	5.11816	416.96
0	-3.141593	-	-

$a_{2,1}$	β	$\frac{da_{2,1}}{d\beta}$	$\frac{d^2a_{2,1}}{d\beta^2}$
Positive imaginary loop			
0	-2.867869	-	-
0.0312500	-2.866752	14.0839	-6283.6
0.062500	-2.863480	7.29830	-775.62
0.1015625	-2.856704	4.82983	-178.40
0.1406250	-2.847515	3.83995	-65.183
0.2343750	-2.819374	3.05829	-9.5815
0.2968750	-2.798522	2.97030	0.05118
0.3906250	-2.767485	3.11954	9.4573
0.5781250	-2.7151301	4.39213	54.616
0.6562500	-2.699416	5.77378	144.49
0.7578125	-2.685932	11.1224	1230.0
0.7968750	-2.683115	18.5615	6124.5
0.8359375	-2.681753	64.9595	299020
Complex loop having positive imaginary component			
0.867188	2.681778	57.862	-220800
0.968750	2.689409	7.3217	-504.15
1.125000	2.727928	2.7245	-33.934
1.250000	2.787568	1.68534	-9.26067
1.500000	2.996661	0.93654	-1.36854
1.750000	3.306651	0.72740	-0.31199
2.000000	3.669298	0.66496	-0.08286
2.250000	4.050801	0.65098	0.00015
2.500000	4.432589	0.66265	0.06202
2.750000	4.801017	0.69919	0.14717
3.000000	5.142689	0.77160	0.28567
3.250000	5.446253	0.88471	0.46547
3.625000	5.826487	1.09728	0.61192
4.000000	6.141613	1.27525	0.47734
$\kappa = 0.25$ (σ = 0.50, plane stress; σ = 0.33333, plane strain)			
-5.937500	-9.722576	1.27703	-0.27888
-5.406250	-9.283622	1.13963	-0.33118
-5.000000	-8.906796	1.01803	-0.30692
-4.500000	-8.376585	0.87476	-0.23084
-4.000000	-7.762000	0.76219	-0.13504
-3.500000	-7.075548	0.70713	-0.02611
-3.375000	-6.898384	0.70489	0.00071
-3.000000	-6.371468	0.72487	0.07197
-2.812500	-6.116410	0.74640	0.09487
-2.593750	-5.828853	0.77547	0.10412
-2.437500	-5.630005	0.79593	0.10054
-2.281250	-5.436020	0.81475	0.09312

$a_{2,1}$	β	$\frac{da_{2,1}}{d\beta}$	$\frac{d^2a_{2,1}}{d\beta^2}$
-1.625000	-4.662849	0.88381	0.10277
-1.250000	-4.250002	0.93701	0.16344
-0.875000	-3.865365	1.02096	0.29028
-0.625000	-3.629619	1.10633	0.45140
-0.375000	-3.414762	1.23165	0.75536
-0.187500	-3.269973	1.36898	1.19572
-0.062500	-3.182415	1.49395	1.70893
0.000000	-3.141593	1.57080	-
0.0234375	-3.126820	1.60288	2.22800
0.1250000	-3.066357	1.76683	3.27220
0.2500000	-3.000408	2.04983	5.66508
0.3750000	-2.944763	2.49478	11.449
0.5625000	-2.883370	4.01255	57.486
0.6250000	-2.869573	5.21955	135.79
0.7109375	-2.856760	9.51573	913.96
0.7500000	-2.853477	15.9717	4570
0.7890625	-2.851895	55.7397	217283
Complex loop having positive imaginary component			
0.820313	2.851915	51.320	-175980
0.921875	2.860495	6.5565	-395.34
1.000000	2.876832	3.7326	-81.066
1.125000	2.922941	2.10683	-16.4234
1.250000	2.996243	1.42859	-5.33358
1.500000	3.225577	0.89707	-0.99170
1.750000	3.539370	0.73326	-0.25226
2.000000	3.894498	0.68695	-0.04439
2.093750	4.031391	0.68394	-0.00096
2.250000	4.259129	0.69068	0.05886
2.500000	4.613084	0.72753	0.15188
2.750000	4.942822	0.79499	0.26249
3.000000	5.240465	0.89099	0.38490
3.468750	5.711299	1.11093	0.51718
3.750000	5.951236	1.23132	0.46924
4.000000	6.147409	1.31378	0.36345

APPENDIX B. TABLES OF THE AIRY FUNCTION Ai(-z), ITS FIRST THREE DERIVATIVES, AND ITS INTEGRAL

z	Ai(-z)	$\frac{dAi(-z)}{dz}$	$\frac{d^2Ai(-z)}{dz^2}$	$\frac{d^3Ai(-z)}{dz^3}$	$\frac{1}{3}+\int_0^z Ai(-\xi)d\xi$
-2.0	0.03492	0.05309	0.06985	0.07126	0.02080
-1.9	0.04059	0.06044	0.07713	0.07424	0.02457
-1.8	0.04704	0.06852	0.08467	0.07631	0.02894
-1.7	0.05432	0.07737	0.09235	0.07721	0.03400
-1.6	0.06254	0.08700	0.10006	0.07666	0.03984
-1.5	0.07175	0.09738	0.10762	0.07432	0.04654
-1.4	0.08204	0.10851	0.11485	0.06610	0.05422
-1.3	0.09347	0.12033	0.12152	0.06296	0.06299
-1.2	0.10613	0.13279	0.12735	0.05322	0.07296
-1.1	0.12005	0.14577	0.13205	0.04029	0.08426
-1.0	0.13529	0.15915	0.13529	0.02386	0.09701
-0.9	0.15189	0.17276	0.13670	0.00360	0.11136
-0.8	0.16985	0.18641	0.13588	-0.02072	0.12744
-0.7	0.18916	0.19985	0.13241	-0.04927	0.14537
-0.6	0.20980	0.21279	0.12588	-0.08212	0.16531
-0.5	0.23169	0.22491	0.11585	-0.11924	0.18738
-0.4	0.25474	0.23583	0.10190	-0.16041	0.21169
-0.3	0.27881	0.24515	0.08364	-0.20526	0.23836
-0.2	0.30370	0.25241	0.06074	-0.25322	0.26748
-0.1	0.32920	0.25713	0.03292	-0.28349	0.29912
0.0	0.35503	0.25882	0.00000	-0.35503	0.33333
0.1	0.38085	0.25696	-0.03808	-0.40655	0.37013
0.2	0.40628	0.25103	-0.08126	-0.45649	0.40949
0.3	0.43090	0.24055	-0.12927	-0.50307	0.45136
0.4	0.45423	0.22503	-0.18169	-0.54424	0.49562
0.5	0.47573	0.20408	-0.23786	-0.57777	0.54214
0.6	0.49485	0.17736	-0.29691	-0.60127	0.59069
0.7	0.51100	0.14464	-0.35770	-0.61225	0.64101
0.8	0.52357	0.10581	-0.41886	-0.60822	0.69277
0.9	0.53196	0.06091	-0.47876	-0.58678	0.74559
1.0	0.53556	0.01016	-0.53556	-0.54572	0.79900
1.1	0.53381	-0.04603	-0.58719	-0.48318	0.85252
1.2	0.52619	-0.10703	-0.63143	-0.39776	0.90557
1.3	0.51227	-0.17199	-0.66595	-0.28868	0.95755
1.4	0.49170	-0.23982	-0.68838	-0.15595	1.00780
1.5	0.46426	-0.30919	-0.69638	-0.00048	1.05566
1.6	0.42986	-0.37854	-0.68778	0.17581	1.10042
1.7	0.38861	-0.44612	-0.66063	0.36980	1.14140
1.8	0.34076	-0.51000	-0.61337	0.57723	1.17792
1.9	0.28680	-0.56809	-0.54492	0.79257	1.20935

z	$Ai(-z)$	$\frac{dAi(-z)}{dz}$	$\frac{d^2Ai(-z)}{dz^2}$	$\frac{d^3Ai(-z)}{dz^3}$	$\frac{1}{3}+\int_0^z Ai(-\xi)d\xi$
2.0	0.22741	-0.61826	-0.45481	1.00910	1.23510
2.1	0.16348	-0.65834	-0.34332	1.21903	1.25468
2.2	0.09615	-0.68624	-0.21152	1.41359	1.26769
2.3	0.02671	-0.70003	-0.06142	1.58337	1.27384
2.4	-0.04333	-0.69802	0.10400	1.71858	1.27301
2.5	-0.11233	-0.67885	0.28081	1.80946	1.26521
2.6	-0.17850	-0.64164	0.46411	1.84676	1.25064
2.7	-0.24004	-0.58601	0.64810	1.82226	1.22966
2.8	-0.29510	-0.51221	0.82627	1.72929	1.20284
2.9	-0.34191	-0.42118	0.99152	1.56334	1.17092
3.0	-0.37881	-0.31458	1.13644	1.32257	1.13479
3.1	-0.40438	-0.19482	1.25358	1.00833	1.09553
3.2	-0.41744	-0.06503	1.33582	0.62554	1.05433
3.3	-0.41718	0.07096	1.37670	0.18300	1.01249
3.4	-0.40319	0.20875	1.37085	-0.30656	0.97136
3.5	-0.37553	0.34344	1.31437	-0.82652	0.93231
3.6	-0.33478	0.46986	1.20520	-1.35673	0.89669
3.7	-0.28201	0.58273	1.04345	-1.87408	0.86575
3.8	-0.21886	0.67688	0.83165	-2.35330	0.84063
3.9	-0.14742	0.74756	0.57494	-2.76806	0.82226
4.0	-0.07027	0.79063	0.28106	-3.09225	0.81134
4.1	0.00968	0.80287	0.03968	-3.30145	0.80830
4.2	0.08921	0.78222	-0.37469	-3.37451	0.81326
4.3	0.16500	0.72794	-0.70949	-3.29514	0.82602
4.4	0.23370	0.64085	-1.02829	-3.05344	0.84602
4.5	0.29215	0.52336	-1.31469	-2.64728	0.87241
4.6	0.33750	0.37953	-1.55248	-2.08335	0.90402
4.7	0.36737	0.21499	-1.72663	-1.37782	0.93940
4.8	0.38004	0.03677	-1.82418	-0.55651	0.97692
4.9	0.37454	-0.14696	-1.83523	0.34556	1.01480
5.0	0.35076	-0.32719	-1.75381	1.28520	1.05121
5.1	0.30953	-0.49459	-1.57858	2.21286	1.08437
5.2	0.25258	-0.63991	-1.31342	3.07493	1.11259
5.3	0.18257	-0.75458	-0.96761	3.81668	1.13445
5.4	0.10293	-0.83122	-0.55585	4.38567	1.14878
5.5	0.01778	-0.86420	-0.09780	4.73530	1.15485
5.6	-0.06833	-0.85003	0.38265	4.82851	1.15231
5.7	-0.15062	-0.78782	0.85853	4.64118	1.14131
5.8	-0.22435	-0.67943	1.30124	4.16506	1.12247
5.9	-0.28512	-0.52963	1.68222	3.40993	1.09687
6.0	-0.32915	-0.34594	1.97487	2.40476	1.06601
6.1	-0.35351	-0.13836	2.15642	1.19753	1.03170
6.2	-0.35642	0.08107	2.20981	-0.14620	0.99602
6.3	-0.33735	0.29899	2.12529	-1.54630	0.96115
6.4	-0.29714	0.50148	1.90168	-2.91233	0.92926
6.5	-0.23802	0.67495	1.54713	-4.14918	0.90235

z	Ai(-z)	$\frac{dAi(-z)}{dz}$	$\frac{d^2Ai(-z)}{dz^2}$	$\frac{d^3Ai(-z)}{dz^3}$	$\frac{1}{3}+\int_0^z Ai(-\xi)d\xi$
6.6	-0.16353	0.80712	1.07927	-5.16346	0.88217
6.7	-0.07831	0.88791	0.52469	-5.87067	0.87001
6.8	0.01210	0.91030	-0.08231	-6.20217	0.86668
6.9	0.10169	0.87103	-0.70165	-6.11180	0.87240
7.0	0.18428	0.77101	-1.28997	-5.58134	0.88678
7.1	0.25404	0.61553	-1.80366	-4.62429	0.90883
7.2	0.30585	0.41412	-2.20213	-3.28755	0.93699
7.3	0.33577	0.18010	-2.45112	-1.65047	0.96927
7.4	0.34132	-0.07028	-2.52580	0.17872	1.00333
7.5	0.32178	-0.31881	-2.41332	2.06930	1.03669
7.6	0.27825	-0.54672	-2.11470	3.87681	1.06688
7.7	0.21372	-0.73605	-1.64565	5.45388	1.09164
7.8	0.13285	-0.87116	-1.03624	6.66216	1.10908
7.9	0.04170	-0.94004	-0.32944	7.38464	1.11787
8.0	-0.05271	-0.93556	0.42164	7.53719	1.11731
8.1	-0.14291	-0.85622	1.15756	7.07828	1.10747
8.2	-0.22160	-0.70660	1.81712	6.01571	1.08912
8.3	-0.28223	-0.49728	2.34252	4.40963	1.06375
8.4	-0.31959	-0.24422	2.68457	2.37105	1.03345
8.5	-0.33029	0.03231	2.80747	0.05563	1.00072
8.6	-0.31311	0.30933	2.69277	-2.34713	0.96832
8.7	-0.26920	0.56298	2.34208	-4.62869	0.93899
8.8	-0.20205	0.77061	1.77808	-6.57934	0.91526
8.9	-0.11727	0.91289	1.04367	-8.00748	0.89917
9.0	-0.02213	0.97566	0.19920	-8.75884	0.89215
9.1	0.07496	0.95150	-0.68213	-8.73358	0.89481
9.2	0.16527	0.84067	-1.52047	-7.89944	0.90692
9.3	0.24047	0.65149	-2.23641	-6.29935	0.92736
9.4	0.29348	0.39986	-2.75869	-4.05218	0.95427
9.5	0.31910	0.10810	-3.03148	-1.34601	0.98514
9.6	0.31465	-0.19695	-3.02066	1.57607	1.01708
9.7	0.28024	-0.48629	-2.71830	4.43674	1.04707
9.8	0.21887	-0.73154	-2.14490	6.95027	1.07223
9.9	0.13624	-0.90781	-1.34873	8.85112	1.09013
10.0	0.04024	-0.99627	-0.40241	9.95602	1.09903

APPENDIX C. FINITE GAGE LENGTH CORRECTIONS

The response of a gage of finite length l to a sinusoidally varying strain, represented by $A \sin 2\pi(x/\lambda - t/\tau)$, travelling along the bar depends on the wavelength λ of the strain oscillations. This effect must be considered in comparing amplitudes of oscillations in the strain pulse.

Considering a gage of uniform width, the response of an element of length dx to the passing strain wave is

$$KA \sin 2\pi\left(\frac{x}{\lambda} - \frac{t}{\tau}\right) dx,$$

where K is the gage constant. Taking the gage to be centered at $x = 0$, the response of the entire gage is given by

$$KA \int_{-l/2}^{l/2} \sin 2\pi\left(\frac{x}{\lambda} - \frac{t}{\tau}\right)dx = -KA \frac{\lambda}{\pi} \sin 2\pi \frac{t}{\tau} \sin \frac{\pi l}{\lambda} .$$

For wavelengths large compared to the gage length, the response is

$$-KA\, l \sin 2\pi \frac{t}{\tau} .$$

For a gage of uniform width, then, the response R to a wavelength λ relative to the response to an infinite wavelength is given by

$$R = \frac{\lambda}{\pi l} \sin \frac{\pi l}{\lambda} . \qquad (144)$$

Similarly, for a circular gage of diameter d, the relative response can be shown to be

$$R = \frac{2\lambda}{\pi d} J_1\left(\frac{\pi d}{\lambda}\right), \qquad (145)$$

where J_1 is the Bessel function of the first kind of order one.

REFERENCES

1. E. G. Coker and L. N. G. Filon, A Treatise On Photo-Elasticity, Cambridge University Press, London, 2nd Ed., 1957.

2. M. M. Frocht, Photoelasticity, Vol. 1, John Wiley and Sons, New York, 1941.

3. M. M. Frocht, Photoelasticity, Vol. 2, John Wiley and Sons, New York, 1948.

4. H. T. Jessop and F. C. Harris, Photoelasticity, Cleaver-Hume Press, Ltd., London, 1949.

5. M. M. Frocht, "Kinematography in Photoelasticity," Trans. Am. Soc. Mech. Engrs., Vol. 54, pp. 83-96(1932).

6. Z. Tuzi and M. Nisida, "Photoelastic Study of Stresses Due to Impact," Phil. Mag., Vol. 21, pp. 448-473(1936).

7. W. N. Findley, "The Fundamentals of Photoelastic Stress Analysis Applied to Dynamic Stresses," Proc. 9th Semi-Annual Eastern Photoelastic Conf., pp. 1-11(1939).

8. W. M. Murray, "A Photoelastic Study in Vibrations," J. Appl. Phys., Vol. 12, pp. 617-622(1941).

9. L. Foeppl, "Slow-Motion Pictures of Impact Tests by Means of Photoelasticity," J. Appl. Mech., Vol. 71, pp. 173-177(1949).

10. M. M. Frocht and P. D. Flynn, "Studies in Dynamic Photoelasticity," J. Appl. Mech., Vol. 23, pp. 116-122(1956).

11. M. M. Frocht, P. D. Flynn, and D. Landsberg, "Dynamic Photoelasticity by Means of Streak Photography," Proc. Soc. Exp. Stress Anal., Vol. 14, No. 2, pp. 81-90(1957).

12. A. A. Betser and M. M. Frocht, "A Photoelastic Study of Maximum Tensile Stresses in Simply Supported Short Beams Under Central Transverse Impact," J. Appl. Mech., Vol. 24, pp. 509-514(1957).

13. H. Schardin and W. Struth, "Hochfrequenz Kinematographische Untersuchung der Bruchvorgänge im Glas," Glastech. Ber., Vol. 16, p. 219 (1938).

14. H. Schardin, "Ergebnisse der Kinematographischen Untersuchung des Glasbruchvorgänges. III," Glastech. Ber., Vol. 23, p. 325(1950).

15. D. G. Christie, "An Investigation of Cracks and Stress Waves in Glass and Plastics by High-Speed Photography," J. Soc. Glass Technol., Vol. 36, pp. 74-89(1952).

16. D. G. Christie, "Reflection of Elastic Waves from a Free Boundary," Phil. Mag., Vol. 46, pp. 527-541(1955).

17. A. A. Wells and D. Post, "The Dynamic Stress Distribution Surrounding a Running Crack: A Photoelastic Study," Proc. Soc. Exp. Stress Anal., Vol. 16, No. 2, pp. 69-95(1958).

18. C. Cranz and H. Schardin, "Kinematographie auf ruhendem Film und mit extreme hoher Bildfrequenz," Z. Phys., Vol. 56, pp. 147-183 (1929).

19. D. A. Senior and A. A. Wells, "A Photoelastic Study of Stress Waves," Phil. Mag., Vol. 37, pp. 463-469(1946).

20. W. Goldsmith and G. W. Norris, Jr., "Stresses in Curved Beams Due to Transverse Impact, Proc. Third U. S. Nat. Cong. Appl. Mech., ASME, New York, 1958, pp. 153-160.

21. G. W. Sutton, "A Study of the Application of Photoelasticity to the Investigation of Stress Waves," Thesis, California Institute of Technology, Pasadena, Calif., 1955.

22. A. T. Ellis, "Techniques for Pressure Pulse Measurements and High-Speed Photography in Ultrasonic Cavitation," Cavitation in Hydrodynamics, Philosophical Library, Inc., New York, 1957.

23. J. C. Feder, R. A. Gibbons, J. T. Gilbert, and E. L. Offenbacher, "The Study of the Propagation of Stress Waves by Photoelasticity," Proc. Soc. Exp. Stress Anal., Vol. 14, No. 1, pp. 109-117(1956).

24. H. C. Perkins, "Movies of Stress Waves in Photoelastic Rubber," J. Appl. Mech., Vol. 75, pp. 140-141(1953).

25. A. J. Durelli and W. F. Riley, "Experiments for the Determination of Transient Stress and Strain Distributions in Two-Dimensional Problems," J. Appl. Mech., Vol. 24, pp. 69-76(1957).

26. J. W. Dally, W. F. Riley, and A. J. Durelli, "A Photoelastic Approach to Transient Stress Problems Employing Low-Modulus Materials," J. Appl. Mech., Vol. 26, pp. 613-620(1959).

27. A. J. Durelli, J. W. Dally, W. F. Riley, "Developments in the Application of the Grid Method to Dynamic Problems," J. Appl. Mech., Vol. 26, pp. 629-634(1959).

28. A. B. J. Clark, "Static and Dynamic Calibration of a Photoelastic Model Material, CR-39," Proc. Soc. Exp. Stress Anal., Vol. 14, No. 1, pp. 195-204(1956).

29. M. M. Frocht, "Studies in Dynamic Photoelasticity with Special Emphasis on the Stress-Optic Law," Stress Wave Propagation in Materials, Interscience Publishers, Inc., New York, 1960, pp. 91-118.

30. A. Mesnager, "Sur la Detérmination Optique des Tensions Intérieures des Solides à Trois Dimensions," C. R. Acad. Sci. Paris, Vol. 190, pp. 1249-1250(1930).

31. J. D'Agostino, D. C. Drucker, C. K. Liu and C. Mylonas, "An Analysis of Plastic Behavior of Metals with Bonded Birefringent Plastic," Proc. Soc. Exp. Stress Anal., Vol. 12, No. 2, pp. 115-122(1955).

32. J. D'Agostino, D. C. Drucker, C. K. Liu, and C. Mylonas, "Epoxy Adhesives and Casting Resins as Photoelastic Plastics," Proc. Soc. Exp. Stress Anal., Vol. 12, No. 2, pp. 123-128(1955).

33. F. Zandman, "Mésures photoélastiques des déformations élastiques et plastiques et des fragmentations cristallines dans les metaux," Rev. Met., Vol. 53, p. 638 (1956).

34. F. Zandman and M. R. Wood, "Photostress," Prod. Engng., Vol. 27, No. 9, pp. 167-178(1956).

35. J. Duffy, "Effects of the Thickness of Birefringent Coatings," Tech. Rep. 34, Div. Appl. Math., Brown University, 1958.

36. T. C. Lee, C. Mylonas, and J. Duffy, "Thickness Effects in Birefringent Coatings with Radial Symmetry," Tech. Rep. No. 1, Div. Appl. Math., Brown University, 1959.

37. K. Bills, Aerojet-General Corporation, Azusa, Calif., personal communication.

38. W. P. Mason, Physical Acoustics and the Properties of Solids, D. Van Nostrand Co., Inc., Princeton, 1958, p. 17.

39. J. Castle, "The Photographic Response of Several High-Speed Emulsions at Very Short Exposure Times," Photographic Engineering, Vol. 5, No. 3, pp. 189-194(1954).

40. D. Post, "Isochromatic Fringe Sharpening and Fringe Multiplication in Photoelasticity," Proc. Soc. Exp. Stress Anal., Vol. 12, No. 2, pp. 143-156(1955).

41. R. M. Davies, "A Critical Study of the Hopkinson Pressure Bar," Phil. Trans. Roy. Soc. (London), Ser. A, Vol. 240, pp. 375-457 (1948).

42. A. E. H. Love, A Treatise on the Mathematical Theory of Elasticity, Cambridge University Press, Cambridge, England, 4th Ed., 1927, pp. 287-292.

43. J. Oliver, "Elastic Wave Dispersion in a Cylindrical Rod by a Wide-Band Short-Duration Pulse Technique," J. Acoust. Soc. Am., Vol. 29, pp. 189-194(1957).

44. J. Miklowitz and C. R. Nisewanger, "The Propagation of Compressional Waves in a Dispersive Elastic Rod. Part II-Experimental Results and Comparison with Theory," J. Appl. Mech., Vol. 24, pp. 240-244 (1957).

45. G. Fox, "Dispersion of a Longitudinal Strain Pulse in an Elastic Cylindrical Bar," Thesis, Lehigh University, Bethlehem, Pa., 1956.

46. D. Bancroft, "The Velocity of Longitudinal Waves in Cylindrical Bars," Phys. Rev., Vol. 599, pp. 588-593(1941).

47. J. Adem, "On the Axially-Symmetric Steady Wave Propagation in Elastic Circular Rods," Quart. App. Math., Vol. 12, pp. 261-275 (1954).

48. R. Folk, G. Fox, C. A. Shook, and C. W. Curtis, "Elastic Strain Produced by Sudden Application of Pressure to One End of a Cylindrical Bar. I. Theory," J. Acoust. Soc. Am., Vol. 30, pp. 552-558(1958).

49. R. Skalak, "Longitudinal Impact of a Semi-Infinite Circular Elastic Bar," J. Appl. Mech., Vol. 24, pp. 59-64(1957).

50. A. E. H. Love, op cit., p. 428.

51. R. D. Mindlin and G. Herrmann, "A One-Dimensional Theory of Compressional Waves in an Elastic Rod," Proc. First U. S. Nat. Cong. App. Mech., ASME, New York, 1952, pp. 187-191.

52. R. E. D. Bishop, "Longitudinal Waves in Beams," Aero. Quart., Vol. 3, pp. 280-293(1952).

53. J. Miklowitz, "Travelling Compressional Waves in an Elastic Rod According to the More Exact One-Dimensional Theory," Proc. Second U. S. Nat. Cong. Appl. Mech., ASME, New York, 1955, pp. 179-186.

54. J. Miklowitz, "The Propagation of Compressional Waves in a Dispersive Elastic Rod. Part I-Results from the Theory," J. Appl. Mech., Vol. 79, pp. 231-239(1957).

55. J. Miklowitz, "On the Use of Approximate Theories of an Elastic Rod in Problems of Longitudinal Impact," Proc. Third U. S. Nat. Cong. Appl. Mech., ASME, New York, 1958, pp. 215-224.

56. R. D. Mindlin and H. D. McNiven, "Axially Symmetric Waves in Elastic Rods," J. Appl. Mech., Vol. 82, pp. 145-151(1960).

57. R. W. Morse, "Dispersion of Compressional Waves in Isotropic Rods of Rectangular Cross Section," J. Acoust. Soc. Am., Vol. 20, pp. 833-838(1948).

58. R. W. Morse, "The Velocity of Compressional Waves in Rods of Rectangular Cross Section," J. Acoust. Soc. Am., Vol. 22, pp. 219-223(1950).

59. G. Hok, "Thickness-Shear Vibrations of Thin Anisotropic Plates," J. Acoust. Soc. Am., Vol. 20, pp. 406-417(1948).

60. S. Ramo and J. R. Whinnery, Fields and Waves in Modern Radio, John Wiley and Sons, New York, 2nd Ed., 1953, pp. 296-360.

61. R. D. Mindlin and E. A. Fox, "Vibrations and Waves in Elastic Bars of Rectangular Cross Section," J. Appl. Mech., Vol. 27, pp. 152-158(1960).

62. L. D. Landau and E. M. Lifshitz, Theory of Elasticity, Pergamon Press, Inc., New York, 1959, pp. 52, 110.

63. R. E. D. Bishop, "On Dynamical Problems of Plane Stress and Plane Strain," Quart. J. Mech. and Appl. Math., Vol. 6, pp. 250-254 (1953).

64. D. C. Gazis and R. D. Mindlin, "Influence of Width on Velocities of Long Waves in Plates," J. Appl. Mech., Vol. 24, pp. 541-546 (1957).

65. A. N. Holden, "Longitudinal Modes of Elastic Waves in Isotropic Cylinders and Slabs," Bell Syst. Tech. J., Vol. 30, pp. 956-969 (1951).

66. T. R. Kane and R. D. Mindlin, "High-Frequency Extensional Vibrations of Plates," J. Appl. Mech., Vol. 23, pp. 277-283(1956).

67. R. T. Folk, "Time Dependent Boundary Value Problems in Elasticity," Thesis, Lehigh University, Bethlehem, Pa., 1958.

68. G. Horvay, "Biharmonic Eigenvalue Problem of the Semi-Infinite Strip," Quart. Appl. Math., Vol. 15, pp. 65-81(1957).

69. C. W. Curtis, "Propagation of an Elastic Strain Pulse in a Semi-Infinite Bar," Stress Wave Propagation in Materials, Interscience Publishers, Inc., New York, 1960, pp. 15-43.

70. C. J. Tranter, Integral Transforms in Mathematical Physics, Methuen and Co., London, 2nd Ed., 1956, Chapt. 1.

71. Lord Rayleigh, "On the Free Vibrations of an Infinite Plate of Homogeneous Isotropic Elastic Matter," Proc. London Math. Soc., Vol. 20, pp. 225-234(1889).

72. H. Lamb, "On Waves in an Elastic Plate," Proc. Royal Soc. (London), Ser. A., Vol. 93, pp. 114-128(1917).

73. J. Prescott, "Elastic Waves and Vibrations of Thin Rods," Phil. Mag., Vol. 33, pp. 703-754(1942).

74. J. L. B. Cooper, "The Propagation of Elastic Waves in a Rod," Phil. Mag., Vol. 38, pp. 1-22(1947).

75. F. A. Firestone, "Tricks with the Supersonic Reflectoscope," Non-Destructive Testing, Vol. 7, pp. 5-19(1948).

76. Y. Sato, "Study on Surface Waves. II: Velocity of Surface Waves Propagated upon Elastic Plates," Bull. Earthquake Research Inst. (Tokyo), Vol. 29, pp. 223-261(1951).

77. R. D. Fay and O. V. Fortier, "Transmission of Sound through Steel Plates Immersed in Water," J. Acoust. Soc. Amer., Vol. 23, pp. 339-346(1951).

78. R. R. Aggarwal and E. A. G. Shaw, "Axially Symmetric Vibrations of a Finite Isotropic Disk. I," J. Acoust. Soc. Amer., Vol. 24, pp. 463-467(1952).

79. R. R. Aggarwal and E. A. G. Shaw, "Axially Symmetric Vibrations of a Finite Isotropic Disk. II," J. Acoust. Soc. Amer., Vol. 24, pp. 663-666(1952).

80. R. R. Aggarwal and E. A. G. Shaw, "Axially Symmetric Vibrations of a Finite Isotropic Disk. III," J. Acoust. Soc. Amer., Vol. 25, pp. 533-535(1953).

81. R. R. Aggarwal and E. A. G. Shaw, "Axially Symmetric Vibrations of a Finite Isotropic Disk. IV," J. Acoust. Soc. Amer., Vol. 26, pp. 341-342(1954).

82. R. H. Lyon, "Response of an Elastic Plate to Localized Driving Forces," J. Acoust. Soc. Amer., Vol. 27, pp. 259-265(1955).

83. I. Tolstoy and E. Usdin, "Dispersive Properties of Stratified Elastic and Liquid Media: A Ray Theory," Geophysics, Vol. 18, pp. 844-870(1953).

84. I. Tolstoy and E. Usdin, "Wave Propagation in Elastic Plates: Low and High Mode Dispersion," J. Acoust. Soc. Amer., Vol. 29, pp. 37-42(1957).

85. R. D. Mindlin, An Introduction to the Mathematical Theory of Vibrations of Elastic Plates, Signal Corps Engineering Laboratories, Fort Monmouth, N. J., 1955.

86. R. D. Mindlin, "Mathematical Theory of Vibrations of Elastic Plates," Proc. 11th Ann. Symposium on Freq. Control, U. S. Army Signal Engineering Laboratories, Fort Monmouth, N. J., 1957, pp. 1-40.

87. R. D. Mindlin and M. A. Medick, "Extensional Vibrations of Elastic Plates," J. Appl. Mech., Vol. 26, pp. 561-569(1959).

88. D. C. Gazis and R. D. Mindlin, "Extensional Vibrations and Waves in a Circular Disk and a Semi-Infinite Plate," J. Appl. Mech., Vol. 27, pp. 541-547(1960).

89. R. D. Mindlin, "Waves and Vibrations in Isotropic Elastic Plates," Structural Mechanics, Proc. First Symp. Naval Struct. Mech., Pergamon Press, New York, 1960, pp. 199-232.

90. J. W. C. Sherwood, "Propagation in an Infinite Elastic Plate," J. Acoust. Soc. Amer., Vol. 30, pp. 979-984(1958).

91. H. Pursey, "The Launching and Propagation of Elastic Waves in Plates," Quart. J. Mech. and Appl. Math., Vol. 10, pp. 45-62(1957).

92. M. Redwood, "Velocity and Attenuation of a Narrow-Band, High-Frequency Compressional Pulse in a Solid Wave Guide," J. Acoust. Soc. Amer., Vol. 31, pp. 442-448(1959).

93. W. M. Ewing, W. S. Jardetzky, F. Press, Elastic Waves in Layered Media, McGraw-Hill Book Co., Inc., New York, 1957.

94. T. H. Havelock, The Propagation of Disturbances in Dispersive Media, Cambridge Univ. Press, London, 1914.

95. H. and B. S. Jeffreys, Methods of Mathematical Physics, Cambridge Univ. Press, Cambridge, 3rd Ed., 1956, Chapt. 17.

96. M. V. Cerrillo, "An Elementary Introduction to the Theory of the Saddlepoint Method of Integration," Tech. Report No. 55:2a, Res. Lab. Elect., M.I.T., Cambridge, Mass., 1950.

97. L. Brillouin, Wave Propagation and Group Velocity, Academic Press, New York, 1960.

98. J. C. P. Miller, "The Airy Integral," British Association for the Advancement of Science Mathematical Tables Part--Volume B, Cambridge Univ. Press, London, 1946.

99. C. M. Tyler, Jr. and W. T. Rouleau, "An Airy Integral Analysis of Beam-Columns with Distributed Axial Loading that Deflects with the Column," Proc. Second U. S. Nat. Cong. Appl. Mech., ASME, New York, 1955, pp. 297-305.

100. M. Newlands, "Lamb's Problem with Internal Dissipation. I," J. Acoust. Soc. Amer., Vol. 26, p. 440(1954).

101. C. W. Curtis, "Propagation of Elastic and Plastic Deformation in Solids," OOR Report, Lehigh Univ., Contract DA 36-034-ORD-1456 Sup. 4, Project TB 2-001(187), pp. 5-8(Sept. 1958).

102. A. J. Durelli and W. F. Riley, "Research Studies of Stress Waves in Earth and Model Earth Media," AFSWC Tech. Rep. 60-4, Armour Research Foundation, Contract AF 29(601)-1167, Project 1080, Task 10801, pp. 96-116(October, 1959).

103. I. I. Glass, W. Martin, and G. N. Patterson, A Theoretical and Experimental Study of the Shock Tube, Institute of Aerophysics, University of Toronto, UTIA Report No. 2, November 1953.

104. J. W. C. Sherwood, "Elastic Wave Propagation in a Semi-Infinite Solid Medium," Proc. Phys. Soc. Lond., Vol. 71, pp. 207-219(1958).

105. E. A. Ripperger, "A Piezoelectric Strain Gage," Proc. Soc. Exp. Stress Anal., Vol. 12, No. 1, pp. 117-124(1954).

106. M. Goland, P. D. Wickersham, and M. A. Dengler, "Propagation of Elastic Impact in Beams in Bending," J. Appl. Mech., Vol. 22, pp. 1-7(1955).

107. G. P. DeVault, "Three Dimensional Problems of an Elastic Cylinder with Mixed Time-Dependent End Conditions," Thesis, Lehigh University, Bethlehem, Pa., 1959.

108. J. N. Goodier, W. E. Jahsman, and E. A. Ripperger, "An Experimental Surface-Wave Method for Recording Force-Time Curves in Elastic Impacts," J. Appl. Mech., Vol. 26, pp. 3-7(1959).

109. J. W. Mark and W. Goldsmith, "Barium Titanate Strain Gages," Proc. Soc. Exp. Stress Anal., Vol. 13, No. 1, pp. 139-150(1955).

110. D. S. Hughes, W. L. Pondrom, and R. L. Mims, "Transmission of Elastic Pulses in Metal Rods," Phys. Rev., Vol. 75, pp. 1552-1556 (1949).

111. A. H. Meitzler, "Propagation of Elastic Pulses Near the Stressed End of a Cylindrical Bar," Inst. Rad. Eng. Convention Record, Part 9, pp. 55-60(1956).

112. F. C. Roesler, "Glancing Angle Reflection of Elastic Waves from a Free Boundary," Phil. Mag., Vol. 46, pp. 517-526(1955).

113. G. Fox and C. W. Curtis, "Elastic Strain Produced by Sudden Application of Pressure to One End of a Cylindrical Bar. II. Experimental Observations," J. Acoust. Soc. Amer., Vol. 30, pp. 559-563(1958).